Modelling and simulation of turbulent premixed combustion with stratification based on multiple mapping conditioning

von der
Fakultät Energie-, Verfahrens- und Biotechnik
der Universität Stuttgart
zur Erlangung der Würde einer
Doktorin der Ingenieurwissenschaften
(Dr.-Ing.) genehmigte Abhandlung

vorgelegt von
Carmen Straub
aus Herrenberg, Deutschland

Hauptberichter:	Prof. Dr. Andreas Kronenburg
Mitberichter:	Prof. Dr. Michael Pfitzner
Tag der mündlichen Prüfung:	13.05.2022

Institut für Technische Verbrennung
der Universität Stuttgart
2022

Erklärung

Hiermit versichere ich:

1. dass ich meine Arbeit selbstständig verfasst habe,
2. dass ich keine anderen als die angegebenen Quellen benutzt und alle wörtlich oder sinngemäß aus anderen Werken übernommenen Aussagen als solche gekennzeichnet habe,
3. dass die eingereichte Arbeit weder vollständig noch in wesentlichen Teilen Gegenstand eines anderen Prüfungsverfahrens gewesen ist,
4. dass ich die Arbeit noch nicht vollständig veröffentlicht habe und,
5. dass das elektronische Exemplar mit den anderen Exemplaren übereinstimmt.

Stuttgart, November 2022

Carmen Straub

Preface

Parts of this thesis have been presented at conferences and published in the archival literature. The introduction, theoretical developments and flame configurations given in Chapters 1, 3 and 4 have been modified with respect to the originally published texts and been significantly extended to ensure completeness, coherence and consistency of the present manuscript.

The relevant papers are:

1. C. Straub, A. Kronenburg, O. T. Stein, G. Kuenne, K. Vogiatzaki, Modelling of turbulent premixed stratified combustion with multiple mapping conditioning mixing model, *Proceedings of the 8th European Combustion Meeting*, 2017.

    - Data and results discussed in this paper are presented in Chapter 5.

    - Author's contribution: Programming (100%), data generation (100%), scientific originality (50%)

2. C. Straub, A. Kronenburg, O. T. Stein, G. Kuenne, J. Janicka, R. S. Barlow, D. Geyer, Multiple mapping conditioning coupled with an artificially thickened flame model for turbulent premixed combustion, *Combustion and Flame*, 196:325-336, 2018.

    - Data and results discussed therein are presented in Chapter 5.

- Author's contribution: Programming (100%), data generation - simulations (100%), data generation - experiments (0%), scientific originality (50%).

3. C. Straub, A. Kronenburg, O. T. Stein, R. S. Barlow, D. Geyer, Modeling stratified flames with and without shear using multiple mapping conditioning, *Proceedings of the Combustion Institute*, 37(2):2317-2324, 2019.

   - Data and results discussed in this paper are presented in Chapter 6.
   - Author's contribution: Programming (100%), data generation - simulations (100%), data generation - experiments (0%), scientific originality (50%).

4. C. Straub, A. Kronenburg, O. T. Stein, S. Galindo-Lopez, M. J. Cleary, Mixing time scale models for multiple mapping conditioning of partially premixed flames, *Proceedings of the* 11*th Mediterranean Combustion Symposium*, 2019.

   - Data and results discussed in this paper are presented in Chapter 7.
   - Author's contribution: Programming (100%), data generation (100%), scientific originality (50%)

5. C. Straub, A. Kronenburg, O. T. Stein, S. Galindo-Lopez, M. J. Cleary, Mixing time scale models for multiple mapping conditioning with two reference variables, *Flow, Turbulence and Combustion*, 106: 1143–1166, 2021.

   - Data and results discussed in this paper are presented in Chapter 7.
   - Author's contribution: Programming (100%), data generation (100%), scientific originality (50%).

Acknowledgements

This thesis originated from my work as a PhD student at the Institute for Combustion Technology of the University of Stuttgart. Without the help of the following people this thesis would have not been possible.

First and foremost I want to thank my supervisor Prof. Dr. Andreas Kronenburg for his input. Through his openness, patience and boundless knowledge he supported me a lot on my journey. I am also grateful to Dr. Oliver Stein who was always open for scientific discussions and helped me to reflect my work. I want to thank my colleagues at ITV including Ricarda Schubert for having the overview in all organization issues.

The financial support by Deutsche Forschungsgemeinschaft (DFG, German Research Foundation) - 393542303 and by the 2016 Universities of Australia - Germany Joint Research Co-operation Scheme is acknowledged. In this context I acknowledge Dr. Matthew J. Cleary, his group and Dr. Alexander Klimenko for having me in Australia. Traveling to the other end of the world and having topic specific discussions was a special experience for me for which I am very thankful.

Another thanks goes to D. Geyer (Hochschule Darmstadt) and R. S. Barlow (Sandia National Laboratories) for providing the experimental data which helps to validate the novel model and satisfies me because the model can be compared to data originating from measurements.

Abstract

The objective of the present study is to predict turbulent premixed combustion with stratification using a transported probability density function (PDF) approach. Depending on the turbulence level in premixed combustion the flame structure is altered and the PDF approach presents a powerful framework to predict flame structures independent of the combustion regime. Conventional mixing models for the closure of the PDF transport equation do not necessarily predict applications within the flamelet regime as they allow particles to mix across the flame front. Therefore, appropriate models are required which can preserve the flamelet structure. A sparse particle version of the *multiple mapping conditioning* (MMC) mixing model is applied in this work. In MMC the definition of reference variables is a crucial point which helps to locate the mixing operator close in composition space. An adequate choice of the reference variables prevents unphysical mixing of burnt and unburnt fluid. While in non-premixed combustion the reference variable can be chosen as the mixture fraction, in premixed combustion the choice is not that obvious. To specify the MMC reference space in premixed combustion the particle approach is coupled with an *artificial thickening flame* model (MMC-ATF) for large eddy simulations (LES). The reference variable is chosen as the LES reaction progress variable of the artificially thickened flame front. The LES-filtered reaction rate is closed by tabulated chemistry, while the source terms for the composition scalar field and temperature on the notional particles are treated locally for each particle. Therefore, MMC

allows for deviations from the tabulated chemistry and is expected to capture the correct flame structure. A series of turbulent stratified flames (TSF) with and without shear and stratification serves as validation cases and the simulation results are compared with experimental data.

Firstly, the MMC model with the thickened reaction progress variable as reference variable is validated. The MMC-ATF results are compared with experimental data of one configuration of the TSF series, which is characterized by stratification (TSF-A). The comparison shows good agreement and flamelet-like structures as well as deviations thereof can be predicted. A sensitivity study towards the localness parameter is investigated. The results are rather insensitive towards the MMC specific modelling parameter but the modelling of the mixing time scale needs to be adapted to achieve consistency between the flame propagation speed predicted by the artificially thickened flame model and the flame dynamics predicted by MMC.

Secondly, the advanced model's validation and generality are demonstrated and the MMC-ATF approach with the same set of parameters is applied to three flames of the TSF series. The simulation data is again validated by comparison with experimental data for the three flames. All flame locations are well predicted by the Eulerian ATF approach and an analysis of the MMC particle statistics demonstrates that MMC preserves the flamelet-like behaviour in regions where the experiments show low scatter around the flamelet structure. Predicted (local) deviations from the flamelet-solution are comparable to deviations observed in the measurements and variations in the flame structure due to differences in stratification and shear are reasonably well captured by the method.

Single conditioning on the reaction progress captures the flame structure, but stratification is not explicitly treated. In a final step, additional conditioning on mixture fraction is introduced to account for stratification. The model is again applied to TSF-A and validated by comparison with experimental data and the singly conditioned MMC results. The introduction of a second reference variable requires modification of the computation of the prescribed characteristic distance of the mixing particles, r_m. Several

strategies for the computation of r_m are suggested. The results are rather insensitive towards a variation of r_m. The second conditioning variable also requires the revision of the mixing time scale. Two different mixing time scale models are compared. A novel anisotropic model for stratified combustion leads to somewhat higher levels of fluctuations for the passive scalar when compared with the original model but differences remain small within the flame front. The results show that both models predict flame position and flame structure with good accuracy. Overall, double conditioning with appropriate time scale models leads to improved mixture fraction predictions that are clearly visible at downstream locations of the flame when compared with singly conditioned MMC. Due to the specific modelling of stratification the doubly conditioned MMC model is a more robust model.

Kurzfassung

Das Ziel der vorliegenden Arbeit ist die Vorhersage turbulent vorgemischter Verbrennung mit Schichtung mit einem Wahrscheinlichkeitsdichtefunktion (engl.: probability density function (PDF)) Ansatz. Je nach Turbulenzgrad kann die Flammenstruktur in der vorgemischten Verbrennung variieren. Um die Flammenstruktur unabhängig vom Verbrennungs-Regime abzubilden, stellt der PDF Ansatz eine erfolgreiche Methode dar. Übliche Mischungsmodelle zur Schließung der PDF Transportgleichung können nicht zwangsläufig das flamelet-Limit vorhersagen, da sich Partikel über die Flammenfront hinweg mischen können. Deshalb werden geeignete Modelle, die das flamelet-Regime annähern, gesucht. In dieser Arbeit wird eine Version des *multiple mapping conditioning* (MMC) Mischungsmodells mit einer dünnbesetzen Partikelmethode angewandt. Dabei erfährt die Bestimmung der Referenzvariablen einen hohen Stellenwert, da diese zur Lokalität des Mischens im Zustandsraum beiträgt. Eine geeignete Wahl der Referenzvariablen verhindert unphysikalisches Mischen von verbranntem und unverbranntem Fluid. In der nicht-vorgemischten Verbrennung ist dies der Mischungsbruch während in der vorgemischten Verbrennung die Wahl nicht so einfach ist. Um den MMC Referenzraum in der vorgemischten Verbrennung zu bestimmen wird die Partikelmethode mit dem *artificially thickened flame* (ATF) Ansatz für Grobstruktursimulationen (engl.: large eddy simulations (LES)), welche im Folgenden mit MMC-ATF abgekürzt wird, gekoppelt. Die Referenzvariable wird durch die LES Reaktionsfortschrittsvariable der künstlich aufgedickten

Flamme bestimmt. Die LES-gefilterte Reaktionsrate wird über tabellierte Chemie geschlossen, während die chemischen Quellterme der Partikel lokal für jedes einzelne Partikel bestimmt werden. Somit kann MMC Abweichungen von der tabellierten Chemie und vermutlich auch die korrekte Flammenstruktur vorhersagen. Eine turbulente, geschichtete Flammenserie (TSF) mit und ohne Scherung und Schichtung dient zur Validierung. Die Simulationsergebnisse werden mit experimentellen Daten verglichen.

Zunächst wird das Modell mit der aufgedickten Reaktionsfortschrittvariablen als Referenzvariable im MMC Mischungsmodell validiert. Dabei werden die MMC-ATF Ergebnisse mit den experimentellen Daten einer Konfiguration der Flammenserie, die Schichtung aufweist (TSF-A) verglichen. Der Vergleich weist gute Übereinstimmungen auf und sowohl die flamelet-Struktur als auch Abweichungen davon können durch die Simulationsergebnisse vorhergesagt werden. Eine Sensitivitätsanalyse der Ergebnisse bezüglich des MMC Modellparameters, der die Lokalität des Mischens bestimmt, wird untersucht. Die Ergebnisse sind eher robust gegenüber dem MMC charakteristischen Modellparameter. Die Modellierung der Mischungszeitskala wird angepasst, um konsistente Flammenausbreitungsgeschwindigkeiten der aufgedickten Flamme und des MMC Modells zu gewährleisten.

Im nächsten Schritt werden die weitergehende Validierung und Allgemeingültigkeit des Modells aufgezeigt und das MMC-ATF Modell wird auf drei verschiedene Flammen der TSF Serie angewandt. Eine Validierung der Ergebnisse wird durch den Vergleich mit experimentellen Daten aller drei Flammen gewährleistet. Die Flammenpositionen werden durch den Eulerschen ATF Ansatz gut vorhergesagt. In Regionen, in denen die experimentellen Werte wenig Streuung um die flamelet-Lösung aufweisen, prognostizieren die MMC Ergebnisse auch eine flamelet-Struktur. Die Abweichungen von der flamelet-Struktur der MMC Simulationsergebnisse sind in der gleichen Größenordnung wie die Abweichungen aus den experimentellen Daten. Abweichungen aufgrund von Schichtung oder Scherung werden durch das MMC Modell ebenfalls vorhergesagt.

Durch die Konditionierung auf den Reaktionsfortschritt wird die Flammenstruktur erfasst, gleichzeitig wird die Schichtung nicht explizit behandelt. Abschließend wird zusätzlich der Mischungsbruch als Referenzvariable eingeführt, was den Referenzraum um eine Dimension erweitert. Dabei wird das Modell auf die eingangs untersuchte Flamme TSF-A angewandt. Die Simulationsergebnisse werden wieder mit den experimentellen Daten und den Ergebnissen des einfachkonditionierten Ansatzes verglichen. Durch die zweite Referenzvariable wird die Berechnung der vorgeschriebenen charakterisierenden Distanz zweier sich mischender Partikel, r_m, beeinflusst. Deshalb wird die Berechnung von r_m auf verschiedene Arten untersucht. Dabei hat eine r_m Variation kaum Einfluss auf die Simulationsergebnisse. Durch die zweite Referenzvariable wird auch eine Überarbeitung der Mischungszeitskala benötigt und es werden zwei verschiedene Modelle verglichen. Ein neues, anisotropisches Mischungszeitmodel für geschichtete Verbrennung führt zu mehr Fluktuationen des Mischungsbruchs im Vergleich zu dem ursprünglich vorgeschlagenen Modell. Die Fluktuationsniveaus innerhalb der Flamme sind für beide Modelle vergleichbar. Die Ergebnisse zeigen, dass beide Modelle die Flammenposition und Flammenstruktur genau vorhersagen. Es lässt sich sagen, dass die Ergebnisse der Zweifachkonditionierung mit passenden Modellen für die Mischungszeitskalen zu verbesserten Mischungsbruchvorhersagen führen. Diese Verbesserungen im Vergleich zum einfachkonditionierten Ansatz sind besonders stromab zu beobachten. Durch die explizite Modellierung der Schichtung stellt das zweichfachkonditionierte MMC Modell ein robusteres Modell dar.

Contents

List of figures

List of tables

Chapter 1

Introduction

1.1 Background

Combustion appears in many applications of our everyday life, e.g. heating systems, car engines or gas turbines. This chemical process has increased the standard of life for human beings a lot. During the industrial revolution an extensive increase of combustion was observed. Combustion attributes to the global energy supply with more than 80% coming from gas, coal and oil as illustrated in Fig. 1.1. The increasing demand for renewable energies and the decreasing amount of fossil fuels can also be observed in the figure. This should not be misinterpreted, because the overall energy demand is continuously increasing. The current way of life cannot be maintained without combustion and combustion will be of major importance within the future. Unfortunately, combustion also contributes to a critical amount of greenhouse gasses in the atmosphere. There is no doubt that climate protection is important and this has become one of the central tasks for politics and society. In order to contribute to the fulfillment of e.g. the Paris Agreement

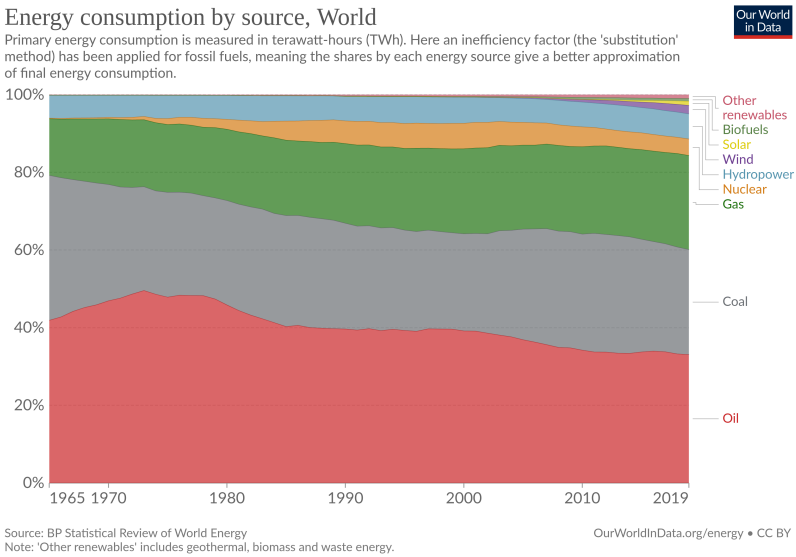

Figure 1.1: Energy consumption by source [59].

[9] the combustion process needs to be further explored and controlled. This implies decreasing the pollutant levels and the conscious and efficient application of fossil fuels. Computational models can contribute a lot to the pollutant prediction without wasting fossil fuels. Once a generic model is established it can be applied to a wide range of different fuels like hydrogen, natural gas, etc.. This is quite promising and becomes interesting as burning biomass is more and more important. To investigate the parameter set for efficient combustion the boundary conditions in simulations can be changed in a cheaper and more environmentally friendly way when compared with experimental setups. Numerous parametric studies can be performed to predict the most efficient setup. For some applications or phenomena where experiments

are difficult or impossible (e.g. at very large scales), simulations can be performed to predict the system's behaviour. In most applications combustion occurs in turbulent environments, where the length scales have a wide range extending from small scales to geometrical scales. Computational models of turbulent combustion account for this wide range of scales by filtering or averaging of the equations describing turbulent combustion. This results in filtered or averaged chemical source terms of reactive scalars. The non-linear dependency of these chemical source terms on the species mass fraction and temperature face a big challenge in computational models. Different approaches to meet this challenge are discussed in this work.

1.2 Motivation of this work

When talking about combustion one distinguishes between premixed and non-premixed combustion. While in non-premixed combustion fuel and oxidiser are introduced separately into the combustor in premixed combustion fuel and oxidiser are mixed before. Lean premixed combustion offers key advantages such as low propensity to soot formation and potentially very low NO_x emissions when compared to other combustion modes such as premixed combustion under stoichiometric conditions or non-premixed combustion. Despite these apparent advantages, lean premixed combustion is not always easy to realize in applications of practical interest as combustion instabilities may occur which leads to the necessity of increasing the fuel concentration locally (known as stratification). These purposely imposed equivalence ratio gradients can reduce emissions and extend the operational range which is also applied in direct injection stratified engines [16, 88]. Rather sophisticated computational models are required that capture all of the important thermo-physical interactions in premixed flames with strati-

fication. In this thesis, such an approach based on the multiple mapping conditioning (MMC) mixing model for turbulent stratified combustion is introduced. In previous studies, MMC was successfully applied to turbulent non-premixed combustion and is used in the current work to predict turbulent premixed combustion with stratification.

1.3 State of the art

In the simulation of combustion the transport equations of mass, momentum, energy and species are solved. Turbulent flows can be described by several techniques involving different degrees of simplification. These methods are direct numerical simulation (DNS), large eddy simulation (LES) or Reynolds averaged Navier Stokes (RANS) simulation. While the smallest scales are resolved in DNS, its high computational demand is challenging. In contrast, the RANS approach constitutes a model with a lower amount of computational cost (this is e.g. why it is mostly applied in industry for the complex geometries), but it is not appropriate to predict local flame structures. LES presents a model with intermediate computational time and amount of modelling. Hence, it provides a promising framework for the modelling of turbulent reacting flows and is discussed more detailed in this work. Some common approaches for turbulent premixed combustion are the modelling of the G-equation [54] or the flame surface density concept [4]. Further developments of these models account for stratification in turbulent premixed combustion [1, 50, 77]. These standard models are of kinematic nature where the flame front is assumed to be thin and effects of finite rate chemistry that may lead to deviations from a laminar flame structure are typically neglected. This is different for the artificially thickened flame (ATF) model [46] where - due to artificially increased diffusion - the flame front is resolved and finite rate chem-

istry effects can be approximated using reduced [46, 63] or tabulated [42] chemical mechanisms. Turbulence-chemistry interactions can be accounted for in even more detail when the joint (velocity and) composition probability density function (PDF) is known [56]. The evolution of the PDF can be computed by e.g. Eulerian stochastic fields [33] or Lagrangian Monte-Carlo [56] methods. A special case, that is also used in the present work, is the transported composition PDF method: the species composition and temperature are represented by Lagrangian particles while the velocities are obtained from RANS or LES. The major advantage of the PDF method is that the chemical source term is closed and no additional approximation needs to be introduced for the modelling of the effects of sub-grid turbulence on the chemical conversion process; thus, the PDF method presents a model that is not confined to a specific combustion regime and can - in principle - be applied to non-premixed, premixed and mixed combustion modes without any major modifications. Due to this ability the PDF method can successfully predict complex phenomena such as extinction and re-ignition [7, 47, 87]. However, the mixing model, which accounts for the effects of molecular and turbulent diffusion, requires closure, and the quality of PDF predictions strongly depends on the accuracy of the mixing model.

Conventional closures such as the interaction by exchange with the mean (IEM) [6, 17], modified Curl's (MC) [32] and the Euclidean minimum spanning tree (EMST) [73] models provided reasonable predictions for premixed flames that burn in the distributed flame regime [48, 60, 68]. The application of conventional models such as the IEM or different versions of the Curl mixing models to relatively thin premixed flames, i.e. flames that are within the flamelet regime, is, however, questionable as they allow particles to mix across the flame front. However, Tirunagari *et al.* [76] predicted reasonable flame prop-

agation speeds for LES combined with particle PDF methods and conventional mixing models without any explicit treatment of the flamelet structure. These encouraging results may be somewhat fortuitous since rather small LES cells were used. A more promising strategy should ensure mixing of particles which are close in composition space as this will prevent (unphysical) mixing of burnt and unburnt fluid across the flame. Haworth [28] coupled the PDF method with premixed laminar flamelet models while Zoller *et al.* [89] combined the PDF method with the Bray-Moss-Libby-model to locate the flame front and compute a flame surface density, which specifies the probability of a particle to ignite. Both approaches are suitable for the modelling of premixed flames that preserve a flamelet-like structure and that are within the wrinkled or corrugated flamelet regimes as classified by Peters [54]. The two models do not allow, however, for any deviation from these regimes. They enforce thin flame structures even though the flame may be thickened due to strong turbulence effects that act locally on the flame. A more universal mixing model that could be applied to all flame regimes would therefore be desirable. It should be able to predict flamelet-like structures if turbulence levels are low to moderate but it should also be able to predict any deviations thereof if turbulence is strong and the preheat or reaction zones are locally thickened.

Multiple mapping conditioning (MMC) [37] may represent such a model. The model combines useful features of the PDF method with the basic concepts of a mapping closure for the modelling of the turbulent mixing term. There are deterministic [82] and stochastic [83, 84, 69] implementations of the MMC framework in RANS. In the context of LES, Cleary and Klimenko [12] introduced sparse Lagrangian particle methods with a generalized MMC closure for the filtered density function (FDF) that is used to model the LES sub-filter contributions. The expression “sparse” refers to the number of stochastic particles that

can be as low as one stochastic particle per 30 LES cells. The MMC mixing model enforces localness of mixing in a (specified) reference space, and it is this conditioning on the reference field that allows for the sparse character of the particle loading. For non-premixed combustion, the LES-filtered mixture fraction is defined as such a reference variable and good predictions are obtained for a number of applications [29, 52, 53]. The question of finding a suitable reference variable for premixed flames remains open. Sundaram *et al.* [74] and Galindo-Lopez [24] discussed the choice of the reference variable for premixed combustion and suggested a variable similar to the shadow positions introduced by Pope [58] with a dense particle distribution. They successfully demonstrated the effect of their conditioning approach as the flamelet structure of the flame is conserved but its full application to realistic burners remains open.

This work does not adopt the strategies based on the shadow position [24, 74] but follows more closely the generalized MMC approach for non-premixed combustion [12]. The reference variable needs to be adapted for turbulent premixed combustion and the LES-filtered reaction progress variable is chosen as a suitable conditioning variable for sub-grid scale mixing. As the reaction progress variable is not fully resolved on the LES grid, the ATF approach [46] is employed and the filtered chemical source term is approximated using a two-dimensional flamelet generated manifold (FGM) [78]. At this stage it is unclear whether one of the two approaches is of clear advantage. Both methods require modelling for the prediction of the correct turbulent premixed flame speed as a particle based method for one-point statistics cannot adequately capture flame corrugation at sub-grid level [76]. The shadow position method may provide a better resolved reference field as resolution increases with stochastic particle number. It is, however, of computational disadvantage that many particles are needed. For the

LES with a thickened reaction progress, the resolution of the reference field depends on the LES grid resolution of the thickened flame, but computational efficiency is preserved as a sparse distribution of stochastic particles can continue to be used for the reactive species fields. The introduction of a thickened reference field does, however, require a new interpretation of the reference variables: the flame real width is considered to be the smallest physical scale and two modelling scales that are larger are introduced: the particle mixing distance and the thickened flame width. While conditioning on shadow positions or, in the case of non-premixed flames on mixture fraction, enforces localness in (real) composition space, the interpretation of conditioning on a thickened flame may be different. Here, the conditioning is primarily used for locating the flame position and imposing the correct turbulent flame speed.

To better control mixing in stratified flames a second reference variable given by the LES-filtered mixture fraction is introduced in the later chapters. The idea of increasing the dimension of the manifold is not new and has been applied in the flamelet [42], conditional moment closure (CMC) [39] and conditional source-term estimation (CSE) [18] approaches. Double conditioning on a progress variable and mixture fraction has also been used in the deterministic version of MMC for partially premixed flames in homogeneous, isotropic turbulence [40]. Here, double conditioning in the context of the sparse, stochastic version of MMC is presented for the first time.

Mixing with respect to sparse MMC requires both the selection of particle mixing pairs that are local in the reference space and modelling of the mixing time scale. The approaches developed for singly conditioned MMC of non-premixed flames can not be directly transferred to doubly conditioned MMC of premixed flames with stratification due to the presence of a relatively thin (unresolved) flame zone. Mixing

time scale models that differ from models validated for non-premixed combustion [81] are presented. For two-dimensional reference spaces in general (and therefore stratified combustion in particular) the exact choice of the mixing time scale model is not evident. As different models for the time scales exist, its exact modelling warrants some attention and the current work therefore assesses different suitable models and combinations thereof for the mixing frequency.

1.4 Objectives of the present work

It is noted here that any flamelet-based model, such as ATF-FGM, does not allow for the prediction of any departures of the flame from the pre-computed composition space as they could be caused by turbulence. In contrast, a stand-alone PDF method may not capture the correct turbulent flame speed but can predict the local thermo-chemical composition of the mixture. The two methods are thus quite complementary and this is why the LES using ATF-FGM is extended here by the MMC model. The model does not require any closure assumptions with respect to the expected flame regime. The premixed flame regime (as indicated by the position of the flame in the regime diagram proposed by Peters [54]) shall be a model output and its specification shall not be required prior to the simulations.

The overall goal of the current work is to demonstrate the general feasibility of a novel Lagrangian MMC mixing model (MMC-ATF) to predict turbulent premixed flames with stratification. The following objectives are formulated as a guideline to achieve the overall goal. The specific objectives of the current work are

1. to demonstrate that MMC-ATF with the filtered reaction progress variable as reference variable is flamelet consistent de-

spite the sparse character of the particle method and predicts possible deviations from the flamelet structure due to turbulence for a turbulent stratified flame located within the thin flame regime.

2. to further validate the MMC-ATF approach with the introduced parameter set by applying the model to different configurations of a flame series with and without shear and stratification.

3. to introduce a valuable model version of the MMC-ATF model for turbulent premixed combustion with stratification by extending the reference space by the filtered mixture fraction to directly model mixing of fluid elements of different equivalence ratio.

Results for MMC-ATF are compared with experimental data for the turbulent stratified flame (TSF) series, which had been selected as a target flame of the International Workshop on Measurement and Computation of Turbulent Flames [30]. The TSF series was experimentally investigated at TU Darmstadt [62] and at the Combustion Research Facility at Sandia National Laboratories, Livermore [67]. Numerous models were applied for model validation [22, 43, 50, 77]. As all the flames are meant to be located within the thin flame regime, deviations from the flamelet structure can be analyzed.

1.5 Thesis outline

This thesis is structured as follows: In Chapter 2 the fundamental equations of turbulent combustion and corresponding solution methods are presented. Chapter 3 describes details of the novel MMC mixing model introduced within this work. The flame configurations investigated in this thesis and the corresponding numerical setup are presented in Chapter 4. MMC based on a single reference variable for turbulent

premixed combustion is applied to one configuration of the turbulent stratified flame series (TSF-A) in Chapter 5. This configuration will be stated as the reference configuration in this work. Further investigations of this model include the application of MMC-ATF to different configurations of the turbulent stratified flame series with and without shear and stratification. The results are presented in Chapter 6. The model is extended by an additional reference variable and applied to the reference configuration in Chapter 7. The introduction of the additional reference variable prompts discussion on the mixing time scale and two different mixing time scale models are compared. Finally, Chapter 8 presents the overall conclusions and starting points, where future investigations can continue.

Chapter 2

Governing equations and modelling of turbulent combustion

In Sec. 2.1 the governing equations of reacting flows are stated. In Sec. 2.2 different approaches to obtain a solution for the evolution of inert mixtures in turbulent flows are discussed. Further details of one specific approach, namely, large eddy simulation are presented. Section 2.3 introduces the basic concept of chemical reaction along with a description of two different combustion modes. Section 2.4 presents advanced combustion models which account for the turbulence-chemistry interactions in mainly turbulent premixed combustion.

2.1 Fundamentals of reacting flows

The continuity equation, which describes the conservation of mass, reads

$$\frac{\partial \rho}{\partial t} + \frac{\partial (\rho u_j)}{\partial x_j} = 0, \tag{2.1}$$

where ρ represents the mass density and u_j the velocity component in jth direction. Note, that this notation makes use of the Einstein summation convention, i.e. repeated indices imply summation. In the momentum equation the rate of change of momentum is equal to the sum of the forces via

$$\frac{\partial (\rho u_i)}{\partial t} + \frac{\partial (\rho u_i u_j)}{\partial x_j} = \frac{\partial \tau_{ij}}{\partial x_j} - \frac{\partial p}{\partial x_i} + \rho g_i, \quad i = 1, 2, 3, \tag{2.2}$$

where p is the pressure, $\boldsymbol{g} = (g_1, g_2, g_3)$ is the gravity force vector and τ_{ij} is the viscous stress tensor. For a Newtonian fluid the stress tensor can be expressed as

$$\tau_{ij} = \mu \left[2S_{ij} - \frac{2}{3} \delta_{ij} \frac{u_k}{x_k} \right], \tag{2.3}$$

where μ is the dynamic viscosity and δ_{ij} is the Kronecker delta. The strain rate tensor, S_{ij}, is given by

$$S_{ij} = \frac{1}{2} \left(\frac{\partial u_i}{\partial x_j} + \frac{\partial u_j}{\partial x_i} \right). \tag{2.4}$$

The transport equation governing the mass fractions of reactive scalars, Y_α, reads

$$\frac{\partial (\rho Y_\alpha)}{\partial t} + \frac{\partial (\rho u_j Y_\alpha)}{\partial x_j} = -\frac{\partial J_{\alpha,j}}{\partial x_j} + \dot{\omega}_\alpha, \quad \alpha = 1, \ldots, n_s, \tag{2.5}$$

with $\dot{\omega}_\alpha$ representing the chemical source term of species α and n_s is the total number of species. The diffusion flux of species α in jth direction, $J_{\alpha,j}$, is modelled via Fick's law of diffusion as

$$J_{\alpha,j} = -\rho \mathcal{D}_\alpha \frac{\partial Y_\alpha}{\partial x_j}, \tag{2.6}$$

where $\mathcal{D}_\alpha$ is the diffusivity coefficient of species α. Neglecting differential diffusion effects, i.e. $\mathcal{D}_\alpha = \mathcal{D}$, Eq. (2.6) can be expressed as

$$J_{\alpha,j} = -\rho \mathcal{D} \frac{\partial Y_\alpha}{\partial x_j} = -\frac{\mu}{\mathrm{Sc}} \frac{\partial Y_\alpha}{\partial x_j}. \tag{2.7}$$

The Schmidt number, Sc, is defined as the ratio of momentum and mass diffusivity

$$\mathrm{Sc} = \frac{\mu}{\rho \mathcal{D}}. \tag{2.8}$$

The conservation of energy is represented by enthalpy and its transport equation reads

$$\frac{\partial (\rho h)}{\partial t} + \frac{\partial (\rho u_j h)}{\partial x_j} = -\frac{\partial J_{h,j}}{\partial x_j} + \dot{q}, \tag{2.9}$$

where $\dot{q}$ is the source or sink term of enthalpy due to e.g. radiation. The enthalpy flux, $J_{h,j}$, is given by heat conduction and species diffusion

$$J_{h,j} = -\lambda \frac{\partial T}{\partial x_j} - \rho \mathcal{D} \sum_{\alpha=1}^{n_s} h_\alpha \frac{\partial Y_\alpha}{\partial x_j}, \tag{2.10}$$

where λ is the thermal conductivity coefficient. This can be rewritten as

$$J_{h,j} = -\frac{\mu}{\mathrm{Pr}} \frac{\partial h}{\partial x_j} + \mu \left(\frac{1}{\mathrm{Pr}} - \frac{1}{\mathrm{Sc}} \right) \sum_{\alpha=1}^{n_s} h_\alpha \frac{\partial Y_\alpha}{\partial x_j}, \tag{2.11}$$

where $\mathrm{Pr} = \frac{\mu}{\lambda/C_p}$ is the Prandtl number and C_p is the specific heat capacity of the gas mixture at constant pressure. The Lewis number specifies the ratio of thermal to mass diffusivity

$$\mathrm{Le} = \frac{\mathrm{Sc}}{\mathrm{Pr}} = \frac{\lambda/C_p}{\rho\mathcal{D}}. \tag{2.12}$$

With the assumption of unity Lewis number, the second term in Eq. (2.11) vanishes. For this consideration Eqs. (2.5) and (2.9) have exactly the same form and can be written in a general form for $\boldsymbol{\phi} = \{Y_1, \ldots, Y_{n_s}, h\}$

$$\frac{\partial(\rho\boldsymbol{\phi}_\alpha)}{\partial t} + \frac{\partial(\rho u_j \boldsymbol{\phi}_\alpha)}{\partial x_j} = \frac{\partial}{\partial x_j}\left(\frac{\mu}{\mathrm{Sc}}\frac{\partial \boldsymbol{\phi}_\alpha}{\partial x_j}\right) + \dot{\omega}_\alpha, \tag{2.13}$$

with $\dot{\omega}_{n_s+1} = \dot{q}$. The system of equations (2.1), (2.2) and (2.13) holds fewer equations than unknowns. An additional equation is missing to close the system. The equation of state for ideal gases is solved and reads

$$p = \frac{\rho R_u T}{\overline{M}}, \tag{2.14}$$

where R_u is the universal gas constant and $\overline{M}$ is the mixture molecular weight.

In the remaining part of this chapter, solution methods for the introduced equations which govern turbulent reacting flows are presented.

2.2 Turbulence

In this section the solution of the governing equations for turbulent flow is investigated. In most combustion applications, e.g. engines, furnaces, etc. the fluid flow is turbulent. This section focuses on the discussion of appropriate solution methods for the turbulent flow field of chemically

inert fluid. An accurate prediction for the thermo-physical interactions between flow field and flame requires advanced computational models, which are further discussed in Sec. 2.3.

2.2.1 Phenomenon

Turbulent flows are characterized by the following properties [57]

- Turbulent flows are highly unsteady. Plotting the velocity versus time at most points in the flow would show high fluctuations.
- Turbulence is three-dimensional.
- Turbulence increases mixing.
- Dissipation: Kinetic energy is converted in sub-grid scale vortices into internal energy of the fluid.
- Turbulent motions occur over a wide range of length and time scales.

These properties make the description of turbulence challenging and the direct solution of the system of equations (2.1), (2.2) and (2.13) is difficult to achieve.

2.2.2 Transition from laminar to turbulent flow

Fluid flows can be laminar or turbulent. The Reynolds number, Re, can predict the transition from laminar to turbulent state and is given by

$$\mathrm{Re} = \frac{UL}{\nu}, \tag{2.15}$$

where U is a characteristic velocity, L is a characteristic length scale and $\nu = \mu/\rho$ is the kinematic viscosity. The Reynolds number represents

the ratio of inertial forces to viscous forces. Exemplary, the specific properties given in Eq. (2.15) for a pipe flow are demonstrated. The characteristic velocity is given by the mean velocity over the cross-section of the pipe, the characteristic length scale is defined via the pipe diameter and ν is the kinematic viscosity of the fluid. For values of Re above the critical value of approximately 2300 the pipe is dominated by turbulent flow [79].

2.2.3 Length and time scales in turbulent flows

Different scales within turbulent flows can be defined. The smallest scale found in turbulent flows is given by the Kolmogorov length scale [38]

$$\eta = \left(\frac{\nu^3}{\epsilon}\right)^{1/4}, \tag{2.16}$$

where ϵ is the kinetic energy dissipation. The corresponding time scale is given by

$$\tau_\eta = \left(\frac{\nu}{\epsilon}\right)^{1/2}. \tag{2.17}$$

In the same way the velocity scale is defined by

$$u_\eta = (\nu\epsilon)^{1/4}. \tag{2.18}$$

The comparison of the smallest and largest turbulent eddies is given by the ratio of the integral length scale, l_t, to the Kolmogorov length scale [55]

$$\frac{l_t}{\eta} = \mathrm{Re}_t^{3/4}, \tag{2.19}$$

with the integral Reynolds number

$$\mathrm{Re}_t = \frac{u' l_t}{\nu}. \tag{2.20}$$

2.2.4 Classification of numerical approaches

There are three simulation approaches to solve the transport equations of turbulent flows: (i) direct numerical simulation (DNS), (ii) Reynolds averaged Navier–Stokes (RANS) description and (iii) large eddy simulation (LES).

In DNS the governing equations are solved with an adequate spatial resolution and time step size to compute the smallest scales (Kolmogorov scales). These requirements on the spatial and temporal resolution end up in large computational cost. Therefore, DNS is quite popular for research purposes where small physical dimensions can be applied to benchmark problems. The DNS data can also serve for validation or development of different modelling approaches [8, 45]. In contrast, the RANS simulations correspond to a time or ensemble averaging of the instantaneous transport equations while all the fluctuations are modelled. The transport equations for the averaged quantities are obtained by averaging the transport equations and unclosed terms arise. As these terms represent the fluctuations from the time-averaged quantities, the modelling part is very large and amount of computational cost is reduced. In industry, RANS computations are frequently applied to model turbulent flows of complex geometries. LES depicts an intermediate approach concerning computational cost and amount of modelling. In LES the large scale motion of the flow is resolved and limited to the computational resolution. The smallest turbulent eddies are modelled via sub-grid dissipation rate models. LES has been established as a promising approach within the last decades and is the basis of the model introduced in this work.

2.2.5 Large eddy simulation

LES is a promising and widely applied approach. The model applied in this work is based on LES and further details of this approach are demonstrated. The basic idea of LES is to resolve the large scale eddies while the small scale motion is modelled. The distinction of these scales is accomplished by spatial filtering of the transport equations.

2.2.5.1 Filtered transport equations

The LES transport equations are obtained by filtering the instantaneous transport equations introduced in Sec. 2.1. The filtering operator, $\mathcal{G}$, depends on the filter size, Δ_E, and is applied as

$$\overline{\phi}(x,t) = \int_{-\infty}^{\infty} \phi(x',t)\mathcal{G}(x'-x;\Delta_E)dx'. \tag{2.21}$$

Different to RANS averaging the doubly applied filter operator is not the same as the singly applied filter operator

$$\overline{\overline{\phi}} \neq \overline{\phi}. \tag{2.22}$$

It is common practice to assume that the filter operation is commutable with the derivative operators [55]

$$\overline{\frac{\partial \phi}{\partial x_j}} = \frac{\partial \overline{\phi}}{\partial x_j}, \tag{2.23}$$

as the differences are mostly negligible. In applications of variable density, e.g. in combustion, the Favre filtered scalar is introduced

$$\widetilde{\phi} = \frac{\overline{\rho\phi}}{\overline{\rho}}. \tag{2.24}$$

Instantaneous properties can be decomposed into the Favre filtered term and the sub-grid scale (sgs) fluctuations

$$\boldsymbol{\phi} = \tilde{\boldsymbol{\phi}} + \boldsymbol{\phi}''. \tag{2.25}$$

Applying the Favre filter to the governing equations results in additional terms which are described in the following. The filtered continuity equation results in

$$\frac{\partial \overline{\rho}}{\partial t} + \frac{\partial (\overline{\rho}\tilde{u}_j)}{\partial x_j} = 0. \tag{2.26}$$

Analogously, the modified momentum equation reads

$$\frac{\partial (\overline{\rho}\tilde{u}_i)}{\partial t} + \frac{\partial (\overline{\rho}\tilde{u}_i\tilde{u}_j)}{\partial x_j} = \frac{\partial}{\partial x_j}\left(\overline{\tau}_{ij} - \underbrace{\overline{\rho}\left(\widetilde{u_i u_j} - \tilde{u}_i\tilde{u}_j\right)}_{=\tau_{ij}^{sgs}} \right) - \frac{\partial \overline{p}}{\partial x_i} + \overline{\rho} g_i, \quad i = 1,2,3, \tag{2.27}$$

where $\overline{\tau}_{ij}$ is the stress tensor evaluated using the filtered velocity and τ_{ij}^{sgs} are the sgs stresses and their modelling is discussed in the next section. After applying the Favre filter to the transport equations of $\boldsymbol{\phi} = \{Y_1, \ldots, Y_{n_s}, h\}$ it holds

$$\frac{\partial \left(\overline{\rho}\tilde{\boldsymbol{\phi}}_\alpha\right)}{\partial t} + \frac{\partial \left(\overline{\rho}\tilde{u}_j\tilde{\boldsymbol{\phi}}_\alpha\right)}{\partial x_j} = \frac{\partial}{\partial x_j}\left(\overline{\rho}\mathcal{D}\frac{\partial \tilde{\boldsymbol{\phi}}_\alpha}{\partial x_j} - \underbrace{\overline{\rho}\left(\widetilde{u_j\boldsymbol{\phi}_\alpha} - \tilde{u}_j\tilde{\boldsymbol{\phi}}_\alpha\right)}_{=J_{\alpha,j}^{sgs}} \right) + \overline{\dot{\omega}}_\alpha, \tag{2.28}$$

where $J_{\alpha,j}^{sgs}$ are the sub-grid scale fluxes. The last term on the right hand side describes the filtered reaction term which represents a major challenge in turbulent combustion modelling. Different approaches to account for this term are discussed in Sec. 2.4.

2.2.5.2 Sub-grid scale models

Without any appropriate models for the unknown sub-grid scale expressions τ_{ij}^{sgs} and $J_{\alpha,j}^{sgs}$ the filtered transport equations introduced earlier are unclosed. One popular approach to model the sgs stresses is based on the Boussinesq assumption. The sub-grid scale stresses are proportional to the viscous stress tensor as

$$\tau_{ij}^{sgs} - \frac{1}{3}\tau_{kk}^{sgs}\delta_{ij} = -\mu_t \left(\frac{\partial \tilde{u}_i}{\partial x_j} + \frac{\partial \tilde{u}_j}{\partial x_i} - \frac{2}{3}\delta_{ij}\frac{\partial \tilde{u}_k}{\partial x_k} \right) = -2\mu_t \left(\tilde{S}_{ij} - \frac{1}{3}\tilde{S}_{kk}\delta_{ij} \right), \tag{2.29}$$

where μ_t is the turbulent viscosity coefficient. Based on the mixing length hypothesis of Prandtl, Smagorinsky [64] modelled the turbulent viscosity based on an algebraic expression via

$$\mu_t = (C_s \Delta_E)^2 \, \|\tilde{S}_{ij}\|, \tag{2.30}$$

where the norm of the stress tensor is given by

$$\|\tilde{S}_{ij}\| = \sqrt{2\tilde{S}_{ij}\tilde{S}_{ij}}. \tag{2.31}$$

Here, the Smagorinsky coefficient, C_s, is a model constant with a standard value of $C_s = 0.17$.

Within the scalar transport equation (cf. Eq. (2.28)) the sub-grid scalar fluxes are modelled based on the filtered scalar gradient via

$$J_{\alpha,j}^{sgs} = -\frac{\mu_t}{\mathrm{Sc}_t}\frac{\partial \tilde{\phi}_\alpha}{\partial x_j}, \tag{2.32}$$

where the turbulent Schmidt number is introduced.

2.3 Combustion

In this section details of the chemical source term in a chemical reaction are introduced. Afterwards, two different flame modes are presented, namely, the non-premixed and the premixed combustion.

2.3.1 Chemical reaction

Combustion is a chemical process, which releases energy. It results from a series of elementary reactions. The chemical conversion of n_s species in R reactions reads [79]

$$\sum_{\alpha=1}^{n_s} \nu'_{\alpha r} N_\alpha \longleftrightarrow \sum_{\alpha=1}^{n_s} \nu''_{\alpha r} N_\alpha, \quad r = 1, \ldots, R, \tag{2.33}$$

where N_α represents the corresponding symbol of species α. The stoichiometric coefficients of reactant species and product species are represented by $\nu'_{\alpha r}$ and $\nu''_{\alpha r}$, respectively. The reaction rate, $\mathcal{R}_r$ for reaction r is

$$\mathcal{R}_r = k_{f,r} \prod_{\alpha=1}^{n_s} (c_\alpha)^{\nu'_{\alpha r}} - k_{b,r} \prod_{\alpha=1}^{n_s} (c_\alpha)^{\nu''_{\alpha r}}, \tag{2.34}$$

where $k_{f,r}$ and $k_{b,r}$ are the forward and backward reaction rate coefficients of reaction r, respectively. The species concentration of species α is given by

$$c_\alpha = \frac{\rho Y_\alpha}{M_\alpha}, \tag{2.35}$$

where M_α is the molecular weight of species α. The forward reaction rate coefficients are exponentially dependent on the temperature, which is known as the modified Arrhenius law

$$k_{f,r} = A_r T^{\beta_r} \exp\left(-\frac{E_{a,r}}{R_u T}\right), \tag{2.36}$$

where A_r is the pre-exponential factor, β_r the temperature exponent and $E_{a,r}$ the activation energy. Summing up the contributions of each elementary reactions ends up in the chemical source term appearing in the species transport equation (cf. Eq. (2.5))

$$\dot{\omega}_\alpha (Y, T) = M_\alpha \sum_{r=1}^{R} \left(\nu''_{\alpha r} - \nu'_{\alpha r}\right) \mathcal{R}_r. \tag{2.37}$$

2.3.2 Flame modes

Depending on the state of the fuel (Fu) and oxidizer (Ox) prior to combustion two different flame modes are known. While in premixed combustion fuel and oxidizer are mixed before reaction occurs, in non-premixed combustion they are supplied separately to the flame.

Non-premixed combustion

In non-premixed (also called diffusion) flames fuel and oxidizer are injected into the combustion chamber separately. The flame characteristics are dominated by the degree of mixing, which is described by the mixture fraction, f. For a simple non-premixed flame with fuel in one stream and oxidizer in the other, the mixture fraction can be defined via

$$f = \frac{Z_i - Z_{i,\mathrm{Ox}}}{Z_{i,\mathrm{Fu}} - Z_{i,\mathrm{Ox}}}, \tag{2.38}$$

which is based on the elemental mass fraction of the ith element, Z_i. This definition is independent of the choice of the element, if the diffusivities are equal. Based on this definition, the mixture fraction can be transported by the following equation

$$\frac{\partial(\rho f)}{\partial t} + \frac{\partial(\rho u_j f)}{\partial x_j} = \frac{\partial}{\partial x_j}\left(\rho \mathcal{D} \frac{\partial f}{\partial x_j}\right). \tag{2.39}$$

Note, this equation is of the form of the generic scalar transport equation (cf. Eq. (2.13)), but does not contain any chemical source term. The mixture faction definition is based on elements, which are conserved. Another quantity to describe the level of mixing is the equivalence ratio, ϕ, which is related to the mixture fraction via [3]

$$\phi = \frac{f}{1-f}\frac{1-f_{\mathrm{st}}}{f_{\mathrm{st}}}, \tag{2.40}$$

where f_{st} is the stoichiometric mixture fraction.

Premixed combustion

In premixed combustion fuel and oxidizer are mixed prior to chemical reaction. Mixing and reaction can occur independently and the mixture fraction is not appropriate to describe the combustion process. In premixed combustion the normalized reaction progress variable, c, which ranges from zero in the unburnt gas to unity in the burnt gas, is a common parameter to describe the combustion progress. A common definition of the reaction progress variable is based on the temperature

$$c = \frac{T - T_u}{T_b - T_u}, \tag{2.41}$$

where T_u and T_b represent the burnt and unburnt temperature, respectively. Another definition of the reaction progress variable is based on the CO_2 mass fraction

$$c = \frac{Y_{\mathrm{CO_2}}}{Y^b_{\mathrm{CO_2}}}. \tag{2.42}$$

Figure 2.1 presents a sketch of laminar premixed flames for two different equivalence ratios. The profiles of the reaction progress variable depends on its definition i.e. the temperature (dashed purple line), the CO_2 mass fraction (red line) or the H_2O mass fraction (blue line)

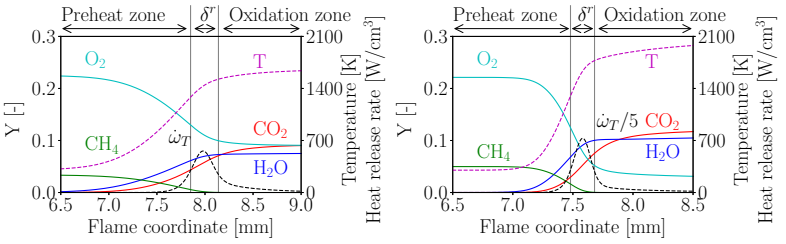

(a) $\phi = 0.6$ (b) $\phi = 0.9$

Figure 2.1: Sketch of laminar premixed flames for two different equivalence ratios.

Furthermore, the flame properties e.g. the peak temperature are controlled by the equivalence ratio. Furthermore, each premixed flame can be split into a preheat, reaction and oxidation zone. In the preheat zone diffusion preheats the mixture, which reacts chemically in the reaction zone, δ^r. Finally, slow chemical processes, e.g. NO_x formation occur in the oxidation zone. Besides the reaction zone thickness, which is the smallest thickness, there exists different definitions for flame length scales. One alternative definition of the flame thickness reads

$$\delta^u = \mathcal{D}_{\mathrm{th,u}}/s_L = \frac{\lambda_u}{\rho_u C_p s_L}, \tag{2.43}$$

where $\mathcal{D}_{\mathrm{th,u}}$ is the thermal diffusivity evaluated in the unburnt mixture and s_L is the laminar flame speed. δ^u is commonly stated as the diffusive thickness and may be evaluated easily before any computation. This thickness is usually much smaller than a common LES cell size. Another, more useful definition quantifies the spatial extent of the

whole flame structure and is given by

$$\delta^{\varphi} = \frac{|\varphi_b - \varphi_u|}{\max\left(\left|\frac{\partial \varphi}{\partial x}\right|\right)}. \tag{2.44}$$

Its definition is based on the burnt and unburnt state of property φ which is commonly chosen as temperature ($\varphi = T$) or CO_2 mass fraction ($\varphi = Y_{CO_2}$). As these properties vary for different equivalence ratios, the flame thickness is a function of the equivalence ratio. The chemical time scale is computed based on the laminar flame thickness and laminar flame speed via

$$\tau_{\text{chem}} = \frac{\delta_L}{s_L}, \tag{2.45}$$

where δ_L is the laminar flame thickness.

Stratification in premixed combustion

Stratified combustion refers to flame propagation through non-uniformly mixed reactants. Consequently, the flame front does not propagate through homogeneously mixed reactants, but rather through fluid with equivalence gradients. In stratified combustion the representing variables of the premixed and non-premixed combustion modes need to be combined. The flame front is tracked via e.g. the reaction progress and at the same time mixture fraction gradients need to be taken in consideration which can be represented by the mixture fraction. Variations in the mixture fraction control the flame speed. Investigations of relevant phenomena in stratified combustion have been conducted in various numerical and experimental studies. They are summarized by e.g. Masri [51] and Lipatnikov [49] , but this combustion mode is still topic of current research. In this work premixed combustion with

stratification is investigated and adequate models for turbulent reacting flows are presented in the next section.

2.4 Modelling of turbulent combustion

One of the major challenges in modelling turbulent combustion is the determination of the filtered chemical source term, $\overline{\dot{\omega}}_\alpha$, in Eq. (2.28). An overview and discussion on different combustion models which account for this challenge mainly in the LES context are presented. The application to premixed combustion (including stratified combustion) is discussed for each model.

2.4.1 Key challenge of combustion models

Independent of the combustion mode, the chemical source term introduced in Sec. 2.3.1 depicts a non-linear dependency on the species mass fractions and the temperature. This dependency is shown in Fig. 2.2. After applying the filter operator to the chemical source term in LES

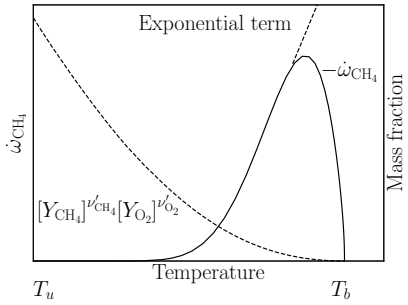

Figure 2.2: Sketch of a simplified reaction for the reactants mass fraction and chemical source term dependency on temperature. This figure is based on a figure published in [79].

(cf. Eq. (2.28)), the evaluation of the filtered chemical source term cannot be based on the filtered quantities

$$\overline{\dot{\omega}_\alpha(Y,T)} \neq \dot{\omega}_\alpha\left(\overline{Y},\overline{T}\right), \tag{2.46}$$

due to its non-linear dependency. The accurate prediction of the filtered source term is a big challenge in turbulent combustion modelling.

2.4.2 Regime diagram for turbulent premixed combustion

The approximation of the filtered reaction rate needs further details on the physics and the corresponding time and length scales. Turbulent premixed combustion regime diagrams schematically represent the correlations of these scales. The diagrams range from flamelets to distributed reaction zones and are based on non-dimensional numbers. The Damköhler number, Da, defines the ratio of a turbulent time scale at the integral (largest) length scale, τ_t, and the chemical time scale, τ_{chem}, as

$$\text{Da} = \frac{\tau_t}{\tau_{\text{chem}}}. \tag{2.47}$$

The Karlovitz number, Ka, is defined as

$$\text{Ka} = \frac{\tau_{\text{chem}}}{\tau_\eta}, \tag{2.48}$$

and relates the chemical time scale with the turbulent time scale at Kolmogorov scale, τ_η. With the assumption of $\text{Pr} = 1$ the Karlovitz number can be expressed via the characteristic length scales

$$\text{Ka} = \frac{\delta^2}{\eta^2}. \tag{2.49}$$

Based on these non-dimensional numbers different combustion regimes of turbulent premixed combustion were proposed in literature. Figure 2.3 shows a regime diagram based on the diagram published by Peters [54]. The abscissa depicts the integral length scale, l_t, normal-

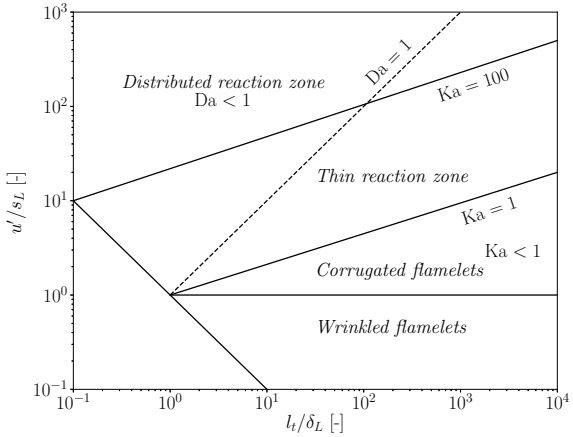

Figure 2.3: Classification of different combustion regimes of turbulent premixed combustion based on the regime diagram proposed by Peters [54].

ized with the laminar flame thickness and the ordinate states the velocity fluctuations, u', normalized with the laminar flame speed, s_L. For $\mathrm{Ka} < 1$ the smallest turbulent length scales are bigger than the flame thickness and cannot enter the flame front. Depending on the turbulence level u'/s_L the regimes are separated into the *wrinkled flamelets* and *corrugated flamelets* regime, while in both the flame structure is not altered by turbulence. In the *thin reaction zone* regime, the chemical time scales are larger than the time scales based on the Kolmogorov scales ($1 < \mathrm{Ka} < 100$) due to increased turbulence levels. The flame structure can be modified due to turbulence within the preheat zone,

but not within the reaction zone. With the approximation that the reaction zone is 1/10 of the total flame thickness [55], the upper boundary of this regime is Ka $\approx$ 100. This boundary depicts the transition into the *distributed reaction zone* regime in which both, the preheat and the reaction zones are altered by turbulence. In the following section popular combustion models are introduced and their applicability to combustion setups in the different regimes within the premixed combustion regime diagram are discussed.

2.4.3 Flamelet model

The flamelet model is based on the assumption that a turbulent flame can be considered as an ensemble of locally laminar flames. The reactive scalars, e.g. temperature and species mass fractions are characterized in terms of a low dimensional manifold and are evaluated based on a precomputed chemistry table. In non-premixed applications the mixture fraction is chosen as such a characteristic variable and describes the flame structure via a locally 1-D flame normal to the stoichiometric contour. The scalar dissipation rate, χ_f, characterizes fluid strain which can affect the flame front. It can be used as an additional parameter to access the table. The filtered quantity is obtained via the probability density function (PDF)

$$\widetilde{\phi}_\alpha = \int_0^\infty \int_0^1 \phi_\alpha(f, \chi_f) P(f, \chi_f) df d\chi_f, \tag{2.50}$$

while the statistical independence of f and χ_f given by $P(f, \chi_f) = P(f)P(\chi_f)$ is usually assumed. The presumed PDF for mixture fraction is often chosen to be a β-distribution and for the scalar dissipation rate a log-normal distribution [79]. An alternative variable to characterize the thermo-physical states is necessary in premixed combustion.

A variable representing reaction progress is needed and its transport equation holds a chemical source term which additionally needs to be obtained via the flamelet table. In the flamelet generated manifolds (FGM) approach [78] the chemical source term of the reaction progress variable and the species composition are parameterized by mixture fraction and reaction progress where the former is necessary to account for the stratification. The variables representing the chemical states properly are called controlling variables. In addition to the flow governing equations, balance equations (cf. Eq.(2.28)) for these controlling variables (mixture fraction and progress variable) are solved. Freely propagating premixed flames of different equivalence ratios are computed a priori to any simulation to create a two-dimensional chemistry table. Based on mixture fraction and reaction progress the chemical source term of the reaction progress variable and the species composition are read from this chemistry table. Only applications within the flamelet regime are reasonably predicted without any additional treatment. The application to turbulent premixed combustion with stratification was investigated by Auzillon *et al.* [1].

2.4.4 G-equation

The G-equation is a popular technique for large eddy simulations of turbulent premixed combustion. In the G-equation approach the flame thickness is set to zero and the flame propagates with a prescribed velocity. The scalar $G(x,t)$ tracks the instantaneous flame surface as presented in Fig. 2.4. The G-equation in LES is given by [54]

$$\frac{\partial\left(\overline{\rho}\widetilde{G}\right)}{\partial t}+\frac{\partial\left(\overline{\rho}\widetilde{u}_j\widetilde{G}\right)}{\partial x_j}=\rho_u\overline{s}_T\left|\nabla\overline{G}\right|, \tag{2.51}$$

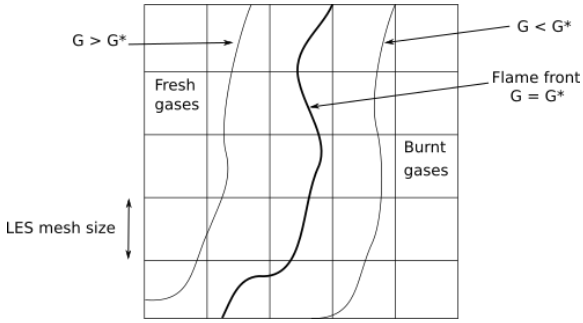

Figure 2.4: Flame front and G-field. This figure is based on a figure published in [55].

where ρ_u is the unburnt density and $\overline{s}_T$ is the sub-grid scale flame speed. A common model to prescribe $\overline{s}_T$ reads

$$\frac{\overline{s}_T}{s_L} = 1 + \alpha \left(\frac{\overline{u'}}{s_L} \right)^n , \tag{2.52}$$

where α and n are model parameters close to unity. The model is applicable to thin flame structures of a well known burning velocity and a model universality within the premixed regime diagram is not given. To account for stratification in turbulent premixed combustion Trisjono *et al.* [77] coupled tabulated chemistry based on mixture fraction and reaction progress variable with the G-equation. Through the coupling with the G-equation the correct propagation velocity was ensured.

2.4.5 Flame surface density approach

The flame surface density (FSD) approach is based on the transport equation of the progress variable. Compared to the G-equation which specifies an arbitrary field the progress variable, c, and flame surface

densities are physically defined and could be obtained from DNS data. The balance equation of the filtered reaction progress variable for LES reads [4]

$$\frac{\partial(\overline{\rho}\widetilde{c})}{\partial t} + \frac{\partial(\overline{\rho}\widetilde{u}_j\widetilde{c})}{\partial x_j} + \frac{\partial}{\partial x_j}\left(\overline{\rho}\widetilde{u_j c} - \overline{\rho}\widetilde{u}_j\widetilde{c}\right) = \frac{\partial}{\partial x_j}\left(\overline{\rho}\mathcal{D}\frac{\partial\widetilde{c}}{\partial x_j}\right) + \overline{\dot{\omega}}_c = \overline{\rho s_d|\nabla c|}, \tag{2.53}$$

where s_d is the displacement speed of the iso-surface c. To resolve the thin flame front on the LES mesh, Boger *et al.* [4] resolved the flame front with a filter size larger than the computational grid resolution. The right hand side in Eq. (2.53) may be modelled as

$$\overline{\rho s_d|\nabla c|} \approx \rho_u s_L \Sigma = \rho_u s_L E|\nabla\overline{c}|, \tag{2.54}$$

where Σ represents the sub-grid scale flame surface density and E the sub-grid scale flame wrinkling. Both properties, Σ and E, need to be modelled. The flame front is assumed to be thin and effects of finite rate chemistry that may lead to deviations from a laminar flame structure are typically neglected. The application to regimes across the entire premixed regime diagram is consequently not given. Marincola *et al.* [50] applied the FSD approach to turbulent stratified flames. The stratification was treated by solving an additional transport equation for the mixture fraction.

2.4.6 Artificially thickened flame approach

Usually, the LES resolution is too coarse to resolve the thin premixed flame front. Through the artificially thickened flame (ATF) approach the flame can be resolved adequately as illustrated in Fig. 2.5. This idea was developed by Butler and O'Rourke [5] and realized by an

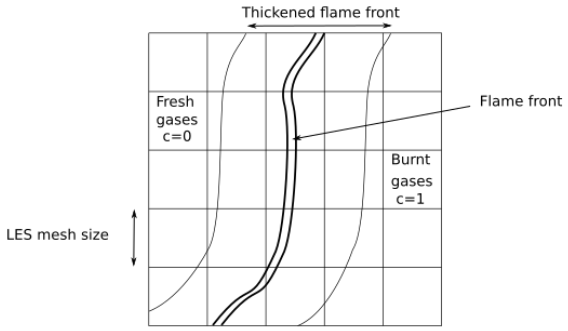

Figure 2.5: Illustration of the artificially thickened flame approach. This figure is based on a figure published in [55].

increase of the molecular diffusion through a thickening factor, F. At the same time the reaction source term is divided by this thickening factor to keep the flame speed constant, because it holds [86]

$$s_L \propto \sqrt{\mathcal{D}\dot{\omega}}, \tag{2.55}$$

and for the laminar flame thickness

$$\delta_L \propto \sqrt{\mathcal{D}/\dot{\omega}}. \tag{2.56}$$

The diffusion as well as the source term are multiplied by the efficiency function, E, to compute the correct flame propagation speed. The transport equations introduced in Eqs. (2.28) are modified in the

following way

$$\frac{\partial\left(\overline{\rho}\widetilde{\phi}_\alpha\right)}{\partial t}+\frac{\partial\left(\overline{\rho}\widetilde{u}_j\widetilde{\phi}_\alpha\right)}{\partial x_j}=\frac{\partial}{\partial x_j}\left(\left[FE\overline{\rho}\mathcal{D}+(1-\Omega)\frac{\mu_t}{\mathrm{Sc}_t}\right]\frac{\partial\widetilde{\phi}_\alpha}{\partial x_j}\right)+\frac{E}{F}\dot{\omega}_\alpha. \tag{2.57}$$

The flame sensor, Ω, is given by

$$\Omega=16[\widetilde{c}(1-\widetilde{c})]^2 \quad \text{with} \quad \widetilde{c}=\frac{\widetilde{Y}_{\mathrm{CO}_2}}{Y^{\mathrm{eq}}_{\mathrm{CO}_2}(\widetilde{f})}, \tag{2.58}$$

where $\widetilde{c}$ is the reaction progress variable, $Y^{\mathrm{eq}}_{\mathrm{CO}_2}$ is the equilibrium value of $\widetilde{Y}_{\mathrm{CO}_2}$ and is a function of the mixture fraction. The flame sensor limits the thickening procedure to the flame front and the method used here is known as the dynamic thickening approach [20]. The thickening factor can be determined based on the flame sensor via

$$F=1+(F_{\max}-1)\,\Omega, \tag{2.59}$$

where the maximum thickening factor, $F_{\max}$, is computed locally (cell based) as

$$F_{\max}=\max\left(1,\frac{\Delta_E}{\Delta_{E,\max}}\right). \tag{2.60}$$

The resolution $\Delta_{E,\max}$ is obtained from one-dimensional laminar flame simulations and guarantees a correct laminar flame speed for this resolution. In Eq. (2.57) the efficiency function, E, is introduced, which accounts for the lost wrinkling by the thickening approach. Colin *et al.* [13] first proposed a model for the efficiency function obtained by DNS results. Charlette *et al.* [10] improved the efficiency function approach by reducing the model coefficients. The efficiency function is modelled in the following way

$$E\left(F,\frac{u'_\Delta}{s_L}\right)=\left(1+\min\left[F,\Gamma\frac{u'_\Delta}{s_L}\right]\right)^{\gamma}, \tag{2.61}$$

where the laminar flame speed, s_L, is obtained locally via the mixture fraction. The sub-grid velocity fluctuations u'_Δ are modelled via [13]

$$u'_\Delta=2\Delta_E^3|\nabla\times(\nabla^2 u)|. \tag{2.62}$$

The function Γ is given by

$$\Gamma\left(F,\frac{u'_\Delta}{s_L}\right)=\left[((f_u^{-a}-f_\Delta^{-a})^{-1/a})^{-b}+f_{\mathrm{Re}}^{-b}\right]^{-1/b}, \tag{2.63}$$

with

$$f_u=4\left(\frac{27C_k}{110}\right)^{1/2}\left(\frac{18C_k}{55}\right)\left(\frac{u'_\Delta}{s_L}\right)^2, \tag{2.64}$$

$$f_\Delta=\left[\frac{27C_k\pi^{4/3}}{110}\left(F^{4/3}-1\right)\right]^{1/2}, \tag{2.65}$$

$$f_{\mathrm{Re}}=\left[\frac{9}{55}\exp\left(-\frac{3}{2}C_k\pi^{4/3}\,\mathrm{Re}_\Delta^{-1}\right)\right]^{1/2}\mathrm{Re}_\Delta^{1/2}, \tag{2.66}$$

$$a=0.6+0.2\exp\left[-0.1\left(\frac{u'_\Delta}{s_L}\right)\right]-0.2\exp\left[-0.01F\right], \tag{2.67}$$

where $\mathrm{Re}_\Delta=4Fu'_\Delta/s_L$ is the sub-grid turbulent Reynolds number. Originally, the model parameters are given by $b=1.4$, $C_k=1.5$ and $\gamma=0.5$ (cf. Eq. (2.61)). Charlette *et al.* [11] further introduced a dynamic computation of γ, but the increased computational cost do not justify the (slightly) improved results. The application of the ATF model is not restricted to any regime within the premixed regime diagram, but the model performance depends on the proper estimation of the thickening factor and the efficiency function. While the ATF model

was originally introduced for premixed combustion, this approach can also be applied to non-premixed combustion. The flame sensor reverts the equations to the standard LES equations outside the flame as $\Omega = 0$. Hence, the ATF model can be applied to stratified combustion. The coupling of ATF with FGM (parametrization of the chemical state by mixture fraction and reaction progress) models turbulent stratified combustion and was applied successfully to various setups in the literature [42]. Further details of this approach are presented in the next chapter contributing to the MMC model introduced in this work.

2.4.7 Transported probability density function models

In transported PDF approaches (or *filtered density function (FDF)* methods within the LES framework), a probabilistic treatment is applied to the LES sub-filter scales. The major advantage of the FDF method is that the chemical source term is closed and no additional approximation needs to be introduced for the modelling of the effects of sub-grid turbulence on the chemical conversion process: thus, the FDF method presents a model that is not confined to a specific combustion regime and can - in principle - be applied to non-premixed, premixed and mixed combustion modes without any major modifications.

The turbulent composition scalar field, $\boldsymbol{\phi}$, may be represented by a filtered mass density function, F_L, which is given by

$$F_L(\boldsymbol{\psi}; x, t) = \int_{-\infty}^{+\infty} \rho(x', t)\zeta[\boldsymbol{\psi}, \boldsymbol{\phi}(x', t)]G(x' - x, \Delta_E)dx', \qquad (2.68)$$

where $\boldsymbol{\psi}$ is the sample space of $\boldsymbol{\phi}$ and the fine-grained density, ζ, is

given by

$$\zeta[\boldsymbol{\psi}, \boldsymbol{\phi}(x,t)] = \delta[\boldsymbol{\psi} - \boldsymbol{\phi}(x,t)] = \prod_{\alpha=1}^{n_s+1} \delta[\psi_\alpha - \phi_\alpha(x,t)], \tag{2.69}$$

where δ is an (n_s+1)-dimensional delta function. Applying gradient models for the conditional velocity and diffusion fluxes the transport equation for F_L reads [14, 31]

$$\frac{\partial F_L}{\partial t} + \frac{\partial}{\partial x_i}\left(\tilde{u}_i F_L - \overline{\rho}(\mathcal{D}+\mathcal{D}_t)\frac{\partial F_L/\overline{\rho}}{\partial x_i}\right) + \frac{\partial(\dot{\omega}_\alpha(\boldsymbol{\psi})F_L)}{\partial \psi_\alpha} = \tag{2.70}$$

$$-\frac{\partial^2}{\partial\psi_\alpha\partial\psi_\beta}\left(\overline{\rho\mathcal{D}\,\frac{\partial\boldsymbol{\phi}_\alpha}{\partial x_i}\frac{\partial\boldsymbol{\phi}_\beta}{\partial x_i}\,\middle|\,\boldsymbol{\psi}}F_L/\overline{\rho}\right). \tag{2.71}$$

The term on the right hand side describes the conditional sub-filter scalar dissipation, which needs to be modelled in FDF approaches. For detailed chemistry, n_s is high and a solution of the joint composition FDF transport equation in the Eulerian framework leads to significant computational cost. Instead, solving an equivalent system of stochastic differential equations that govern the evolution of Lagrange particles, each representing an instantaneous and local realization of the composition field within the turbulent reactive flow, reduces the computational cost. The equations that govern the evolution of an ensemble of Lagrangian particles read [12, 56]

$$dx_i^p = \left[\widetilde{u}_i + \frac{1}{\overline{\rho}}\frac{\partial(\overline{\rho}\mathcal{D}_{\text{eff}})}{\partial x_i}\right]^p dt + \left[\sqrt{2\mathcal{D}_{\text{eff}}}\right]^p d\omega_i, \tag{2.72}$$

$$d\phi_\alpha^p = (\dot{\omega}_\alpha^p + S_\alpha^p)\,dt. \tag{2.73}$$

The superscript $(\cdot)^p$ specifies stochastic particle properties, such as the particle position, x^p, and the particle composition, ϕ_α^p, where the index

$\alpha = 1, \ldots, n_s+2$ includes all reactive scalars, enthalpy and mixture fraction. In Eq. (2.72) the filtered velocity, $\widetilde{u}_i$, density, $\overline{\rho}$, and the effective diffusivity, $\mathcal{D}_{\text{eff}} = \mathcal{D} + \mathcal{D}_t$, are obtained from the LES and interpolated to the particle position. The increment of a stochastic Wiener process is given by $d\omega_i$. In Eq. (2.73) $\dot{\omega}_\alpha^p$ denotes the chemical source term and S_α^p is the unclosed mixing operator. The model does not require any closure assumptions with respect to the expected flame regime and is by its definition per se applicable to different combustion setups across the premixed regime diagram. The choice of the mixing model can influence the flame front. The application of conventional mixing models to thin premixed flames, i.e. flames that are within the flamelet regime, can be questioned as these models do not avoid particles to mix across the flame front. In this work the modelling of the mixing operator is accomplished via the MMC mixing model which conditions the mixing operator to overcome this deficiency. Details of this model are introduced in the following chapter.

2.5 Summary

This chapter presents the fundamental equations governing reacting flow. Different approaches are available to account for the turbulent scales affecting the flow field in inert mixtures. Common approaches are introduced and further details of the promising LES method are presented. Moving to reacting flows, an introduction to chemical reaction is given. It is useful to distinguish the two combustion modes: (i) non-premixed and (ii) premixed combustion. Stratification in premixed combustion is associated with flame propagation through non-uniformly mixed reactants. The combination of reacting fluid with turbulence requires advanced models. Popular models for turbulent premixed combustion are presented and their applicability to stratified

combustion are discussed. Useful features of the PDF method with the basic concepts of a mapping closure for the modelling of the turbulent mixing term are combined in the multiple mapping conditioning mixing model. Details of the MMC mixing model and the novel version for turbulent premixed combustion are presented in the next chapter.

Chapter 3

Multiple mapping conditioning for turbulent premixed combustion

Within this chapter the multiple mapping conditioning (MMC) mixing model for turbulent combustion is introduced. The background and available versions in literature are summarized to present a basic overview of MMC in Sec. 3.1. Generalized MMC based on a sparse particle distribution in the LES context is introduced in detail in Sec. 3.2, because it represents the base of the MMC model investigated in this work. Following the basic principles of generalized MMC, the novel MMC model coupled with the ATF approach for turbulent premixed combustion with stratification is explored in Sec. 3.3. In the context of

premixed combustion the choice of the reference space is discussed and the corresponding mixing time scale model is reviewed.

3.1 Background

Originally, MMC was introduced by Klimenko and Pope [37]. MMC is a modelling framework for the closure of the conditional sub-filter scalar dissipation as any conventional mixing model. A common feature of all MMC realisations is the introduction of mathematically independent reference variables that are used to achieve localness of mixing in composition space. The two different versions, the original and the generalized MMC approach, are available. For the original MMC version [37] there exists deterministic and stochastic implementations. The deterministic MMC approach is closely related to the conditional moment closure (CMC), while the stochastic MMC approach is based on a Lagrangian formulation where the mixing models are based on the conditional expectations. Different stochastic versions were coupled to RANS [69, 82, 83, 84] and LES [12, 27, 53] of the turbulent flow field. Generalized MMC was first proposed by Klimenko [36]. Compared to the original version this approach is less restrictive and bases upon a Lagrangian formulation. The technique of determining the reference variables is different for the generalized MMC approach, which allows for the evolution of a non-Markov process of the reference variables. Cleary and Klimenko introduced generalized MMC for LES where the reference variable is given by properties with physical meaning and interpolated from the Eulerian field to the particle position. They investigated turbulent non-premixed flames [12] with the Eulerian mixture fraction as reference variable. It should be noted, that the independence of the reference variable and the particle property need to be guaranteed, i.e. in non-premixed combustion the Eulerian mixture fraction is

mathematically independent from the mixture fraction solved for the particle. Using the LES-filtered mixture fraction as a reference variable has led to good results for a number of applications [29, 52, 53]. Specific implementation issues are summarized by Galindo Lopez *et al.* [25]. In premixed applications the definition of a suitable reference variable is not that obvious. One LES approach using a reference variable similar to a shadow position with a dense particle distribution [24, 74] has been published so far. The current work follows more closely the generalized MMC approach with a sparse particle distribution [12] which was mostly applied to non-premixed combustion so far. Details of generalized MMC with a sparse particle distribution are introduced in the next section.

3.2 Generalized multiple mapping conditioning with sparse particle distribution

To get a better overview the equations governing the evolution of the Lagrangian particles, which were introduced in the previous chapter, are repeated here

$$dx_i^p = \left[\widetilde{u}_i + \frac{1}{\overline{\rho}}\frac{\partial(\overline{\rho}\mathcal{D}_{\text{eff}})}{\partial x_i}\right]^p dt + \left[\sqrt{2\mathcal{D}_{\text{eff}}}\right]^p d\omega_i, \tag{2.72}$$

$$d\phi_\alpha^p = (\dot{\omega}_\alpha^p + S_\alpha^p)\, dt. \tag{2.73}$$

The equivalent system of stochastic differential equations solves the joint scalar FDF transport equation indirectly. The FDF is represented by a sparse set of stochastic particles where "sparse" means that the number of stochastic particles, N_p, is less than the number of LES cells.

The low number of particles is realizable, because mixing is localized in physical space and the reference space. The unclosed mixing operator, S_α^p, is modelled via a mixing model. A valuable mixing model should [73]

1. conserve the mean values of the composition,
2. predict the correct variance decay,
3. be linear and independent with respect to the composition values,
4. relax to a Gaussian distribution in statistically homogeneous systems (for an inert scalar) and
5. be local in composition space.

The mixing models interaction by exchange with the mean (IEM) [6, 17] and modified Curl's (MC) [32] conserve the mean values and predict the correct decay of variance, but have drawbacks in that they do not relax to a Gaussian and are not local in composition space. The Euclidean minimum spanning tree (EMST) [73] additionally is local in composition space, but is not linear and independent with respect to composition values. The MMC mixing model is a model that accounts for localness in compositions space and it complies with independence and linearity principles. The localness in composition space of the MMC mixing model is accomplished by conditioning the mixing particles in reference space. This can be ensured through the correct choice of the reference variable space. The particle pairs are chosen in such a way that mixing partners (p, q) are close in reference variable space, $\boldsymbol{\xi}$, and in physical space, $\boldsymbol{x}$. This is realized by minimizing the effective square distance

$$\left(\hat{d}^{p,q}\right)^2 = \sum_{i=1}^{3} \left(\frac{d_{x_i}^{p,q}}{r_m/\sqrt{3}}\right)^2 + \sum_{j=1}^{N_\xi} \left(\frac{d_{\xi_j}^{p,q}}{\xi_{j,m}}\right)^2, \tag{3.1}$$

where N_ξ is the number of reference variables. Here, $d_\psi^{p,q} = |\psi^p - \psi^q|$ represents the magnitude of the difference of the corresponding property ψ for a particle pair (p,q), where $\psi \in \{x_1, x_2, x_3, \xi_1, \ldots, \xi_{N_\xi}\}$. For small enough relative values of the localness parameters $\xi_{j,m}$ and r_m the mixing partners (p,q) are close in reference variable space, $\boldsymbol{\xi}$, and in physical space, $\boldsymbol{x}$, respectively. To minimize the effective square distance, a k-d tree algorithm is implemented [23]. All particles within the computational domain are grouped into particle pairs and once these pairs (p,q) have been determined, the particles are mixed by the modified Curl's mixing model over a finite time step Δt using

$$\boldsymbol{\phi}_\alpha^p(t+\Delta t) = \boldsymbol{\phi}_\alpha^p(t) + \gamma(\overline{\boldsymbol{\phi}}_\alpha^{p,q}(t) - \boldsymbol{\phi}_\alpha^p(t)), \tag{3.2}$$

$$\boldsymbol{\phi}_\alpha^q(t+\Delta t) = \boldsymbol{\phi}_\alpha^q(t) + \gamma(\overline{\boldsymbol{\phi}}_\alpha^{p,q}(t) - \boldsymbol{\phi}_\alpha^q(t)), \tag{3.3}$$

where particle pairs mix linearly towards their mean, $\overline{\boldsymbol{\phi}}_\alpha^{p,q}$, and $\gamma = 1 - \exp(-\Delta t/\tau_L)$ is the extent of mixing defined via a mixing time scale, τ_L, which is further discussed in Sec. 3.3.3.3. To ensure localness in composition space, the reference space needs to be chosen adequately. In this generalized MMC approach the reference space is obtained based on the Eulerian solution which is obtained simultaneously to the particle solution. For consistency of the Eulerian and the MMC fields, the particle density is coupled to the Eulerian fields. Care has to be taken, because a direct coupling from the particles to the LES cells is not feasible due to the sparse particle distribution. A common approach in MMC for non-premixed combustion is the coupling via an equivalent enthalpy [25].

3.3 MMC coupled with an artificially thickened flame model for turbulent premixed combustion

The novel MMC approach which is introduced in this work follows the basic concept of the previously presented generalized MMC approach while the reference space needs to be adapted for turbulent premixed combustion. The LES-filtered reaction progress variable is introduced as a suitable conditioning variable to prevent mixing over the flame front. For stratified combustion additional conditioning on mixture fraction is introduced to account for stratification layers. Further differences compared to the model introduced in the previous section which is mainly applied for non-premixed combustion are explicitly stated.

3.3.1 The transport equations

For the computation of the reference variables for turbulent premixed combustion with stratification, two models which are presented in the previous chapter are coupled. Through the artificial thickening of the flame front the flame is resolved on the LES grid and can be coupled with tabulated chemistry via the FGM approach (ATF-FGM). These approaches are outlined in Secs. 2.4.3 and 2.4.6, respectively. In ATF-FGM the standard Eulerian LES equations for mass, momentum and the two reference fields (namely, reaction progress and mixture fraction) are solved. As in previous publications of ATF-FGM [42], the CO_2 mass fraction is used to represent reaction progress here. The ATF model achieves closure by increasing the molecular diffusion such that the reaction zone is sufficiently broadened and resolved by the LES grid. While in Sec. 2.4.6 the transport equations for every species

mass fraction are introduced, the following equations state the modified transport equations for the controlling variables in ATF-FGM [42, 43]

$$\frac{\partial\left(\overline{\rho}\widetilde{Y}_{\mathrm{CO_2}}\right)}{\partial t}+\frac{\partial\left(\overline{\rho}\widetilde{u}_i\widetilde{Y}_{\mathrm{CO_2}}\right)}{\partial x_i}=\frac{\partial}{\partial x_i}\left(\left[FE\overline{\rho}\mathcal{D}+(1-\Omega)\frac{\mu_t}{\mathrm{Sc}_t}\right]\frac{\partial\widetilde{Y}_{\mathrm{CO_2}}}{\partial x_i}\right)+\frac{E}{F}\dot{\omega}_{\mathrm{CO_2}}, \tag{3.4}$$

and

$$\frac{\partial\left(\overline{\rho}\tilde{f}\right)}{\partial t}+\frac{\partial\left(\overline{\rho}\widetilde{u}_i\tilde{f}\right)}{\partial x_i}=\frac{\partial}{\partial x_i}\left(\left[FE\overline{\rho}\mathcal{D}+(1-\Omega)\frac{\mu_t}{\mathrm{Sc}_t}\right]\frac{\partial\tilde{f}}{\partial x_i}\right). \tag{3.5}$$

The thickening factor, F, is chosen as introduced in Eq. (2.59) and the flame is nominally resolved by 10 LES cells. The efficiency function, E, accounts for the correct turbulent flame speed and is modelled via the formulation proposed by Charlette *et al.* [10] introduced in Sec. 2.4.6. The thickening is applied only within the flame front which is realized via the flame sensor defined in Eq. (2.58) based on the reaction progress variable. To include detailed chemistry but preserve low computational cost for the computation of the reference fields, an FGM [78] is applied to close the reaction source term of the CO_2 mass fraction, $\dot{\omega}_{\mathrm{CO_2}}$, in Eq. (3.4). This chemical source term and the species composition are parameterized by mixture fraction and reaction progress where the former is necessary to account for the stratification. A two-dimensional chemistry table is created a priori to any simulation from freely propagating premixed flames of different equivalence ratios. Diffusive fluxes across mixture fraction gradients are neglected as these simulations are computed independently [44]. Outside the flammability limits the mass fractions are obtained via extrapolation. They are assumed to evolve by pure mixing i.e. without chemical reaction. Hence the mass frac-

tions are linear functions of the mixture fraction [44]. During run-time, the chemical source term, the species composition and the density are read from this two-dimensional chemistry table, which is based on the GRI-Mech 3.0 kinetic scheme [65] using unity Lewis numbers. The unity Lewis number assumption is in line with common practice for modelling this flame [22]. De Swart *et al.* [15] showed that preferential diffusion of the different species can have opposing effects and cancel each other in methane-air mixtures like those investigated here. An effective Lewis number near unity is a sufficiently accurate approximation. It is noted here, that the ATF-FGM model described up to now is a well established and stand-alone model. Further details on the ATF-FGM model can be found in the literature [42].

Coupling the ATF model for the reference variables with the MMC approach for the reactive sub-filter scale fluctuations (MMC-ATF) requires the solution of the joint scalar FDF which models deviations of the flame from the flamelet structure across all premixed flame regimes. Figure 3.1 gives an overview of the interaction of the Eulerian framework (left) and the Lagrangian approach (right). The reference variables, flow field properties for the particle movement and the mixing time scale are transferred from the Eulerian grid to the Lagrangian particles. The figure also indicates that the FDF transport equation is solved via the stochastic differential equations given by Eqs. (2.72) and (2.73). The Eulerian solution based on FGM is used in the particle method for conditioning the mixing operator and finite rate chemistry is directly integrated on the particles. Details of the MMC mixing model required for S_α in premixed combustion are introduced in Sec. 3.3.3.

It is emphasized here that the ATF-FGM model is a flamelet approach and the flamelet table is needed for closure of the source term for the filtered reaction progress, i.e. there is no imminent need for backward coupling from the stochastic particles to the Eulerian frame-

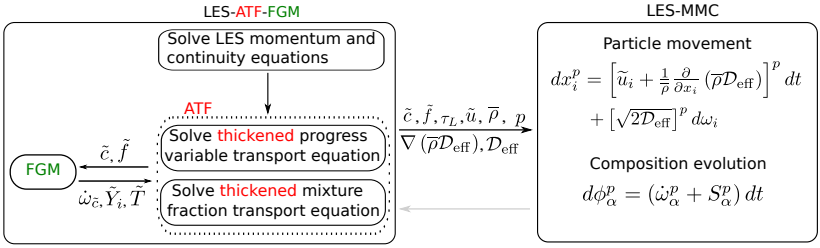

Figure 3.1: Schematic of the coupling relationship between the submodels LES, ATF, FGM and MMC.

work (illustrated by the grey arrow in Fig. 3.1) if the flame is within the flamelet regime. Only if the flame structure deviated strongly from a flamelet, the flamelet table would provide inaccurate closure of the LES-filtered chemical source term and backward coupling of the (more accurate) stochastic particle solution to the LES-filtered field would be needed. To achieve such backward closure the filtered chemical source term and density could be mapped from the particle solution onto the LES grid but care would need to be taken as the LES-filtered reaction progress variable is artificially thickened while the particle solution represents a thin flame. Backward coupling is beyond the scope of this work and deferred to future work. For now, this places the model's application close to the flamelet regime where the conditional density does not deviate too much from the flamelet structure. This certainly limits its application. Flames close to the flamelet regime serve, however, as stringent first test cases as MMC shall be designed to avoid unphysical mixing across the flame front that would be inherent to conventional PDF methods. For the application investigated here, $\tilde{c}$ is only used for conditioning of mixing and flame characteristics are extracted from the particle solution, extinction levels are quite low and the ATF-FGM approach should provide a sufficiently accurate approximation of the

density, the reference and the flow fields.

3.3.2 MMC correlation

The reference variables represent physical quantities and a particle can be associated with specific values of (i) the filtered reaction progress variable, $\tilde{c}$, and (ii) the filtered mixture fraction, $\tilde{f}$. The reference variables are provided by the Eulerian solution and interpolated to the particle position. At the same time there exist the actual (local and instantaneous) stochastic particle solutions obtained by Eq. (2.73) for the CO_2 mass fraction and the mixture fraction, z^p, respectively, on the stochastic particles. The CO_2 mass fraction can be normalized for each particle in the same manner as $\tilde{c}$ (see Eq. (2.58)) and is denoted in the following by θ^p. The actual particle values θ^p and z^p should not be confused with the interpolated LES-filtered values $\tilde{c}(x^p)$ and $\tilde{f}(x^p)$. Reaction progress and mixture fraction are thus computed twice, once within the Eulerian framework and once for the particles. The reference variables and the corresponding properties are mathematically independent, but need to be correlated as otherwise the conditioning of mixing in reference space would not yield localization in composition space.

3.3.3 MMC mixing model

Within this approach the mixing model is also specified by the modified Curl's mixing model in which particle pairs mix linearly towards their mean as described in Eqs. (3.2) and (3.3). MMC specific details for turbulent premixed combustion are presented in the following.

3.3.3.1 Particle pair selection

As mentioned above, the key feature of MMC is the introduction of reference variables to enforce mixing localness in this reference variable space. As MMC is a high-quality mixing model which is designed to fulfill important mixing model principles as localness, linearity and independence, it can be applied in a sparse particle distribution framework. Mixing over larger physical distances, which can occur due to the sparse particle distribution, does not -per se- lead to unphysical solutions. However, if mixture compositions of these selected particles differ too much, then a shear layer or flame front may lie inbetween the particles and mixing of these particles leads to unphysical results. This can be alleviated by conditioning on the reference fields. The reference variables are obtained from the LES as $\boldsymbol{\xi}^p = \{\tilde{c}\}(\boldsymbol{x}^p)$ in the *singly conditioned* MMC model. The model including mixture fraction ($\boldsymbol{\xi}^p = \{\tilde{c}, \tilde{f}\}(\boldsymbol{x}^p)$) is called in the following the *doubly conditioned* MMC approach. The conditioning of mixing particles in reaction progress variable space relates the particles to their relative position with respect to the flame and prevents undesired mixing across the flame front. The conditioning on mixture fraction prevents mixing across the stratification and shear layers.

It follows that the particle pairs are chosen in such a way that mixing partners (p, q) are close in progress variable space, $\tilde{c}$, in mixture fraction space, $\tilde{f}$ (in doubly conditioned MMC) and in physical space, $\boldsymbol{x}$. The effective square distance introduced in Eq.(3.1) reads for pre-

mixed combustion with stratification

$$\left(\hat{d}^{p,q}\right)^2 = \underbrace{\sum_{i=1}^{3}\left(\frac{d^{p,q}_{x_i}}{r_m/\sqrt{3}}\right)^2 + \underbrace{\left(\frac{d^{p,q}_{\tilde{c}}}{c_m}\right)^2}_{\text{single conditioning}} + \left(\frac{d^{p,q}_{\tilde{f}}}{f_m}\right)^2}_{\text{double conditioning}}. \tag{3.6}$$

This expression states the two last terms on the right hand side based on the reference variables $\tilde{c}$ and $\tilde{f}$. Here again, $d^{p,q}_{\psi} = |\psi^p - \psi^q|$ represents the magnitude of the difference of the corresponding property ψ for a particle pair (p, q) and $\psi \in \{x_1, x_2, x_3, \tilde{c}, \tilde{f}\}$. The values of the localness parameters c_m, f_m and r_m specify if the mixing partners (p, q) are close in reference progress variable space, $\tilde{c}$, in reference mixture fraction space, $\tilde{f}$, and in physical space, $\boldsymbol{x}$, respectively. Their values are discussed in Sec. 3.3.3.2. The method of minimizing the effective square distance via the k-d tree pair selection algorithm [23] is maintained. Previous work [81] shows that while the implemented k-d tree algorithm minimizes that distance on average, it is an approximate method that does not ensure minimal distance in $(\tilde{f}, \tilde{c}, \boldsymbol{x})$-space for all particle pairs. Premixed combustion is more sensitive to the unphysical mixing across large distances in composition space compared to non-premixed combustion [75]. To prevent undesired mixing particle pairs obtained by the k-d tree algorithm with $d^{p,q}_{\tilde{c}} > 2c_m$ and $d^{p,q}_{\tilde{f}} > 2f_m$ are omitted from mixing in the doubly conditioned approach. These events account for no more than 3% of all mixing events. The need for two reference variables is illustrated in Fig. 3.2 in which the thermo-chemical state is represented by the CO mass fraction as a function of reaction progress and mixture fraction. The values are extracted from the FGM table. Additionally, four typical stochastic particles A, B, C and D are plotted and the possible selections of mixing partners for particle A

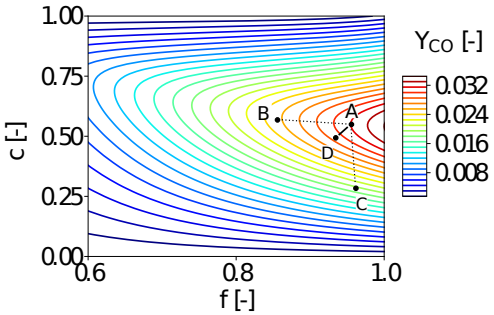

Figure 3.2: Schematic of particle pair selection in MMC for four exemplary stochastic particles. The solid lines indicate iso-contours of the CO mass fraction as a function of progress variable and mixture fraction extracted from the FGM table.

are examined. If the particles are located within the reaction progress variable space only, as described in the singly conditioned approach, particle B would be chosen. However, due to the stratification A and B have very different CO mass fractions and pairing based on c alone clearly does not ensure localness in composition space. Alternatively in the sparse particle approach for non-premixed combustion [12], the distance in progress variable space is ignored, and a small f_m value would locate the particle mixing pairs such that they are close in LES mixture fraction space. Then, particle A would mix with particle C. But these two particles have very different reaction progress (vertical distance) such that non-local pairing is also undesirable. In the doubly conditioned model mixing pairs are localized in both reference spaces and particle A will mix with particle D, because they are close in reaction progress variable and mixture fraction spaces. Note, Fig. 3.2 only demonstrates localization in the reaction progress and mixture fraction spaces. Additionally, particle pairs are chosen to be as close as possible

in physical space, which is not illustrated in Fig. 3.2.

3.3.3.2 MMC localness parameters

The parameters c_m and f_m are - in principle - free model parameters. They may not be universal and depend on the flame regime. In a perfectly stirred reactor regime, where high Karlovitz numbers prevail, conditioning may not be needed as the flame zone will be distributed and a PDF method should work using any reasonable mixing model. For flamelet-like regimes, low values of c_m are likely to be needed. A standard value of $f_m = 0.03$ was established in a number of past MMC computations of non-premixed flames [29, 52, 81], and this value is also applied here. The premixed counterpart is chosen analogously as $c_m = 0.03$ and model sensitivities towards c_m are discussed in Sec. 5.4. The parameter r_m, however, varies with the particle resolution and is formulated to be dependent on c_m and f_m. It is understood that the mixing volume, V_m, is defined as the volume represented by a mixing particle pair within a turbulent flow field. The selection of r_m uses the fact that V_m is equal to the nominal fluid volume represented by each particle. This condition reads

$$CV_m = \Delta_L^3, \tag{3.7}$$

where Δ_L is the average particle distance and $C = 2$ is introduced for the trivial reason that the fluid domain consist of half as many mixing pairs as there are particles. For singly conditioned, non-premixed MMC, Cleary and Klimenko [12] derived a simple expression to relate r_m with f_m. As shown in [71], the parameter r_m can be computed based on a geometrical consideration for two reference variables ξ_1 and ξ_2 and will be discussed in the following. The sliver thicknesses of each generic reference space $l_{\xi_1} = \frac{\xi_{1,m}}{|\nabla \xi_1|}$ and $l_{\xi_2} = \frac{\xi_{2,m}}{|\nabla \xi_2|}$ are introduced, re-

spectively. The length scales are visualized in Fig. 3.3. The localness

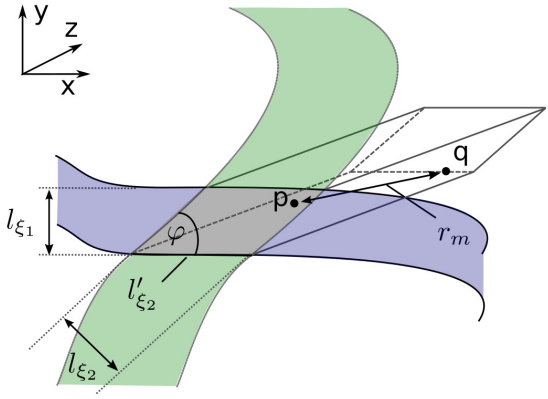

Figure 3.3: Schematic of the sliver representation with two reference variables of a particle mixing pair (p, q). In this example, particle p lies within the front x-y plane while particle q is located within the extrusion along the z direction and confined to be within the 2 scalar slivers of thicknesses l_{ξ_1} and l_{ξ_2}, respectively.

parameters are $\xi_{1,m}$ and $\xi_{2,m}$ and the assumption $l_{\xi_1} < l_{\xi_2}$ (if this is not fulfilled the variables can be commuted) holds. The mixing volume is approached via

$$V_m = l_{\xi_1} l'_{\xi_2} l_x, \tag{3.8}$$

where l'_{ξ_2} (see Fig. 3.3) is given by

$$l'_{\xi_2} = \begin{cases} \frac{l_{\xi_2}}{\sin(\varphi)} & \text{if } \varphi > 0 \text{ and } \frac{l_{\xi_2}}{\sin(\varphi)} < l_x, \\ l_x & \text{if } \varphi = 0 \text{ or } \frac{l_{\xi_2}}{\sin(\varphi)} > l_x \text{ or } |\nabla \xi_2| = 0, \end{cases} \tag{3.9}$$

where φ is the angle between the reference variable gradients. The case analysis is given by the fact that once the sliver thickness based on ξ_2 is bigger than the distance between a particle mixing pair in

physical space with fractal properties, l_x, particle pairs are chosen close in physical space and l_x defines the mixing volume. The length scale l_x is approximated by

$$l_x = \sqrt{A_{\text{surf}}} = \Delta_E^{1-D_f/2} r_m^{D_f/2}, \tag{3.10}$$

where A_{surf} is the sliver surface area modelled in the same manner as in [12] assuming fractal properties. D_f is its fractal dimension and a value of $D_f = 2.36$ was observed experimentally [66]. The filter size is given by Δ_E and defines the fractal inner cutoff scale. The characteristic Lagrangian filter width, r_m, is the outer cutoff scale and the model parameter to be computed. Inserting Eqs. (3.9) and (3.10) in Eq. (3.8) results in distinct formulas for the particle mixing pair volume based on the two cases

First case: $\frac{l_{\xi_2}}{\sin(\varphi)} < l_x$ and $\varphi > 0$

$$V_m = l_{\xi_1} \frac{l_{\xi_2}}{sin(\varphi)} l_x = l_{\xi_1} \frac{l_{\xi_2}}{sin(\varphi)} \Delta_E^{1-D_f/2} r_m^{D_f/2}. \tag{3.11}$$

Second case: $\frac{l_{\xi_2}}{\sin(\varphi)} > l_x$ or $\varphi = 0$ or $|\nabla \xi_2| = 0$

$$V_m = l_{\xi_1} l_x^2 = l_{\xi_1} \Delta_E^{2-D_f} r_m^{D_f}. \tag{3.12}$$

Equating each formula of V_m with the volume represented by the particles (see Eq. (3.7)) and solving for r_m results in the following formulas for the two cases:

First case: $\frac{l_{\xi_2}}{\sin(\varphi)} < l_x$ and $\varphi > 0$

$$r_m = (1/C)^{2/D_f} \left[\frac{|\nabla \xi_1||\nabla \xi_2| \sin(\varphi) \Delta_L^3}{\xi_{1,m} \xi_{2,m} \Delta_E^{1-D_f/2}} \right]^{2/D_f}. \tag{3.13}$$

Second case: $\frac{l_{\xi_2}}{\sin(\varphi)} > l_x$ or $\varphi = 0$ or $|\nabla\xi_2| = 0$

$$r_m = (1/C)^{1/D_f} \left[\frac{|\nabla\xi_1|\Delta_L^3}{\xi_{1,m}\Delta_E^{2-D_f}} \right]^{1/D_f} . \tag{3.14}$$

It is noted here, that particle selection based on 5 dimensions seems overrestrictive in a three-dimensional physical space. Seemingly more consistent, alternative methods for a particle selection algorithm may follow from a coordinate transformation: a three-dimensional space could be spanned by

$$\boldsymbol{e} = (\frac{\nabla\xi_1}{\mid\nabla\xi_1\mid}, \frac{\nabla\xi_2}{\mid\nabla\xi_2\mid}, \frac{\nabla\xi_1}{\mid\nabla\xi_1\mid} \times \frac{\nabla\xi_2}{\mid\nabla\xi_2\mid})^T. \tag{3.15}$$

Then, Eq. (3.6) may be replaced by

$$\left(\hat{d}^{p,q}\right)^2 = \left(\frac{d_{e_1}^{p,q}}{\xi_{1,m}/\mid\nabla\xi_1\mid}\right)^2 + \left(\frac{d_{e_2}^{p,q}}{\xi_{2,m}/\mid\nabla\xi_2\mid}\right)^2 + \left(\frac{d_{e_3}^{p,q}}{r_m}\right)^2 \tag{3.16}$$

with $\boldsymbol{e}$ being the (non-orthogonal) unit vector. If this strategy was pursued, however, the co-ordinate transformation would need to be effectuated at every particle position at every instant in time which is numerically unfeasible. Also, the k-d tree algorithm used in this work splits the samples in the direction where the largest (normalized) differences exist. Imagine now that $\nabla\xi_1$ is aligned with the x-axis. If $\xi_{1,m}/\mid\nabla\xi_1\mid$ is smaller than r_m, the localness condition in x-direction is ignored. The reverse is true for $\xi_{1,m}/\mid\nabla\xi_1\mid > r_m$. The k-d tree algorithm thus ensures that conditioning is executed in any suitable three-dimensional space independent of the number of conditioning variables.

In **single** dimension reference space with $\tilde{c}$ as reference variable the

expression in Eq. (3.14) reads

$$r_m = (1/C)^{1/D_f} \left[\frac{|\nabla \tilde{c}| \Delta_L^3}{c_m \Delta_E^{2-D_f}} \right]^{1/D_f}, \tag{3.17}$$

with an equivalent expression for single conditioning in mixture fraction space. Equation (3.17) includes the reference variable gradient, and r_m should change throughout the computational domain. The numerical implementation of a particle pair selection algorithm with varying r_m is not practical, but a previous DNS analysis demonstrated that a global r_m is sufficient [81]. This is also supported by a number of flame computations where r_m is calculated globally with a characteristic reference variable gradient taken at the position where it is at its maximum. In **doubly** conditioned MMC, for $\tilde{f}$ and $\tilde{c}$ as reference variables Eq. (3.13) can be computed as

$$r_m = (1/C)^{2/D_f} \left[\frac{|\nabla \tilde{c}||\nabla \tilde{f}| \sin(\varphi) \Delta_L^3}{c_m f_m \Delta_E^{1-D_f/2}} \right]^{2/D_f}. \tag{3.18}$$

Again, practical aspects of the particle selection numerics mean that spatial variation of r_m is unsuitable for use in Eq. (3.6) and a global value of r_m is used. The location of determining r_m may be important as the $\tilde{f}$ and $\tilde{c}$ gradients usually vary within the computational domain and the critical locations differ for different setups. The appropriate locations for the investigated application in this work are discussed in Sec. 4.3 and the corresponding r_m values are presented there. The sensitivity of the results towards the r_m variation for doubly conditioned MMC is presented in Sec. 7.3.

3.3.3.3 The mixing time scale models

Once the particle pairs are selected they mix linearly towards their mean with the extent of mixing given by $\gamma = 1 - \exp(-\Delta t/\tau_L)$ (see Eqs.(3.2) and (3.3)). This mixing extent is specified by the characteristic mixing time scale, τ_L. Two different models are introduced that are based on the original formulation derived in [12] and on a modified formulation that was introduced in [81]. The first closure was originally proposed for the mixing time scale in non-premixed combustion and can be formulated for non-premixed ($\xi_1 = f$) and premixed ($\xi_2 = c$) combustion in a generic way [12]

$$\tau_{\text{orig}}^{\xi_i} = C_{\xi_i} \frac{\beta \left(d_{\tilde{\xi}_i}^{p,q} \right)^2}{\tilde{\chi}_{\xi_i}}. \tag{3.19}$$

The modelling of the scalar dissipation rate $\tilde{\chi}_f$ follows the standard procedure for non-premixed combustion

$$\tilde{\chi}_f = 2\mathcal{D}_{\text{eff}} \nabla \widetilde{f} \cdot \nabla \widetilde{f}. \tag{3.20}$$

The model for $\tilde{\chi}_c$ as derived by Dunstan *et al.* [19] has been adapted to the ATF implementation

$$\begin{aligned} \widetilde{\chi}_c =& 2\mathcal{D}F^2 \nabla \widetilde{c} \cdot \nabla \widetilde{c} + [1 - \exp(-0.75\Delta_E/\delta^{Y_{CO_2}})] \\ & \times [1.58\tau(s_L/\delta^{Y_{CO_2}}) + (C_3 - \tau C_4 \, \text{Da}_\Delta) \times (2u'_\Delta/3\Delta_E)]\widetilde{c}(1-\widetilde{c})/2.4, \end{aligned} \tag{3.21}$$

where the model parameters are $\tau = (T_{ad} - T_u)/T_u$, $C_3 = 1.5\sqrt{\text{Ka}_\Delta}/(1 + \sqrt{\text{Ka}_\Delta})$ and $C_4 = 1.1/(1 + \text{Ka}_\Delta)^{0.4}$. $\text{Da}_\Delta = \frac{s_L}{u'_\Delta} \frac{\Delta_E}{\delta^{Y_{CO_2}}}$ and $\text{Ka}_\Delta = (u'_\Delta/s_L)^{3/2}(\Delta_E/\delta^{Y_{CO_2}})^{-1/2}$ are the local Damköhler and Karlovitz numbers, respectively. $\delta^{Y_{CO_2}}$ is the laminar flame thickness introduced in

Sec. 2.3.2. The original expression derived by Dunstan *et al.* [19] is extended by the thickening factor F^2 to compensate for the reduced $\tilde{c}$-gradients due to application of the ATF model for the closure of the $\tilde{c}$-equation. $C_f = 0.1$ and $\beta = 3$ are common modelling constants in Eq.(3.19) for non-premixed combustion. The model sensitivities towards C_c are discussed in Sec. 5.3.

Vo *et al.* [81] re-assessed MMC time scale models and introduced an alternative model (the *anisotropic* - or *a-iso* - model) in non-premixed combustion. The second closure is based on the anisotropic idea and the generic formulation is given by

$$\tau^{\xi_i}_{\text{a-iso}} = C'_{\xi_i} \frac{\left(l_{\xi_i}\right)^2}{2\mathcal{D}^*_{\text{eff}}}, \tag{3.22}$$

where again $\xi_1 = f$ and $\xi_2 = c$ specify non-premixed and premixed combustion, respectively. $\mathcal{D}^*_{\text{eff}} = \mathcal{D}^p + \frac{d_x^{p,q}}{\Delta_E^p}\mathcal{D}_t^p$ is the modified effective diffusivity and l_{ξ_i} is the characteristic length scale of each combustion mode. The length scale in MMC for non-premixed combustion is determined by the distance in physical space of the particle mixing pair $l_f = d_x^{p,q}$ and $C'_f = 0.1$ is fixed. Note the similarity of this model with the standard model for the LES sub-grid time scale. For non-premixed flames, this model yielded much improved predictions of the conditional variances [81]. Note that the use of standard modelling constants is not as intuitive as it seems. The parameters for the mixing time scale relate to the distance between the particles as in previous applications of MMC to non-premixed flames. The parameters for localization in thickened reference space refer, however, to a scale larger than the average particle distance. This is different to conditioning on mixture fraction (or shadow positions) where scales of the reference fields are smaller than the length scale of the particles. As such, conditioning on

$\tilde{c}$ does not - in a strict sense - ensure localness in the composition space of a real (thin) premixed flame but merely ensures the correct flame position and turbulent flame speed on the LES grid. This imposes a higher sensitivity on the right choice of modelling parameters and their interdependencies (i.e. dependence of the correct mixing time scale on c_m), as a "wrong" set of parameters can easily lead to a decorrelation of the particle and the LES solution (cf. Fig. 5.2). Further research is needed to establish a possible correlation between all modelling parameters, but this is beyond the scope of this work and the standard modelling constants provide a stable solution for the analysis of the double conditioning approach.

In turbulent premixed combustion, however, the conventional time scale models tend to fail once the flame front is thinner than the resolved turbulent scales [26]. This is because the scalar dissipation rate is substantially underpredicted in zones where the premixed flame is located [26]. The modelling needs to be based on the correct scales and cannot simply be proportional to the particle distance $d_x^{p,q}$ [85]. In [85] the laminar flame thickness is chosen as the characteristic premixed length scale and here $l_c = \delta^{Y_{CO_2}}$ based on the CO_2 mass fraction (cf. Sec. 2.3.2) is applied. The laminar flame thickness is a function of the local equivalence ratio and is obtained from 1-D laminar freely propagating flame calculations. The modelling constant in Eq. (3.22) for premixed combustion is given by $C_c' = 0.0025$. Differences to the constant chosen in the original publication [85] can be explained by the different definitions of the flame thickness $\delta^{Y_{CO_2}}$. Wang *et al.* [85] use the diffusive thickness ($\delta^u = \mathcal{D}_{\mathrm{th,u}}/s_L$, see Sec. 2.3.2) as compared to the thermal thickness that is used here. The model given in Eq. (3.22) is expected to approximate mixing better in regions away from the premixed flame compared with the model given in Eq. (3.19). Also note that the definition given by Eq. (3.22) is independent of the reference

variables as opposed to the definition given by Eq. (3.19).

Some blending between the time scales for premixed and non-premixed combustion is needed. Away from the premixed flame front, the mixing time scale should revert to the expressions given by Eqs. (3.19) or (3.22) for $\xi_1 = f$. This is particularly important in zones where no reaction occurs, but composition varies due to stratification. There, the mixing frequency should not differ from the mixing frequency observed in turbulent non-premixed combustion. To account for the transition between these two regimes, the harmonic mean weighted by the flame sensor, Ω, (cf. Eq. (2.58)) is used viz.

$$\frac{1}{\tau_L} = \frac{\Omega^p}{\tau^c} + \frac{(1-\Omega^p)}{\tau^f}, \tag{3.23}$$

where τ^c and τ^f represent the respective premixed and non-premixed time scale of either approach. For non-premixed combustion and away from the premixed flame zone, ($\Omega = 0$), the model reverts to $\tau_L = \tau^f$ while for $\Omega \to 1, \tau_L \to \tau^c$. The influence on the results of the choice of the different mixing time scale models (original or anisotropic mixing model) is investigated in Sec. 7.5.

As each stochastic particle within a pair can be associated with a time scale, one further averaging procedure is needed. In previous MMC publications, the maximum mixing time scale ($\tau_L^{p,q} = \max(\tau_\mathrm{L}^\mathrm{p}, \tau_\mathrm{L}^\mathrm{q})$) had been selected to avoid excessive numerical diffusion. If not stated otherwise, the same approach is applied in this work. In Sec. 7.5 the sensitivities of the results on either the maximum value or the harmonic mean are investigated.

3.4 Summary

This chapter introduces the multiple mapping conditioning mixing model for turbulent combustion. An overview of different MMC mixing models is given and the reference variables as the common fundamental tool of all MMC versions is emphasized. The reference variable in generalized MMC for non-premixed combustion is stated as the filtered mixture fraction. For premixed combustion with stratification the choice of the reference space is not that obvious. In this thesis the reference variables are chosen as the progress variable and the mixture fraction of the ATF approach in LES. For the singly conditioned MMC approach (reaction progress variable as reference variable) and the doubly conditioned MMC approach (additionally the filtered mixture fraction is taken as reference variable) the MMC parameters and the mixing time scale model are revised. The computation of the mean physical distance of a particle mixing pair for two reference variables is presented and two different mixing time scale models are introduced. For the application of this MMC mixing model the following chapter presents the validation cases of the current work. The flame configuration and numerical setup of the turbulent stratified flame series are introduced.

Chapter 4

Flame configurations

Section 4.1 introduces the experimental setup of the turbulent stratified flame (TSF) series and the specific configurations which serve as validation cases in this work. Details of the the numerical setup are stated in Sec. 4.2. The computation of the MMC model parameter r_m at different locations within the stratified flame is presented in Sec. 4.3.

4.1 Experimental setup

The setup of the burner used in the TSF series consists of three staged concentric tubes placed in coflowing air which allows for the generation of both shear and stratification in the flow as illustrated in Fig. 4.1. In this work different configurations are investigated numerically which differ in their composition (stratification) and/or bulk velocities (shear) of the inner and outer slots. All flame configurations are stabilized by the central pilot. The fuel is methane and the equivalence ratio is always identical between the central pilot and slot 1. The inner tube radii are 7.4 mm, 18.5 mm and 30 mm, respectively. The different operating

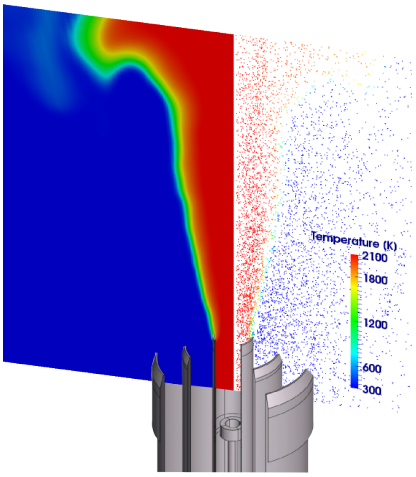

Figure 4.1: Illustration of the burner geometry with the ATF-FGM solution (left) and the particle distribution in the computational domain (right) coloured by temperature in TSF-A.

conditions investigated in this work are summarized in Tab. 4.1. The

Table 4.1: Overview of different operating conditions of the TSF series investigated in this work. u_i are the bulk velocities at the corresponding outlets.

	TSF-A (reference configuration)	TSF-C	TSF-G
ϕ_{Pilot} [-]	0.9	0.9	0.9
u_{Pilot} [m/s]	7.7	7.7	7.7
ϕ_{Slot1} [-]	0.9	0.9	0.9
u_{Slot1} [m/s]	10.0	10.0	10.0
ϕ_{Slot2} [-]	0.6	0.6	0.9
u_{Slot2} [m/s]	10.0	5.0	10.0

pilot velocity is given by the mass flow rate of the cold reactants and

equilibrium assumptions of the burnt products as used in the computations. The stratified flame TSF-A holds different equivalence ratios in slots 1 and 2, while the flame TSF-C is identical in composition, but features different bulk velocities within these slots to include shear. The flame TSF-G is a fully premixed flame without stratification, i.e. the fluids within the two slots have the same equivalence ratio and the same bulk velocities. TSF-A is stated as the reference configuration in this work. The estimated ranges of the TSF series for the Karlovitz ($1.2 \leqslant \mathrm{Ka} \leqslant 2.1$) and Damköhler numbers ($50 \leqslant \mathrm{Da} \leqslant 80$) [67] place the three configurations within the thin reaction zone regime where some thickening of the preheat zone of the flame can be expected. The investigated flames therefore present appropriate applications for the evaluation of MMC's capability to predict (1) a flamelet-like solution -if this limit is enforced- and (2) possible deviations from this laminar flame structure. Advanced discussions on this flame series can be found in the literature [62, 67].

The multi-scalar line measurements of temperature (Rayleigh scattering) and major species concentrations (Raman scattering for N_2, O_2, CH_4, H_2O, CO, CO_2, H_2 and two photon CO-LIF) presented in this work were performed at the Turbulent Combustion Laboratory at Sandia. Due to differences in instrumentation, they deviate in some respects from previously published data of the same flames [62, 43] that were taken in Darmstadt. The updated experimental data is given in this work and a discussion on the improved measurement setup can be found in [72].

4.2 Numerical configuration

The computation of the LES-filtered reaction progress variable was realized by an OpenFOAM solver called mmcFoam [25, 61]. The FGM

chemistry model and the ATF-modified transport equations of the filtered reaction progress variable and mixture fraction have been implemented to account for stratified combustion. The results of Chapters 5 and 6 are based on the mmcFoam-2.4.x version, while the results of Chapter 7 are based on the mmcFoam-5.x version. Consistency of the two versions was ensured. The computational domain is resolved by approximately 0.7 million cells and extends 316 mm in axial (the position $z = 0$ mm defines the pilot exit plane) and 300 mm in radial directions. This leads to a cell size of $\Delta_E \approx 1.6$ mm in the flame front at $z = 75$ mm. This is the approximate location where the flame front meets the mixing layer in the stratified cases. The quality of the resolution was validated by comparison with LES-ATF-FGM results by Kuenne *et al.* [43]. Standard LES closures such as the Smagorinsky model [64] and constant Schmidt number assumptions (with $\mathrm{Sc} = 0.7$ and $\mathrm{Sc}_t = 0.4$) are used.

The turbulent inflow data is generated via independent pipe flow simulations (slots 1 and 2) and by synthetic turbulence for the pilot stream as described in [35]. Zero-gradient pressure boundary conditions are applied at the inlets and fixed pressure at the domain sides and outlets. Numerical discretisation of the filtered transport equations in the LES framework is realized via a second order backward scheme in time. For the filtered momentum equation a central difference scheme is used for the divergence term, while all the other transport equation terms are discretized by a total variation diminishing scheme. The maximum thickening factor is computed dynamically within the computational domain as introduced in Eq. (2.60) with $\Delta_{E,\max} = 0.15$ mm. The parameters in the efficiency model introduced in Sec. 2.4.6 are kept the same as originally proposed. In the current implementation the evaluation of the sub-grid velocity fluctuations in Eq. (2.62) is slightly altered compared with the originally proposed implementation [13, 10] where

the Laplace operator is evaluated on a $4\Delta_E$ stencil. Here, the operator is evaluated on a twice coarser mesh and interpolated to the fine mesh instead.

For the Lagrangian scheme there is on average one stochastic particle per three LES cells as this number of particles corresponds to a sparse Lagrangian distribution. This results in approximately $300,000$ particles within the computational domain. The source terms for the composition scalar field and temperature of the particles (see Eq. (2.73)) are computed based on the GRI-Mech 3.0 kinetic scheme [65], which is the same as for the generation of the ATF-FGM table. Species and reactions associated with NO_x formation are not considered on the particles for the benefit of reduced computational cost. Firstly, approximately 23 flow through times (based on the bulk velocity of slot 1) are computed with the ATF-FGM approach to reach a statistically steady-state solution. Then, the particles are introduced throughout the domain and their particle composition is initialized as the local (interpolated) filtered reaction progress, mixture fraction and the corresponding thermo-chemical state from the FGM table. The statistics for the analysis are collected for 1.3 flow through times (based on the bulk velocity of slot 1). The computational requirements exemplary for the simulation results presented in Chapter 6 amount to $2,400$ CPUh per flow through time on 24 cores of an Intel Xeon E5-2680 with roughly 75% of the cost being associated with the particle solution.

4.3 Computation of r_m

Three characteristic locations for the computation of r_m are selected as illustrated in Fig. 4.2 for TSF-A. (1) "Pos-c" is at an upstream location within the flame front between the pilot and unreacted mixture. Here, no stratification exists and MMC (including the computation of

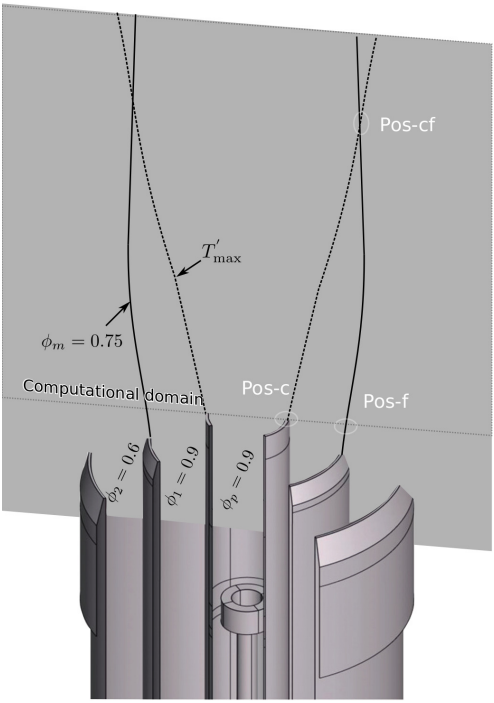

Figure 4.2: Schematic of the turbulent stratified flame (TSF-A) burner setup with pilot, slot 1 and slot 2. The mean radial positions of the center of the flame brush that is taken as the position of the maximum temperature RMS, $T'_{\max}$, is indicated by dashed lines, and the mean location of the stratification layer given by the equivalence ratio, $\phi_m = \frac{\phi_1+\phi_2}{2}$, is represented by the solid lines.

r_m) should revert to single conditioning with $\tilde{c}$ as reference field (cf. Eq. (3.14) with $\xi_1 = \tilde{c}$ for computation of r_m). (2) "Pos-f" is located at the upstream location within the stratification layer where mixture fraction gradients are highest and MMC should revert to single conditioning with mixture fraction as a reference variable (cf. Eq. (3.14)

with $\xi_1 = \tilde{f}$). (3) "Pos-cf" is given by the position where the mean flame brush meets the mean mixing layer. Here, the use of two reference fields is expected to be the most crucial and Eq. (3.18) should be used.

At "Pos-cf" the temporal mean of $\nabla\tilde{c}$, $\nabla\tilde{f}$ and φ is taken at the axial position $z \approx 83\,\text{mm}$ (this is where the mean flame brush meets the mean mixing layer investigated in Chapter 7) and radial position of $\max(|\nabla\tilde{c}||\nabla\tilde{f}|)$. For the other two locations $\nabla\xi_i$ is evaluated as the maximum normal gradient. For "Pos-c", r_m is increased to $r_m = 5.9\,\text{mm}$ instead of $r_m = 3.47\,\text{mm}$ obtained by Eq. (3.14), because the former value is applied in [72] [1] and the smaller values lead to too many odd mixing particles with $d_{\tilde{f}} > 2f_m$ and $d_{\tilde{c}} > 2c_m$, which influenced the flame propagation speed. The value for r_m at "Pos-f" is rather small ($r_m = 2.5\,\text{mm}$) compared to the values computed at the other locations. This is due to the relatively small mixture fraction gradient and a larger Δ_E in this region (cf. Eq. (3.14)). Using this value throughout the entire domain would enforce strong localization in physical space and prevent localization in reaction progress variable space where needed. The values at the other two characteristic locations provide more reasonable values with $r_m = 5.9\,\text{mm}$ ("Pos-c") and $r_m = 8.7\,\text{mm}$ ("Pos-cf") which is of the order of the inner pilot diameter and about 1 order of magnitude larger than the laminar flame thickness. The larger value for "Pos-cf" is expected as closeness in a two-dimensional reference space can only be achieved by relaxing closeness in physical space if the total number of particles (i.e. Δ_L) is kept constant. The different r_m values at different locations are summarized in Tab. 4.2. Generally, the computation of r_m is restricted to a specific grid, because $\nabla\tilde{c}$, $\nabla\tilde{f}$ and Δ_E are used in the formulas. Modifying r_m

[1] Note the difference in Eq. (3.14) to former publications [12, 72] as previously the constant C was not meant to represent any actual relation.

Table 4.2: Overview of different r_m values at different locations within the stratified flame.

Position name given in Fig. 4.2	Formula	r_m [mm]
Pos-cf	Eq. (3.18)	8.7
Pos-c	Eq. (3.14) with $\xi_1 = \tilde{c}$	5.9
Pos-f	Eq. (3.14) with $\xi_1 = \tilde{f}$	2.5

values merely modifies the weighting between the localization parameters for localization in the composition and physical spaces, but does not introduce errors in the model. The influence of r_m variations on the simulation results is analyzed in Sec. 7.3.

Chapter 5

Singly conditioned MMC-ATF simulations of reference configuration

In this chapter the sparse Lagrangian MMC mixing model coupled with ATF in the LES framework is applied to the reference configuration which has been introduced in the previous chapter. In the MMC-ATF approach the mixing operator is conditioned on the LES-filtered reaction progress variable (singly conditioned MMC) and the mixing time scale is modelled based on the original description as described in Eq. (3.19) with $\xi = c$.

Section 5.1 provides a general discussion on the MMC-ATF model parameters for turbulent premixed combustion. Section 5.2 presents

results of the base case using "standard" modelling parameter values, i.e. the values are not modified compared to their counter parts in non-premixed combustion. The model sensitivities towards the modelling parameters C_c and c_m are discussed in Sec. 5.3 and Sec. 5.4, respectively.

5.1 MMC modelling parameters

The MMC modelling parameters are c_m and r_m (introduced in Eq. (3.6)), which control the localness of mixing in composition and physical space, respectively, and the parameter C_c that constitutes a modelling constant for the mixing time scale (cf. Eq. (3.19)). Standard values are $f_m = 0.03$ and $C_f = 0.1$ that yield good MMC predictions for non-premixed flames. The same values are used here for the premixed case, i.e. $c_m = 0.03$ and $C_c = 0.1$. The parameter r_m is not independent of c_m, and Eq. (3.17) then gives a value of $r_m = 5.9\,\text{mm}$ [1] for the particle seeding used here. Results from a base case using these modelling parameters are presented first, while the model sensitivities towards C_c and towards c_m are discussed in Sec. 5.3 and Sec. 5.4, respectively.

5.2 Base case

Figure 5.1 displays the Favre mean temperature (left) and its root-mean-square (RMS) (right) versus radial positions at four axial positions. For the results from the ATF-FGM simulation the temperature is extracted from the FGM table during run time and then time-averaged, i.e. only the resolved part is considered. The mean temperature and

[1] Due to rounding error this value is slightly changed compared to $r_m = 5.8\,\text{mm}$ in [72].

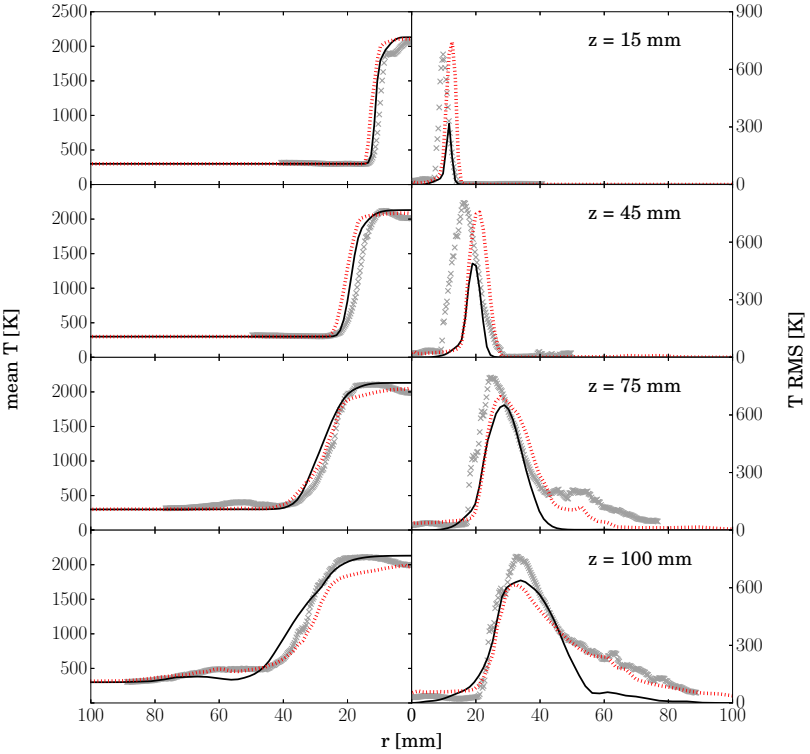

Figure 5.1: Radial profiles of Favre mean temperature and RMS at different axial positions. Grey crosses represent experimental data. Black solid lines represent the ATF-FGM solution and dotted red lines represent the Lagrangian solution for $c_m = 0.03$ and $C_c = 0.1$.

RMS are in good agreement with the experimental data and comparable to results presented in Fiorina *et al.* [22] where different model predictions of TSF-A were compared. The reasons for the slight overprediction of temperature on the centerline at z>15 mm can be associated with heat losses of the pilot flame to the burner walls upstream of

the nozzle exit ($z < 0\,\text{mm}$). The inclusion of the heat losses is not attempted here as it would require an additional dimension in the flamelet table. The omission of heat losses also leads to a wider profile of the ATF-FGM solution at $z = 15\,\text{mm}$ and $z = 45\,\text{mm}$ in comparison with the experimental data due to the smaller radial expansion of the flow at lower temperatures. However, the primary objective of the present investigation is the analysis of the flame structure and the capability of MMC to capture the different flame regimes. The current solution provides a satisfactory prediction of the flame position and thus of the reference scalar used for the conditioning of the MMC mixing model. No further optimization of the ATF-FGM solution (e.g. inclusion of enthalpy as a third FGM parameter) is attempted nor needed here.

As expected, the position of the flame predicted by the particle solution (dotted lines) largely follows the ATF-FGM solution as the flame propagation is imposed by the ATF-FGM approach. The peak value of the ATF-FGM temperature RMS is underpredicted upstream but matches the experimental data fairly well further downstream. The underprediction close to the nozzle can be expected due to the artificial thickening of the flame which significantly reduces the flame wrinkling of the resolved reaction progress variable and thus suppresses the fluctuations of all dependent quantities (such as temperature). Most notably, however, this is different for the Lagrangian particles: They represent an instantaneous and local solution of the composition space and the correct (measured) RMS is indeed much more accurately captured by the MMC model.

As indicated above the thermo-chemical state on the particles (i.e. the solution of Eq. (2.73)) needs to correlate with the LES-filtered reaction progress to ensure an appropriate conditioning of the particles to be mixed. The correlation is shown in Fig. 5.2 where the normalized CO_2 mass fraction from the MMC particles, θ^p, is plotted versus the

thickened progress variable (the reference variable) for stochastic particles at $z = 15\,\text{mm}$. It is apparent that the particles ignite and burn

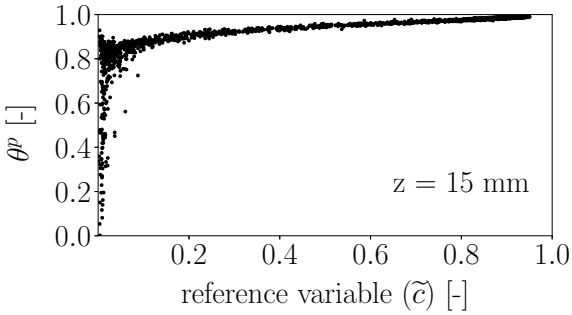

Figure 5.2: Scatter plot of normalized CO_2 mass fraction versus reference variable at $z = 15\,\text{mm}$ for the MMC simulation with $c_m = 0.03$ and $C_c = 0.1$.

in regions of low $\widetilde{c}$ values. This indicates that (1) the flame modelled by the particles sticks to the fresh gas side of the (thickened) premixed flame predicted by ATF-FGM and (2) the flame front as predicted by the particles tends to be thinner compared to the flame thickness predicted by the ATF-FGM approach since θ^p increases within a narrow band of $\widetilde{c}$. While the latter is an indication for a physically correct prediction of the flame structure by the particles, the former indicates too much mixing that heats up unreacted particles too quickly and results in an overprediction of the flame speed compared with the ATF-FGM solution. This is consistent with Fig. 5.1 where the flame predicted by MMC appears to be slightly shifted towards larger radii at the two upstream locations and is located at positions where LES-ATF-FGM predicts low (non-zero) values of $\widetilde{c}$. In other words, the turbulent diffusion of the particles does not match the turbulent flame speed of the underlying reference field and the standard modelling constants

calibrated for non-premixed combustion need to be adapted. This is discussed in the following section.

5.3 Sensitivity to C_c parameter

5.3.1 Flame position and correlation of reference variables and corresponding stochastic properties

The intensity of mixing is primarily controlled by the mixing time scale τ_L. DNS studies for non-premixed combustion [81] suggested that the standard model (cf. Eq. (3.19)) tends to underestimate the appropriate mixing time and thus the conditional fluctuations of the reactive scalars [80, 81]. In the absence of suitable DNS data, the development of a new time scale model is not intended but the mixing frequency is reduced. This is performed by varying the time scale constant C_c and the sensitivity of the MMC predictions towards the modelling parameter C_c is investigated. The time scale constant is increased from the standard value of $C_c = 0.1$ to $C_c = 0.5$ and $C_c = 1.0$. Figure 5.3 shows the the radial profiles of the Favre mean temperature and RMS at different axial positions for the experimental data and the Lagrangian solutions with varying C_c value. The flame expansion depends on the C_c value. For $C_c = 1.0$ the flame is shifted towards smaller radial locations for all axial locations, while for smaller C_c values (increased mixing) the flame is shifted towards higher radial locations. The temperature RMS does not correlate in such a linear way. At the upstream location the predictions obtained with $C_c = 0.1$ present the highest peak temperature RMS and even slightly overpredicts the experimental data. The results for $C_c = 0.5$ and $C_c = 1.0$ show decreased peak temperature RMS and are similar to each other. The location of the peak temperature RMS is

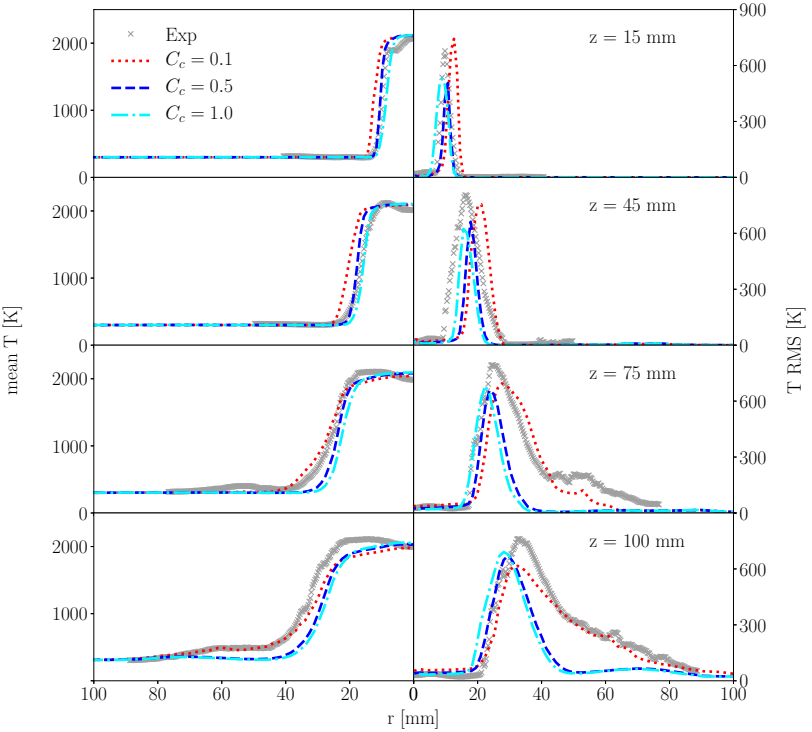

Figure 5.3: Radial profiles of the Favre mean temperature and RMS at different axial positions. Grey crosses represent experimental data. The Lagrangian solutions are represented by the dotted red lines ($C_c = 0.1$), the dashed blue lines ($C_c = 0.5$) and the dash-dotted cyan lines ($C_c = 1.0$) with $c_m = 0.03$ for all cases.

shifted in alignment to the flame position. The influence of the C_c variation on the correlation between the reaction progress on the stochastic particle and the reference variable is shown in Fig. 5.4. Clear sensitivities can be observed. For $C_c = 0.1$ the flame thickness represented by the particles is very small as the flame sticks to the lower bound-

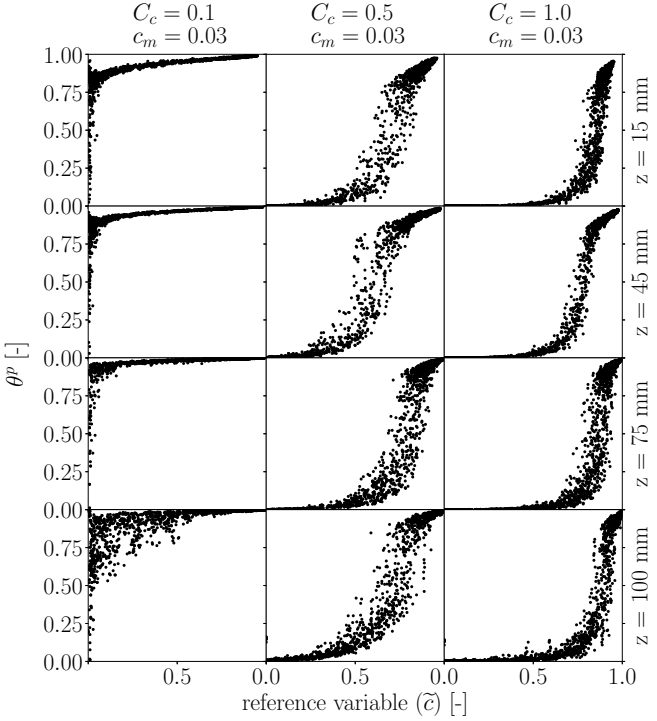

Figure 5.4: Scatter plot of normalized CO_2 mass fraction versus reference variable at different axial positions for MMC simulations. Left: $C_c = 0.1$; middle: $C_c = 0.5$ and right: $C_c = 1.0$ with $c_m = 0.03$ for all three cases.

ary of the thickened progress variable. No clear correlation between θ^p and $\widetilde{c}(x^p)$ exists due to the mismatch in turbulent flame propagation of the ATF-FGM and MMC solutions. An increase of the mixing time scale shows a clear improvement and a shift of the particle ignition towards higher values in reference space and away from the leading edge of the ATF-FGM flame. This corresponds to a more narrow flame (a

shift of the mean flame position towards smaller radii) at all locations, which is consistent with the results presented in Fig. 5.3. The results for $C_c = 0.5$ and $C_c = 1.0$ show a similar correlation between θ^p and $\widetilde{c}(x^p)$ at all axial positions. For $C_c = 0.1$ MMC resembles the model by Zoller *et al.* [89] where a reference field (the flame surface density) is used as an "ignition" indicator and the reference field is bi-modal. The mapping of θ^p and $\widetilde{c}(x^p)$ for larger C_c allows to capture a more gradual mixing across the flame front as particles from the preheat zone and the reaction zone should feature different $\widetilde{c}$-value and will not directly mix. For now, any apparent mapping is sufficient and the flame thickness is discussed. The MMC solution shall represent the real (thin) flame and Fig. 5.4 indicates a significantly thinner flame predicted by MMC (compared with ATF-FGM). As example may serve data from the axial position $z = 15\,\text{mm}$. The normalized CO_2 mass fraction on the particles, θ^p, increases from 0.1 to 0.9 in a range of $\Delta\widetilde{c} \approx 0.1$ for $C_c = 1$ and $\Delta\widetilde{c} \approx 0.2$ for $C_c = 0.5$, i.e. the flame represented by the particles will not be distributed across the entire extent of the thickened premixed flame and maximum temperature gradients will be at slightly different spatial locations. Small differences between the results for $C_c = 1.0$ and $C_c = 0.5$ can be observed, but an appropriate choice of the mixing time scale suffices to adapt the turbulent flame propagation speed of the particles to the flame propagation of the ATF-FGM solution and that reaction progress of the particle and ATF-FGM solutions remains sufficiently correlated throughout the computational domain.

5.3.2 Flame thickness

As indicated above, Fig. 5.4 suggests a lower spatial extent of the flame simulated by the particles than the one predicted by ATF-FGM. The scatter plot shows all particles sampled at one axial position (as given

by the black dots) and does not allow for a direct estimate of the flame thickness predicted by MMC as the width in $\widetilde{c}$-space represents the thickness of the flame brush rather than the thickness of a specific flame element. To estimate this thickness the particle positions and temperature evolution of single particles are tracked. Some of these particles are exemplarily shown in Fig. 5.5 for $C_c = 0.5$ and $C_c = 1.0$ at $z = 15\,\mathrm{mm}$. Each particle is represented by a different colour. Then,

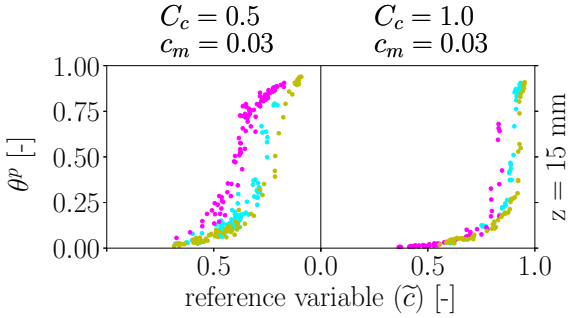

Figure 5.5: Single particles tracked through the flame front showing their normalized CO_2 mass fraction versus reference variable at $z = 15\,\mathrm{mm}$ of MMC simulations for $C_c = 0.5$ (left) and $C_c = 1.0$ (right). The different colours represent different particles.

the flame thickness can be approximated via

$$\delta_{\mathrm{MMC}} \approx \frac{\langle \Delta \widetilde{c}^{\,p} \rangle}{|\nabla \widetilde{c}|_{\max}}, \tag{5.1}$$

where $|\nabla \widetilde{c}|_{\max}$ is the magnitude of the thickened progress variable's gradient at the $\widetilde{c}$-value where $d\theta^p/d\widetilde{c}$ is largest. This $\widetilde{c}$-value changes with C_c and with axial position but equals $\widetilde{c} \approx 0.82$ for $z = 15\,\mathrm{mm}$ and $C_c = 1.0$ (cf. Fig. 5.5). In Eq. (5.1) the term $\langle \Delta \widetilde{c}^{\,p} \rangle$ represents the mean

of particle differences in reference space and each $\Delta\widetilde{c}^p$ is computed via

$$\Delta\widetilde{c}^p = \widetilde{c}|_{T_p=1800K} - \widetilde{c}|_{T_p=500K}\,, \tag{5.2}$$

where T_p specifies the particle temperature and the temperature limits are chosen to approximately represent the area of highest reaction progress gradient within the reaction zone. Sampling 20 particles gives an average flame thickness of $\delta_{\mathrm{MMC}} \approx 1.4\,\mathrm{mm}$. More importantly, however, are individual particles that allow for estimates of the flame thickness between $\delta^{\mathrm{min}}_{\mathrm{MMC}} = 0.7\,\mathrm{mm}$ and $\delta^{\mathrm{max}}_{\mathrm{MMC}} = 2.0\,\mathrm{mm}$. If this is compared to $\delta^{Y_{\mathrm{CO_2}}} \approx 0.6\,\mathrm{mm}$ which corresponds to the laminar flame thickness based on the CO_2 mass fraction introduced in Eq. (2.44), one can conclude that some particles can capture the laminar flame thickness while others show some flame thickening potentially due to the effect of turbulence on the preheat zone (see the particle coloured 'magenta' in Fig. 5.5 with $C_c = 0.5$). These numbers should be understood as estimates for the flame thickness, but they certainly approximate the actual (physical) flame thickness more accurately when compared to the rather broad flame thickness of $\delta_{\mathrm{ATF}} \approx 3.5\,\mathrm{mm}$ at $z = 15\,\mathrm{mm}$ predicted by ATF-FGM. The latter serves here as a limiting value for the comparison and should not be confused with the actual flame thickness as ATF (by definition) does not attempt to preserve a thin flame.

5.3.3 Flame structure

The analysis of the flame thickness demonstrates that MMC can predict thin laminar-like flames, but it remains to be shown whether a thickening of the flame can be associated with deviations from the flamelet structure and whether the extent of these deviations can be backed by comparison with experimental data. Figure 5.6 compares the computed

CH_4 mass fraction with measurements. The results are presented for

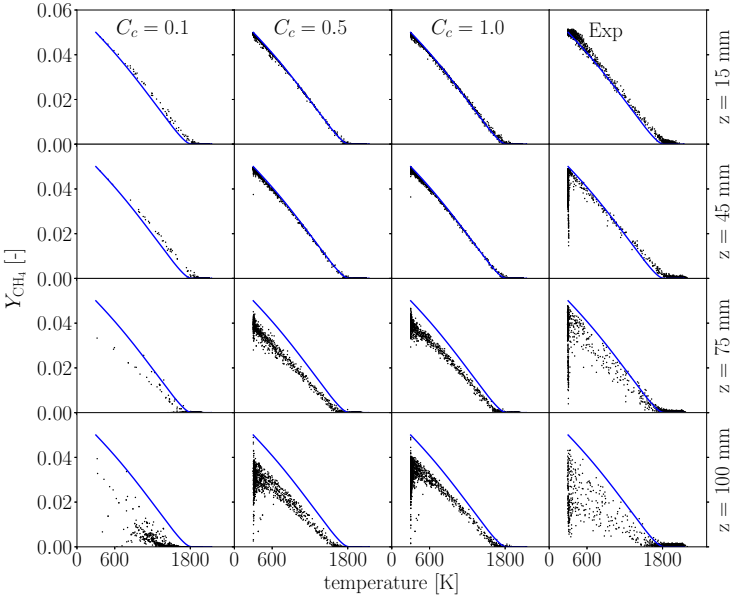

Figure 5.6: Scatter plot of CH_4 mass fraction versus temperature at different axial positions. MMC simulations with $c_m = 0.03$ are given for $C_c = 0.1$ (first column), $C_c = 0.5$ (second column) and $C_c = 1.0$ (third column). Fourth column: experimental data. Solid lines: FGM solution for $\phi = 0.9$.

different C_c values as functions of temperature. Note that samples are only collected from within the flame brush when conditional quantities are shown. This is realized in the experiments by limiting the radial extent of the measurement locations. For MMC the sampling was equally constrained by the same radial locations. In addition to the particle data, the solid line depicts the FGM solution for $\phi = 0.9$, which is plotted here for orientation at all axial positions. Good agreement be-

tween the MMC results and the experimental data can be seen. At the upstream locations ($z = 15\,\text{mm}$ and $z = 45\,\text{mm}$) the CH_4 mass fraction depends linearly on the temperature for the burning fluid as is expected for a fully burning premixed flame. Here, the flame structure seems to be well approximated by a flamelet and this can be captured by MMC. Very good agreement with the experiments exists for all C_c-values. Further downstream ($z = 75\,\text{mm}$), the results are compared with the flamelet with $\phi = 0.9$ for illustration only as much larger deviation can be expected and indeed occur. This is due to the mixing of the reactants of the first ring with reactants of the second ring and (even further downstream) with air. The MMC results for $C_c = 0.5$ and $C_c = 1.0$ tend to agree quite well with the experimental data. At $z = 100\,\text{mm}$ it is apparent that a mixing time scale using $C_c = 0.1$ mixes too quickly as any high methane mass fractions disappear indicating rather low equivalence ratios across the flame for this MMC solution. Larger mixing times scales ($C_c = 0.5$ and $C_c = 1.0$) yield a much improved agreement with experiments but scatter for the intermediate temperatures tends to be somewhat too low. This is due to the predicted flame shape (cf. Fig. 5.4) which is rather narrow, and the burning MMC particles tend to originate from the inner streams with higher equivalence ratios and thus overpredict methane mass fractions when compared with the experimental data.

The analysis of an intermediate species such as carbon monoxide allows for a more detailed assessment of the predicted inner flame structure. Figure 5.7 shows a comparison of Y_{CO} conditioned on temperature from experiments and MMC for different axial positions and different C_c values. The results are coloured by the equivalence ratio $\phi \in [0.6, 0.9]$, where the minimum and maximum values of this range are selected as they represent the equivalence ratios of rings 1 and 2, respectively. Additionally, the coloured solid lines depict the flamelet

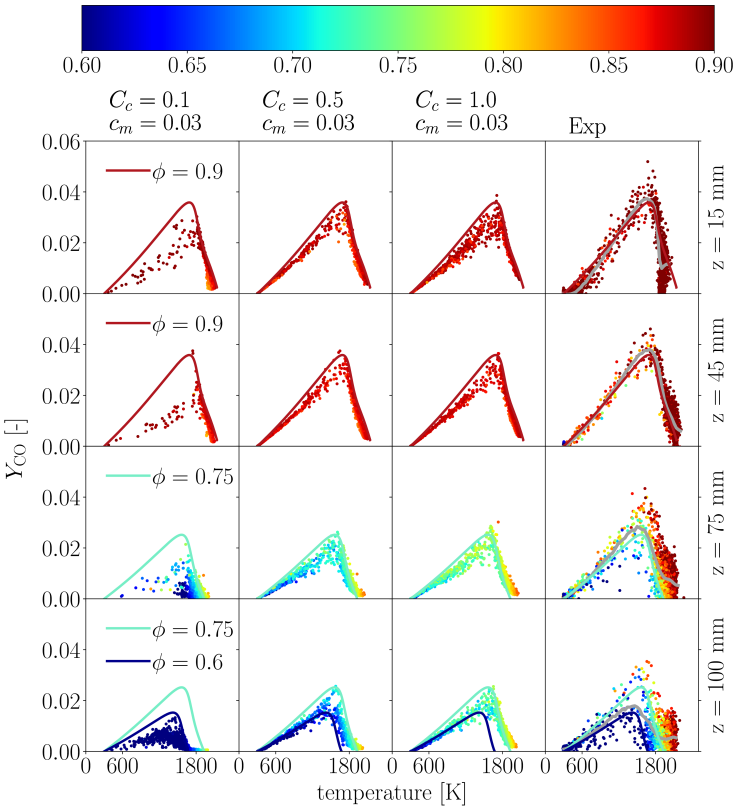

Figure 5.7: Scatterplot of the mass fraction of CO versus temperature coloured by equivalence ratio ϕ at different axial positions for $C_c = 0.1$ (left), $C_c = 0.5$ (middle) and $C_c = 1.0$ (right). The coloured solid lines are given by the FGM table for different equivalence ratios, namely $\phi = 0.6$, $\phi = 0.75$ and $\phi = 0.9$. The additional grey line indicates the conditional mean of the measurements.

solutions of the FGM table for equivalence ratios $\phi = 0.6$, $\phi = 0.75$ and $\phi = 0.9$. Note that the computation of ϕ from the experiments may

be subject to small errors ($\Delta\phi < 0.02$) as not all species are measured and an approximation for ϕ needs to be employed [67]. Also, and for orientation only, the grey line indicates the conditional mean of the measurements.

Two issues can be observed: firstly, predicted CO mass fractions tend to be lower than measurements. Most notably, $C_c = 0.1$ leads to rather low CO values which can be attributed to the fast mixing and the increased reaction progress as also observed in Fig. 5.4. The measured RMS tends to be rather large but the conditional mean (grey line) stays close to the flamelet solution for $\phi = 0.9$ at $z = 15$mm. The MMC results approximate the flamelet solution rather well and predictions somewhat lower than the flamelet solution can be caused by turbulence (i.e. the appropriate amount of mixing) as increased strain should tend to reduce predicted CO [34]. Secondly, the scatter and deviations from the flamelet solution can be associated with different sources: (1) scatter can be caused by turbulence and (2) mixing of fluid elements with different equivalence ratios broaden the CO profiles as indicated by the colors in particular for downstream positions with $z \geqslant 75\,\text{mm}$. It is apparent that MMC largely preserves the flamelet-structure for a given equivalence ratio and that the amount of scatter (conditioned on a specific ϕ) is comparable to the scatter observed in the experiments.

Overall, MMC seems to predict mixing between fluids of the rings and the co-flow faster than the experiments would suggest leading to a faster depletion of mixtures with the highest equivalence ratio and therefore to a reduced spread in stratification levels. But again, differences at $z = 100\,\text{mm}$ can be associated with differences in the predicted and measured flame width (cf. discussion surrounding the scatter observed in Fig. 5.6), but one may also interpret the scatter as the tendency for a thickening of the predicted flame in the preheat zone, while

the mass fractions in hotter regions tend to stick rigidly to the flamelet solutions.

A quantitative analysis of the deviations from the flamelet structure can be conducted by analyzing the conditional mean and, in particular, the conditional RMS of carbon monoxide. These deviations stem from turbulent contributions to (i) the drift term and the Wiener process for particle displacement (i.e. the turbulent contribution to $\mathcal{D}_{\text{eff}}$ in Eq. (2.72)) and (ii) the modelling of the mixing operator in Eq. (2.73) using a turbulent mixing time scale τ_L. Some of these turbulent contributions are implicitly modelled by the flamelet method, while in MMC-LES these distributions are solved through the PDF transport equation. Of primary importance is the different treatment of the temporal evolution of the composition space: The flamelet table provides steady state solutions for specific values of the scalar dissipation, while stochastic particle compositions in MMC-LES evolve in time along the Lagrangian trajectories of those particles. This different treatment in MMC preserves the relative importance of the turbulent and chemical time scales of all chemical species (and not of just those species which are closely correlated with either the $\tilde{c}$ or $\tilde{f}$ fields). Lastly, the standard implementation of the flamelet tabulation method omits cross-correlations in reaction progress-mixture fraction space while MMC particles mix across both spaces. Thus, a much wider composition space is accessed by the MMC solution and differences between ATF-FGM and MMC solutions and subsequent comparison with experimental data provide insight on MMC's capabilities to predict the accurate level of turbulence-chemistry interactions. Figure 5.8 shows the conditional mean mass fraction of CO and its RMS versus temperature for different axial positions predicted by MMC and obtained from experiments. In MMC the parameters are chosen as $c_m = 0.03$ and $C_c = 0.5$, as this choice yielded accurate predictions previously. The error bars in-

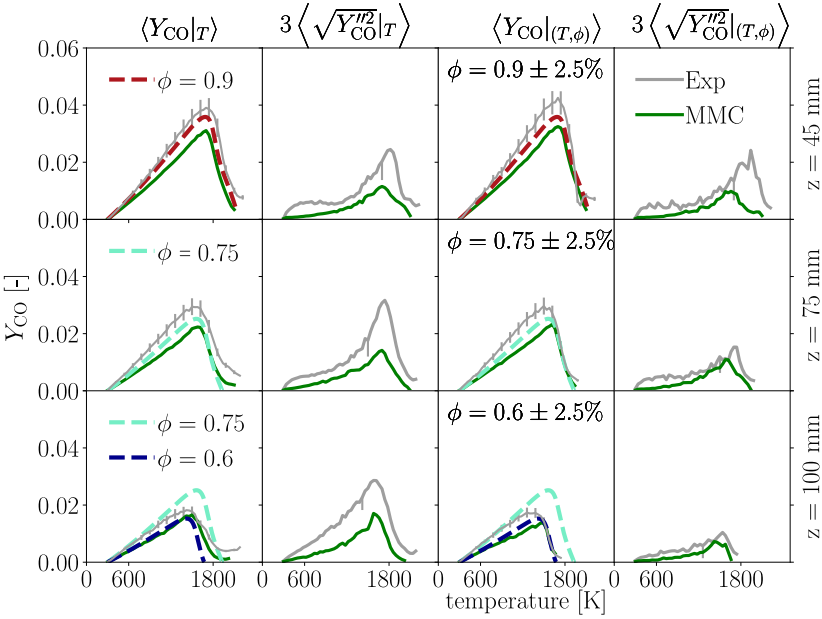

Figure 5.8: Mass fraction of CO versus temperature at different axial positions for experimental data (grey lines) and MMC ($c_m = 0.03$ and $C_c = 0.5$) results (green solid line). Left column: conditional mean; center left column: conditional RMS; center right column: conditional mean for specific equivalence ratios and right column: conditional RMS for specific equivalence ratios. The coloured dashed lines within the first and third column are given by the FGM table for different equivalence ratios, namely $\phi = 0.6$, $\phi = 0.75$ and $\phi = 0.9$.

dicate the estimated calibration uncertainty of 10% for the conditional means. Measurement uncertainty due to photon statistics is 4.5% in a premixed calibration flame with Y_{CO} roughly 0.06. The one-sided error bars associated with the RMS measurements visualize the expected contribution of this random uncertainty to the RMS level corresponding to the maximum conditional mean CO. Relative uncertainty will be

higher for lower CO levels. For temperatures away from the peak CO, uncertainty in temperature also contributes to the conditional RMS in CO. Furthermore, there are additional sources of random uncertainty in turbulent flames, which are difficult to quantify, including fluctuations in luminous background that are not necessarily correlated with the local CO level. It is seen that MMC predictions for the conditional means (first column) lie somewhat below the given uncertainties and are of satisfactory accuracy. Calculating a (conventional) conditional RMS across all equivalence ratios (shown in the second column of Fig. 5.8) from experiments gives higher RMS peak values for axial positions in the stratified region ($z = 75$, 100 mm) compared to result at $z = 45$ mm. While at upstream location the RMS can be attributed to experimental noise and strain, the increased peak levels at downstream locations can be attributed to the increased range of available equivalence ratios due to mixing with the outer streams. At all axial locations the peak value of the MMC solution is located approximately at the same temperature as the experimental data. In MMC, the magnitude of the peak value increases at downstream locations and approaches the peak value predicted by the experimental data. The given differences can be attributed to the omission of experimental noise in MMC and to some inaccuracies in predicting the mixing between the different streams at the downstream locations and the therefore reduced range of equivalence ratios (cf. discussion surrounding Fig. 5.7). To exclude the latter effect (i.e. scatter due to variation in equivalence ratio) and to isolate deviations from the flamelet solution, the mean and RMS are doubly conditioned [34], i.e. they are computed conditioned on a specific equivalence ratio at each axial location and plotted as functions of temperature in the third and fourth columns of Fig. 5.8, respectively. The RMS of the doubly conditioned CO mass fraction predicts the deviations from the flamelet solution for a fixed equivalence ratio.

The slight underprediction of the conditional means has been discussed above, but it is apparent that trends are correctly captured by MMC. The relationship between the doubly conditioned measurements and MMC at the stratified locations is comparable to that in the fully premixed locations ($z = 15\,\text{mm}$(not shown)) and $z = 45\,\text{mm}$), and the model is appropriately handling stratification. Most important for the current study is, however, the analysis of the doubly conditioned RMS. The RMS at the upstream location displays a similar profile compared to the single conditional RMS as the flame burns only with $\phi = 0.9$. Moving further downstream, the peak value of the RMS conditioned on a fixed equivalence ratio decreases with decreasing equivalence ratio. The deviations for a fixed equivalence ratio are represented well by the MMC predictions, they are close to or within the confidence interval of the measurements, and MMC can quantitatively predict deviations from a flamelet structure.

Lastly, the radial (unconditional) profiles of the mean CO mass fraction for different axial positions are presented in Fig. 5.9. The ATF-

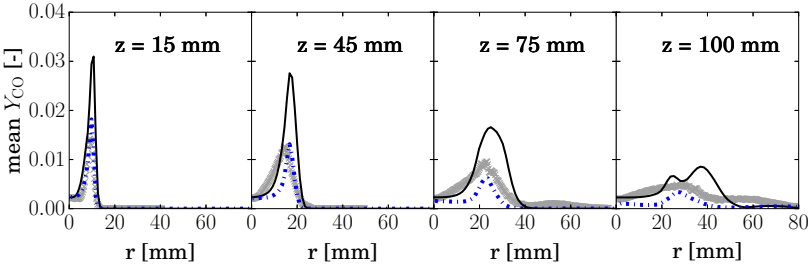

Figure 5.9: The averaged CO mass fractions as function of radial position for different downstream locations: ATF-FGM (solid black lines), MMC with $C_c = 0.5$ (blue dashed lines) and measurements (grey crosses).

FGM solution, the MMC solution and the experimental data are compared. The clear overprediction by ATF-FGM can be associated with the preserved flamelet structure and the relatively low variances of the (thickened) reaction progress variable at positions where the flamelet solution, $\mathrm{Y}_{CO}^{flmt}(c)$, peaks. In contrast, MMC and experiments agree rather well, and the observed differences in the conditional statistics and the underlying conditioning scalar seem to cancel: the higher conditional means obtained from experiments are compensated by larger fluctuations such that the measured CO peak values can be matched by the predictions. This may be somewhat fortuitous, but a clear improvement towards the ATG-FGM solution can certainly be realized by extending the ATF-FGM methodology by MMC.

5.4 Sensitivity to c_m parameter

Section 5.3 demonstrates that C_c can influence the turbulent flame propagation velocity. Here, the influence of the modelling parameter c_m is investigated. The variation of c_m influences the particle selection: lower values of c_m should enforce localness in reference space while larger values allow particles to be mixed that are further away in reference space. Values of $c_m = 0.02$, $c_m = 0.03$ and $c_m = 0.06$ are investigated for a fixed value of $C_c = 1.0$ as the latter value leads to a consistent turbulent flame speed between particle solution and ATF-FGM as demonstrated in the previous section. Using $C_c = 1.0$ provides a good correlation between the reaction progress of the particles and the LES solution that allows for meaningful conditioning of the particle pair selection on the reference field. The corresponding average physical distances of a mixing particle pair, r_m, based on the chosen c_m value are computed via Eq. (3.17). Details on the computation are stated in Sec. 4.3. The r_m values based on the specific c_m values are

given in Tab. 5.1.

Table 5.1: Average physical distance of a mixing particle pair, r_m, based on c_m (computed via Eq. (3.17)).

c_m	r_m in mm
0.02	6.8
0.03	5.9
0.06	4.3

5.4.1 Mixing distances in composition and physical space

Figure 5.10 presents the radial profiles of the mean distances of mixing particles in reference space, $d_{\tilde{c}}$, and physical space, d_x, for different c_m values at four different axial locations. The horizontal black dashed lines indicate one of the target values (for $c_m = 0.03$) and the grey dashed lines indicate the corresponding value for r_m. The profiles of $d_{\tilde{c}}$ and d_x illustrate where mixing takes place and also demonstrate the performance of the particle selection algorithm. It can clearly be seen that increasing c_m leads to increases in $d_{\tilde{c}}$ and corresponding decreases in r_m (see Eq. (3.17)) and d_x. At $z = 15\,\text{mm}$ the maximum of the averaged $d_{\tilde{c}}$ is of the order of the prescribed value of each c_m. The same holds for d_x which approximates the target value given by the corresponding r_m. The deviation from the target values further downstream can be explained with the spatial gradients that enter Eq. (3.17). Their local variation is not considered here and this leads to the deviation of $d_{\tilde{c}}$ and d_x from their target values. DNS studies of non-premixed flames [81] demonstrated that inclusion of spatial (and/or temporal) variation of the gradient of the reference scalar does not have significant effects on the results. Here, it is important to note that firstly,

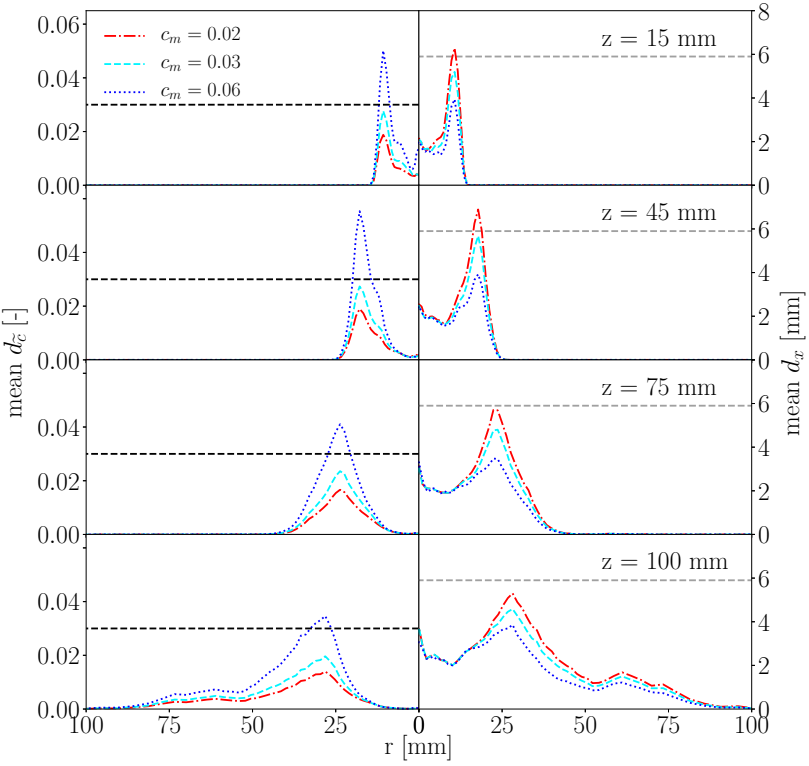

Figure 5.10: Radial profiles of mean $d_{\tilde{c}}$ and mean d_x at different axial positions. The Lagrangian solutions are represented by the red dash-dotted lines ($c_m = 0.02$), the cyan dashed lines ($c_m = 0.03$) and the blue dotted lines ($c_m = 0.06$). The horizontal black dashed lines indicate $c_m = 0.03$ and the grey dashed lines indicate the corresponding value for r_m.

decreases in c_m enforce increased localness of the mixing particles in composition space, secondly, the spatial distance between the particles increases with decreasing c_m. This is expected and demonstrates the

correct implementation of the particle selection algorithm. It should be noted, that mixing in regions with $\widetilde{c} = 0$ and $\widetilde{c} = 1$ will result in $d_{\widetilde{c}}^{p,q} = 0$ and $d_x^{p,q} \rightarrow \Delta_L$. In the unburnt and fully burnt regions, $\tilde{\chi}_c \rightarrow 0$ and $\tau_L^{\text{orig}} \rightarrow 0$, i.e. particles of equal composition mix very fast. It is apparent, however, that the current configuration sets limits to this approach: within the shear layer between ring 2 and the co-flow, $\tilde{\chi}_c \rightarrow 0$ but infinitely fast mixing between the two streams is certainly not physical and suppressed here (as indicated by $d_x^{p,q} \rightarrow 0$ in Fig. 5.10). This indicates the need for an additional conditioning of the mixing process on equivalence ratio in these regions of the flame in order to account for stratification. The application of the doubly conditioned MMC model (mixture fraction as additional reference variable) is presented in Chapter 7.

5.4.2 Correlation of reference variables and corresponding stochastic properties

For larger c_m, the particle selection algorithm (see Eq. (3.6)) correctly provides larger $d_{\widetilde{c}}$ close to the respective values of c_m and corresponding decreases in d_x. The increased distance of particle pairs, $d_{\widetilde{c}}$, would be equivalent to increased mixing across the flame front and can lead to a widening of the flame in $\widetilde{c}$-space. The influence of c_m variations on the correlation between θ^p and $\tilde{c}(x^p)$ is shown in Fig. 5.11 for different axial positions. For all c_m values a clear correlation of θ^p and $\tilde{c}(x^p)$ at all axial locations is presented and the turbulent flame propagation speed of the particles adapts to the flame propagation of the ATF-FGM solution. A moderate variation of the standard value ($c_m = 0.03$) hardly alters the correlations between θ^p and $\tilde{c}(x^p)$. Overall, the mixing model appears to be rather robust towards the exact values of c_m as long as c_m is chosen small enough, which is consistent with previous findings for the

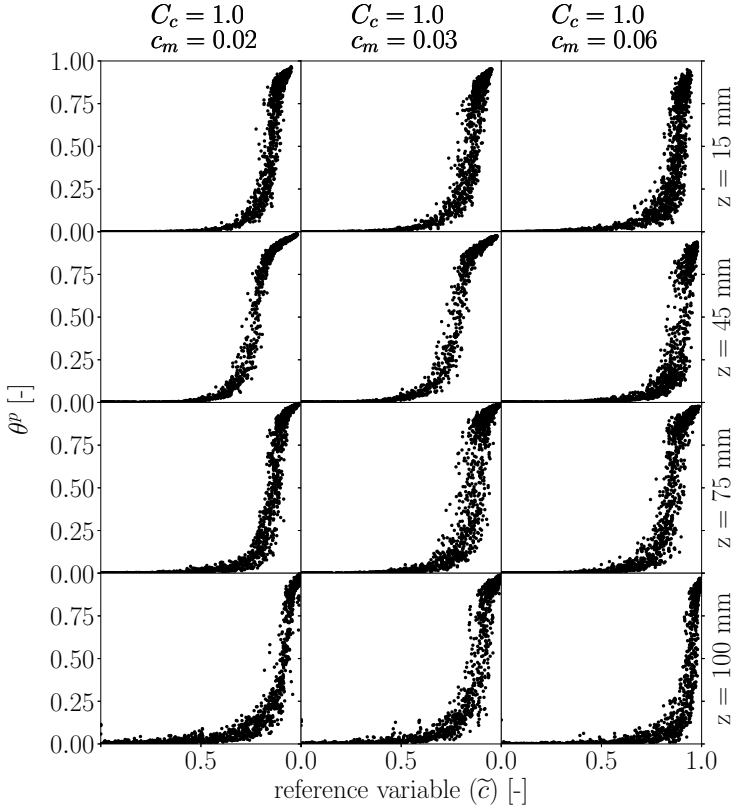

Figure 5.11: Scatterplot of normalized CO_2 mass fraction versus reference variable at different axial positions for MMC simulations with $c_m = 0.02$ (left), $c_m = 0.03$ (middle) and $c_m = 0.06$ (right) and $C_c = 1.0$ for all three cases.

equivalent parameter f_m of the non-premixed model [81].

5.4.3 Radial profiles of temperature

Figure 5.12 shows the Favre mean temperature (left) and its RMS (right) versus radial position at four axial positions for the experimental data and the MMC solutions with the three different c_m values. Close to the nozzle, the radial position of the flame is not affected by

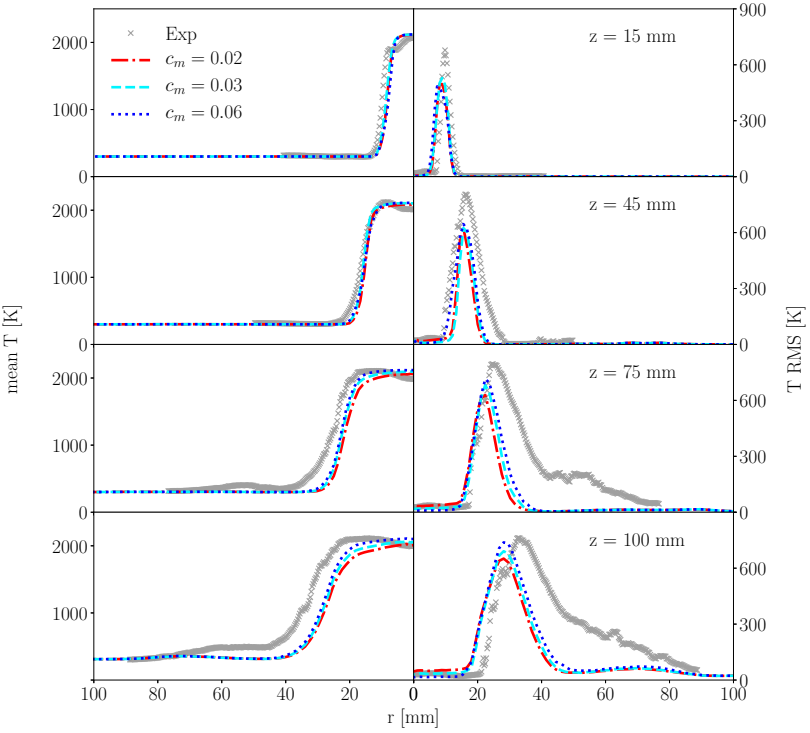

Figure 5.12: Radial profiles of the Favre mean temperature and RMS at different axial positions. Grey crosses represent experimental data and the Lagrangian solutions are represented by the dash-dotted red lines for $c_m = 0.02$, the dashed cyan lines for $c_m = 0.03$ and the dotted blue lines for $c_m = 0.06$ with $C_c = 1.0$ for all cases.

the localization in reference space. At larger downstream distances, the centerline temperature decreases for smaller c_m values. The reason for that is discussed in the next section. The position of the flame in physical space that is predicted by the Lagrangian particles does not change significantly which is consistent with the small impact of the c_m variation on the MMC correlation given in Fig. 5.11.

5.4.4 Flame structure

Larger effects of c_m can be observed when the flame structure is analyzed. Figure 5.13 shows scatter plots of CO mass fraction versus temperature at different axial positions for the three different c_m values. Experimental data are again included for reference. At first glance, the MMC results do not show much sensitivity of the flame structure on different c_m values, particularly at $z = 15\,\text{mm}$ and $z = 45\,\text{mm}$ as the scatter due to turbulence is moderate and similar in size to the experimental values. Clear differences can, however, be seen when equivalence ratios are compared. For decreasing c_m the maximum equivalence ratio of the MMC particles is lowered. This effect can be associated with the increased distance d_x of the mixing particles in physical space when increased localness in reference space is enforced. Particle diffusion is proportional to $D^p \sim d_x^2/\tau_L$ along iso-scalar surfaces in reference space (see reference [81]) and larger d_x allows for enhanced mixing in (the predominantly) axial direction as the iso-scalar surfaces align with the flame. Due to the stratification, localness in $\widetilde{c}$-space does not necessarily ensure localness in composition space. Mixing over longer physical distances may ensure closeness of the particles in reaction progress space, however, it increases the likelihood that particles of different equivalence ratios will mix within the stratified flame. This increased spatial diffusion will lead to a noticeable reduction of the particles' equivalence

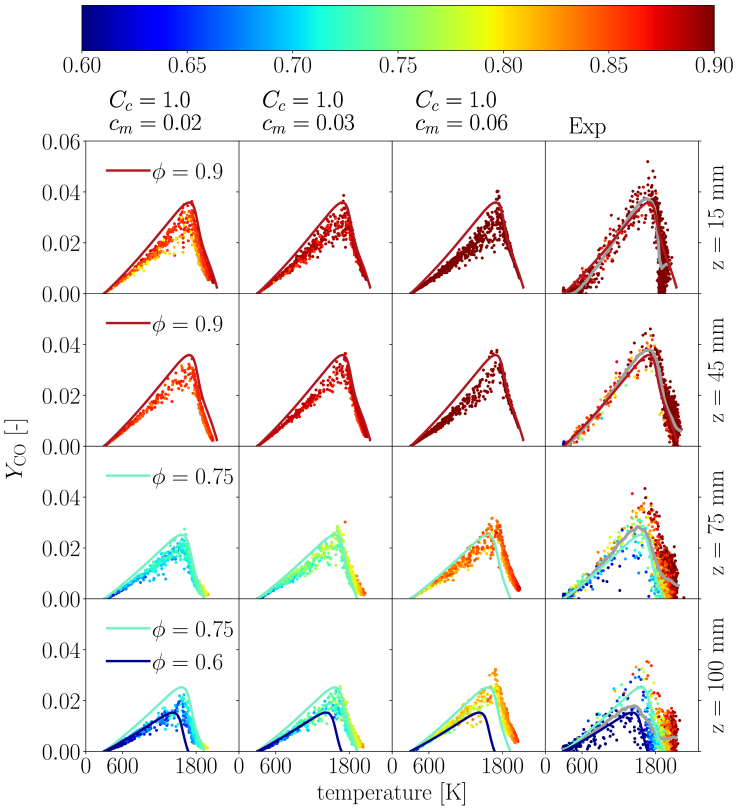

Figure 5.13: Scatterplot of the mass fraction of CO versus temperature coloured by equivalence ratio ϕ at different axial positions. MMC results are obtained with $C_c = 1.0$. First column: $c_m = 0.02$, second column: $c_m = 0.03$, third column: $c_m = 0.06$, fourth column: experimental data. The coloured solid lines are given by the FGM table for different equivalence ratios, namely $\phi = 0.6$, $\phi = 0.75$ and $\phi = 0.9$. The additional grey line indicates the conditional mean of the measurements.

ratio as can clearly be observed for $c_m = 0.02$ at all axial positions. This effect is also presented in Fig. 5.12. Decreasing c_m results in increased d_x values. As a result, the centerline temperature is decreased. As also indicated in the discussion surrounding Sec. 5.4.1, the introduction of a second reference field (such as mixture fraction) is beneficial as it ensures mixing of particles that are close in reaction progress and (!) composition space. The doubly conditioned MMC mixing model is investigated in Chapter 7. However, the standard value of c_m provides acceptable predictions of the deviations from the laminar flame structure, but a further enforcement of localness in reference space may lead to unwanted spatial diffusion and increase mixing across stratification layers. Also note that similar effects are observed in Fig. 5.3. There, an increase in C_c increases τ_L and thus reduces mixing along the iso-contour. As a consequence, larger C_c give a slight increase in centerline temperature as mixing with (colder) particles further downstream is decreased.

5.5 Summary

A sparse Lagrangian particle method is applied to a reference configuration of turbulent premixed combustion with stratification. The particle mixing model requires conditioning on a reference variable and this is taken here to be the LES-filtered reaction progress variable $\widetilde{c}$ which is obtained from an LES-ATF-FGM solution. Sensitivities towards modelling constants such as parameters for the mixing time scale and particle selection are studied. The flame locations can reasonably be predicted and results compare well with experimental data when standard modelling constants are used for particle selection, but the mixing time scale needs to be adapted. The current study demonstrates in particular that

1. the sparse particle method can approximate laminar flame structures if the particle mixing model is conditioned on the reaction progress,

2. deviations from the flamelet structure can be modelled and correspond in size to the measured fluctuations around the flamelet solution,

3. a parameter set can be found to ensure consistency between turbulent flame propagation of the ATF-FGM solution and the convective-diffusive-reactive balance on the particles (i.e. the flame location on the MMC particles accurately follows the ATF-FGM solution) and that

4. results are not overly sensitive to the exact choice of the other modelling parameters.

This study thus demonstrates the feasibility of MMC-ATF to predict turbulent premixed laboratory scale flames with stratification. However, further model validation and the application to different flame configurations is given and explored in Chapter 6. Further analysis also refers primarily to the introduction of a second reference field as it is needed to account for stratification. MMC-ATF results based on a two-dimensional reference space are presented and discussed in Chapter 7.

Chapter 6

Singly conditioned MMC-ATF simulations of flame series

The singly conditioned MMC-ATC approach is applied to a reference configuration in the previous chapter and shows promising results. It is common practice to apply novel models to a flame series for further model validation and to rule out that the model parameters are fitted to predict reasonable results for one configuration only. Through this validation against several flames the model parameters are shown to be case independent and valid over a wide range of applications. The model is shown to be robust and becomes more reliable. In this chapter the MMC-ATF approach is applied to three different configurations of the TSF series with shear and/or stratification.

Section 6.1 gives an introduction to this chapter. In Sec. 6.2 the mean quantities for all three flame configurations of the MMC solu-

tions are compared with experimental data. Section 6.3 presents the correlation of the reference variable and the corresponding stochastic properties. To investigate the flamelet structure of the three different configurations, the CH_4 and CO mass fractions as functions of the temperature for the MMC approach are compared with the experimental results in Sec. 6.4.

6.1 Introduction

The TSF series depicts a good validation setup for computational models and was investigated experimentally for different configurations with and without shear and stratification [62, 67]. It had been selected as a target flame of the International Workshop on Measurement and Computation of Turbulent Flames [30] and has served in many publications as a reference case for model validation [22, 43]. The experimental setups of the flame configurations are introduced in Chapter 4. For the simulations, again, the reference variable is chosen as the LES-filtered reaction progress variable, $\tilde{c}$ and the MMC modelling parameters $c_m = 0.03$ and $C_c = 0.5$ are applied, which resulted in accurate predictions in the previous chapter. Note, that minor changes in the grid resolution are performed compared to the previous chapter. All simulations of the three flames are based on the same grid and the LES grid consist of approximately 0.9 million cells to account for the phenomena appearing in all three flames. The results are rather insensitive to the grid refinement.

6.2 Mean quantities

Figure 6.1 compares the mean radial positions of the flame brush (indicated by $T'_{\max}$) and the mean locations of the stratification layer (indicated by $\phi_m = 0.75$) only for experimental data of the three flame configurations TSF-A, TSF-C and TSF-G. At the upstream locations

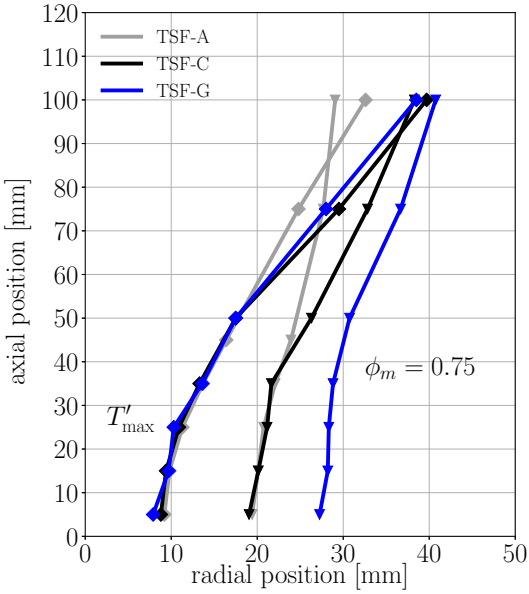

Figure 6.1: The mean radial positions of the center of the flame brush that is taken as the position of the maximum temperature RMS, $T'_{\max}$, is indicated by diamonds and the mixing layer (indicated by $\phi_m = 0.75$) is represented by triangles for experimental data of the three different configurations TSF-A, TSF-C and TSF-G.

($z < 50\,\mathrm{mm}$) there is no difference for the mean radial positions of the flame brush between the different configurations as the zones of stratification or shear have not yet merged with the flame front that

is still localized within the first ring. Moving further downstream differences can be observed. The flame position for TSF-C is shifted to the highest radial location as the axial momentum of slot 2 is reduced and the flame can therefore establish itself at positions closer to the nozzle in regions where the flame interacts with the unburnt mixture originating from this slot. The flame position for TSF-G is located at larger radii compared with TSF-A as the richer mixture of slot 2 in TSF-G allows for an increased flame spread. The mean locations of the stratification layer are similar for TSF-A and TSF-C at the upstream locations ($z < 45\,\mathrm{mm}$). Due to similar reasons as described above, the mean radial locations of the stratification layer for TSF-C are shifted to higher radial positions further downstream. Hence, the intersection of the mean positions of the flame brush and the mixing layer is further downstream compared to TSF-A. The mean location of $\phi = 0.75$ is shifted for TSF-G to larger radii, as the fluid in the second slot is of $\phi = 0.9$. The intersection of the mean flame brush and the mixing layer is further downstream compared to the other two configurations.

A more quantitative comparison for the evolution of the three different flames is provided by the radial profiles of mean temperature and its RMS at four axial positions as depicted in Figs. 6.2-6.4, respectively. The ATF-FGM solutions, the MMC results and the experimental data are presented for each configuration. At $z = 15\,\mathrm{mm}$ there is no difference in the mean temperature profiles for the different configurations as the flame is not in the zones of stratification or shear yet as mentioned above. The widest temperature profile for TSF-C at further downstream locations ($z > 45\,\mathrm{mm}$) is correctly predicted by the ATF-FGM solution. Similarly, ATF-FGM correctly predicts the wider flame for TSF-G compared with TSF-A. A second temperature peak of the experimental data is noted for TSF-G at larger radii in Fig. 6.4 that stems from products mixing with coflowing air, because the low coflow veloc-

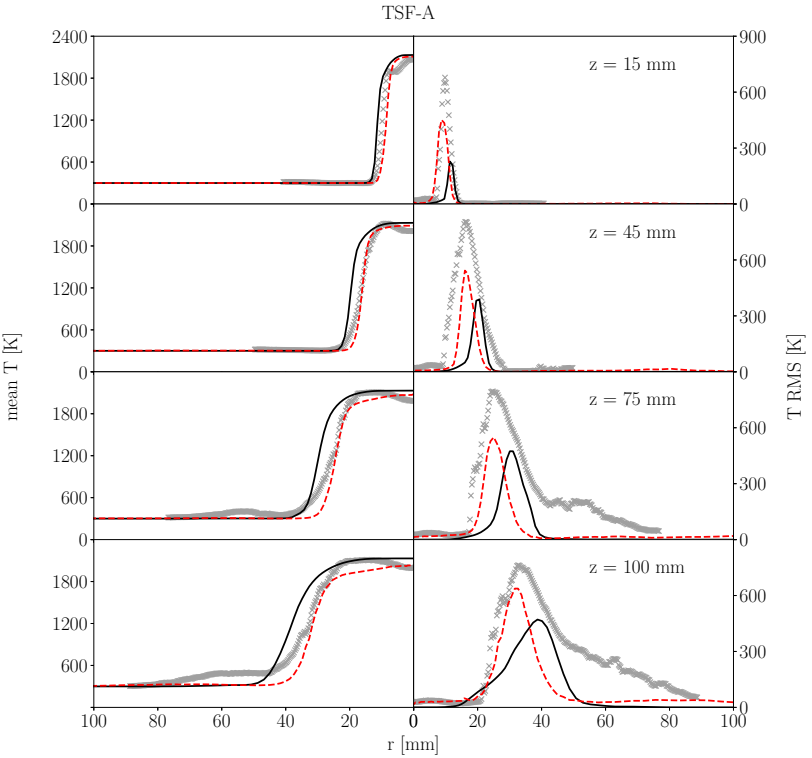

Figure 6.2: Radial profiles of Favre mean temperature and RMS at different axial positions for TSF-A. The grey crosses represent the experimental data, the lines represent the ATF-FGM solution and the dashed lines represent the MMC solution.

ity of 0.1 m/s allows for some reverse flow of products from the outer, downstream region of the flame. These zones are excluded from the conditional analysis (see e.g. Figs. 6.6 and 6.7) as the inner structure of the flame is of importance and secondary mixing effects are not the focus of this work. TSF-A is the most narrow and the flame position is

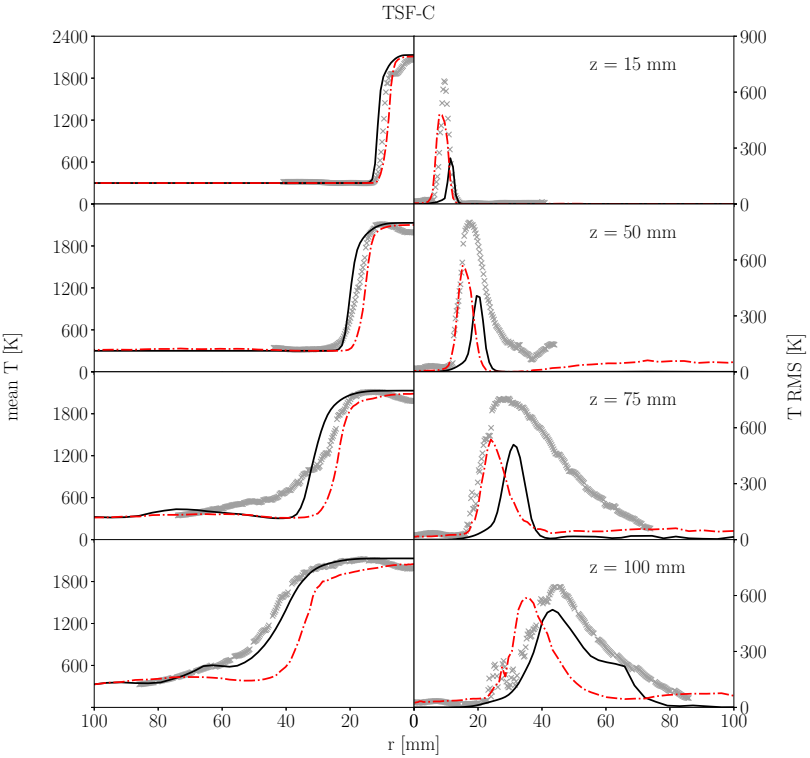

Figure 6.3: Radial profiles of Favre mean temperature and RMS at different axial positions for TSF-C. The grey crosses represent the experimental data, the lines represent the ATF-FGM solution and the dash-dotted lines represent the MMC solution.

again well captured by the simulation. The flame positions predicted by MMC are slightly shifted towards smaller radii, which leads to excellent predictions of flame position at $z = 15\,\mathrm{mm}$ and $z = 45/50\,\mathrm{mm}$ for all flames and at $z = 75\,\mathrm{mm}$ and $z = 100\,\mathrm{mm}$ for TSF-A (see Fig. 6.2). MMC flame spread is somewhat too narrow for TSF-C and G at this

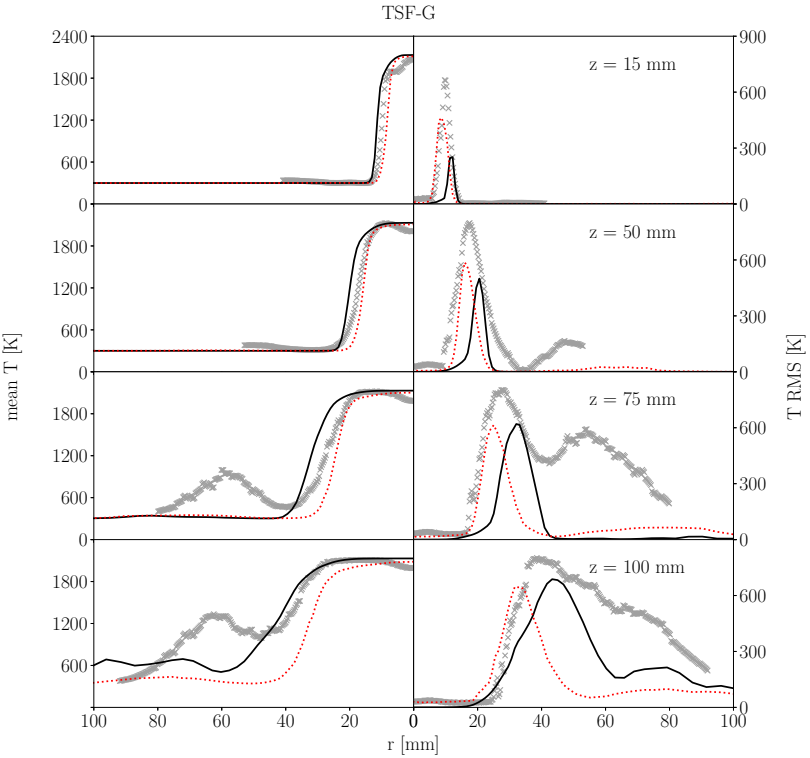

Figure 6.4: Radial profiles of Favre mean temperature and RMS at different axial positions for TSF-G. The grey crosses represent the experimental data, the lines represent the ATF-FGM solution and the dotted lines represent the MMC solution.

latter downstream locations. Possible improvements (or deteriorations) with respect to flame position should, however, not be over-emphasized as MMC's particle mixing is conditioned on the ATF solution, and flame positions extracted from particle data will be correlated with the ATF-FGM solution. The relative position of the MMC solution

to ATF-FGM is explained below where the correlation between θ^p and $\tilde{c}(x^p)$ is discussed (cf. Fig. 6.5). The corresponding temperature RMS are very similar to each other at upstream positions. The temperature RMS peak values are aligned with the mean temperature gradients of similar magnitude at all axial positions. The constant underprediction of the RMS for all ATF-FGM simulations is expected as the thickening of the flame by the ATF method will prevent an accurate prediction of the turbulent fluctuations by the LES. For the MMC results this is different as the Lagrangian particles represent an instantaneous and local solution of the composition space, and the RMS can therefore expected to be closer to the experimental data. It is again noted that at all locations the ATF-FGM solutions predict slightly wider temperature profiles compared with the experimental data. This issue is known and discussed in the previous chapter (cf. also Fiorina *et al.* [22]). Based on the same arguments as in the previous chapter, the optimization of the ATF-FGM solution (e.g. inclusion of enthalpy as a third FGM parameter) shall not be the primary objective of the current contribution. The results show, however, that the simulations predict the correct trends given by the experiments. The reader is reminded here, that in the context of the MMC modelling attempted here, the ATF-FGM solution is required to predict the flame position with adequate accuracy. Details of the flame structure, in particular the deviations from a low dimensional manifold imposed by the flamelet, shall be captured by the solution of the notional MMC particles and is investigated in Sec. 6.4.

6.3 Correlation of reference variables and corresponding stochastic properties

Conditioning on the reference variable is only useful if the thermo-chemical state on the particles - represented by θ^p - correlates with the reference variable, i.e. with the LES-filtered reaction progress $\widetilde{c}(x^p)$ interpolated to the particle position. Figure 6.5 shows this correlation for all three flames at $z = 15\,\mathrm{mm}$, $z = 75\,\mathrm{mm}$ and $z = 100\,\mathrm{mm}$. For now,

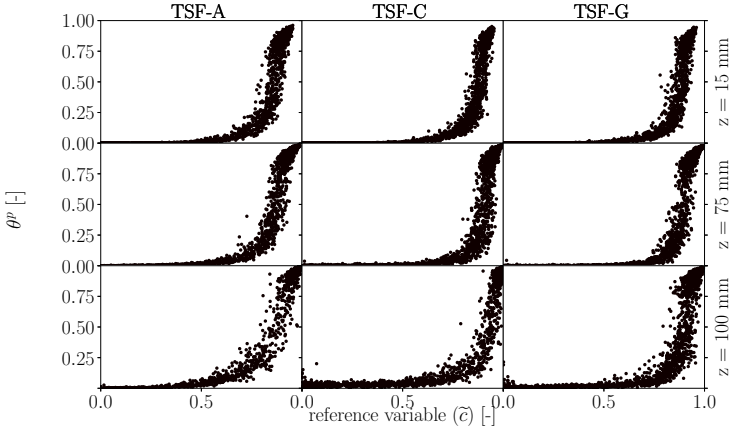

Figure 6.5: Scatter plot of normalized CO_2 mass fraction versus reference variable at $z = 15\,\mathrm{mm}$, $z = 75\,\mathrm{mm}$ and $z = 100\,\mathrm{mm}$ for MMC simulations of three different flame configurations from left to right: TSF-A, TSF-C and TSF-G.

any apparent mapping is sufficient and the given correlation indicates that reaction on the particles occurs in a relatively narrow $\widetilde{c}$-space for all axial positions. The position and shape of the correlation for the different flame configurations are quite similar at each axial location. Flame thickness, δ, and reaction progress are related by $\delta \approx \Delta\widetilde{c}/\nabla\widetilde{c}$.

The relevant $\Delta\tilde{c}$ for the ATF-FGM solution is $\Delta\tilde{c} = 1$ while the spatial extent of the flames on the particles is $\Delta\tilde{c} \approx 0.1 - 0.2$. The flame will therefore be much thinner in physical space and a detailed assessment of the flame thicknesses predicted by MMC and ATF-FGM has been demonstrated in the previous chapter.

6.4 Flame structure

Figure 6.6 shows the predicted CH_4 mass fractions as functions of temperature compared with measurements at three axial positions. The

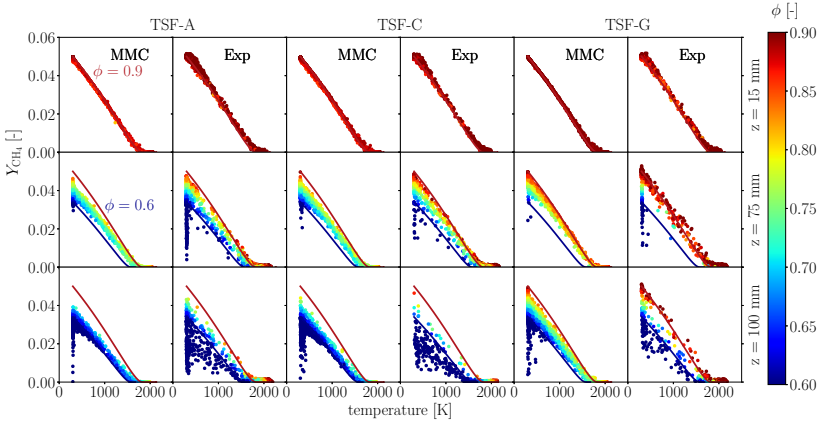

Figure 6.6: Scatterplot of mass fraction of CH_4 versus temperature coloured by equivalence ratio ϕ at different axial positions. The MMC data is compared with experimental data for all three flame configurations from left to right: TSF-A, TSF-C and TSF-G. The coloured solid lines are given by the FGM table for different equivalence ratios, namely $\phi = 0.6$ and $\phi = 0.9$ and added for guidance only.

reader is reminded here, that the key modelling challenge for a par-

ticle method like MMC is not only to predict the correct deviations from the flamelet structure, but it is equally important to demonstrate that MMC can predict flamelet-like flame zones where the experiments predict a thin flame front. In experiments and simulations alike, the samples for conditional quantities are collected from within the flame brush only by limiting the radial extent of the sampling volume. The results are coloured by the equivalence ratios $\phi \in [0.6, 0.9]$, where the limits of this range correspond to the equivalence ratios of rings 1 and 2 of the stratified configurations, respectively. Additionally and for guidance only, the coloured solid lines depict the flamelet solutions of the FGM table for equivalence ratios $\phi = 0.6$ and $\phi = 0.9$. At $z = 15\,\mathrm{mm}$, the CH_4 mass fraction depends linearly on the temperature for the burning fluid with $\phi = 0.9$. This holds for all three flame configurations and is expected as a fully burning premixed flame is observed. But most importantly, it demonstrates that the particle method does not lead to an artificial thickening of the flame due to mixing across the flame front and is capable of preserving a flamelet structure. The larger experimental scatter at $z = 15\,\mathrm{mm}$ where reaction zones are fully premixed, can be again explained by experimental noise of the order of 4.5% (ref. [2]) as mentioned in the previous chapter. Further downstream at $z = 75\,\mathrm{mm}$ the scatter in equivalence ratio increases depending on the flame configuration and is least pronounced for TSF-G. Here, the difference between scatter caused by turbulence (quantified by the scatter for a fixed equivalence ratio) and mixing of fluid elements with different equivalence ratios as indicated by the colors in particular at $z = 75\,\mathrm{mm}$ should be emphasized. The scatter is primarily caused by mixing and not necessarily by strong deviations of the solution from the flamelet profile. Therefore, the scatter remains low (in experiments as well as predictions) for flame TSF-G without stratification. At $z = 100\,\mathrm{mm}$ scatter in equivalence ratio is shown for mainly

fluid with $\phi < 0.6$. Again, the scatter is more pronounced for TSF-A and TSF-C. For TSF-G fluid with $\phi = 0.9$ remains, but not many realizations in between. The MMC solutions agree quite well with the measurements for all three flames and depict higher equivalence ratios for TSF-G. The scatter in equivalence ratio is slightly underpredicted by MMC at this downstream location, which can be attributed to an overprediction of mixing between the fluids of rings and the co-flow.

An analysis of intermediate species allows for an additional assessment of the deviation from the flamelet structure, and Fig. 6.7 shows a comparison between computed and measured CO mass fractions conditioned on temperature. The results are again coloured by the equivalence ratio. At $z = 15\,\text{mm}$ the different flame configurations predict similar CO mass fractions. For the stratified setups the peak value is slightly increased compared with TSF-G, but these differences are within the measurement uncertainty for CO of +/- 10%. As the flame is located between pilot and slot 1 similar results for all flames are expected and the results should not be affected by shear or stratification. All configurations depict a flamelet structure as the CO mass fraction follows the FGM solution for $\phi = 0.9$, and the scatter indicates only small deviations thereof. At $z = 75\,\text{mm}$, the equivalence ratio for the premixed flame is higher when compared with the stratified setups (TSF-A and TSF-C), which is consistent with Fig. 6.6. The stratified configurations show an increased scatter (from $\phi = 0.6$ to $\phi = 0.9$) as they feature faster mixing with fluid of decreased equivalence ratio. The MMC results approximate the flamelet solution, but the conditional means tend to be lower than the measurements for temperatures below 1800 K. Reasons for the systematic underprediction are not entirely clear. Some discrepancy can be explained by measurement uncertainty but some might be associated with differential diffusion effects as demonstrated in [21]. There, increases of conditionally averaged CO by

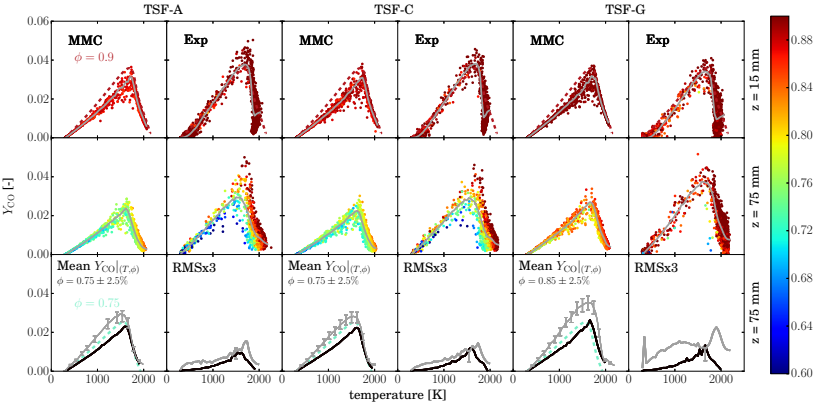

Figure 6.7: Comparison of the MMC results with experimental data for all three flame configurations. Upper and middle row: Scatterplot of mass fraction of CO versus temperature coloured by equivalence ratio, ϕ, at different axial positions. The coloured dashed lines represent the FGM data for different equivalence ratios. The grey solid lines indicate the conditional mean of the MMC solution and the measurements, respectively. Bottom row: conditional mean and RMS for specific equivalence ratios of the MMC results (black solid lines) and the experimental data (grey solid lines).

up to 14% could be observed when non-unity Lewis numbers were considered. The underprediction should not, however, be associated with an inadequate choice of the MMC modelling parameters. The MMC predictions somewhat lower than the flamelet solution are expected and are caused by turbulence as increased strain should tend to reduce predicted CO [34]. To isolate deviations from the flamelet solution, the mean and RMS are double conditioned [34], i.e. they are computed conditioned on a specific equivalence ratio and plotted as functions of temperature for $z = 75\,\text{mm}$ in the last row of Fig. 6.7. Different

equivalence ratios needed to be chosen depending on the configuration. The error bars for the conditional means represent again (analogously to the previous chapter) the estimated calibration uncertainty of 10% and the one-sided error bars in the RMS measurements indicate again the expected contribution of measurement uncertainty due to photon statistics. The underprediction of the conditional mean has been discussed above, but more important for the assessment of the particle method to predict the correct flame structure is a comparison of the conditional RMS. Here, predicted deviations from the flamelet structure are excellent for flames TSF-A and TSF-C. The agreement is less perfect for TSF-G as only a small overlap of predicted and measured equivalence ratios exist.

6.5 Summary

Large eddy simulations are performed for different configurations of the TSF series and are coupled with a sparse Lagrangian particle version of MMC. As the particle mixing model is a conditional mixing model where stochastic particles that mix are selected under the condition that their distance in the LES-filtered, thickened reaction progress variable space is small, localness of mixing in composition space is ensured. Unphysical mixing across the flame front is avoided. MMC-ATF predictions of all three flame configurations investigated in this chapter are good independent of the level of stratification and shear. Most importantly, for one fixed set of parameters the MMC-ATF predictions follow the trends of the different flames within the series. This demonstrates the feasibility of this novel MMC method for the modelling of turbulent premixed combustion with stratification for a wide range of applications. Furthermore, MMC can preserve a flamelet structure and deviations thereof aligned to experimental data for all investigated

flame configurations are satisfactorily predicted. This suggests that the model is applicable across the different flame regimes without any prior assumptions on the inner flame structure. The next chapter presents the development of the MMC-ATF approach where the reference space is extended by the filtered mixture fraction to explicitly account for stratification.

Chapter 7

Doubly conditioned MMC-ATF simulations of reference configuration

This chapter is motivated by the observations in Chapter 5 where the singly conditioned MMC model does not explicitly account for stratification. Hence, the reference space is extended by the LES-filtered mixture fraction compared to the model applied in the previous chapters. The underlying theory has been introduced in Chapter 3. In doubly conditioned MMC the localness parameters c_m, f_m and r_m specify the distances in reference and physical space. The standard value found in the literature is $f_m = 0.03$ for non-premixed applications [12, 81]. In premixed combustion the results of the previous two chapters demon-

strate that the value of $c_m = 0.03$ performs well. These values are also used throughout this investigation.

In Sec. 7.1 the differences compared to singly conditioned MMC and especially the choice of the r_m value are evaluated. The investigated MMC cases of this chapter are summarized in Sec. 7.2. In Sec. 7.3 the results of an r_m sensitivity study are presented. Predictions of the doubly conditioned MMC approach are compared with results of the singly conditioned MMC approach in Sec. 7.4. In Sec. 7.5 different mixing time scale models for the doubly conditioned MMC approach are discussed. The accuracy of the model is assessed by comparison with experimental data of the reference configuration TSF-A.

7.1 Double conditioning strategies

By introducing a second reference variable it is necessary to investigate the related changes in the MMC mixing model. In doubly conditioned MMC there exist two reference variables and the corresponding localness parameters are c_m and f_m. The computation of r_m is based on these localness parameters and stated in Sec. 3.3.3.2. Additionally, the definition of r_m is based on the Eulerian gradients of the reference variables which vary depending on the position in the flame. Based on the choice where the gradients are evaluated, the value of r_m differs remarkably (see Sec. 4.3). Hence, results for an r_m variation are presented in Sec. 7.3. The mixing time scale within the flame front has been validated in the previous chapters by predicting the correct flame propagation speed. The definition of the mixing time scale of particles with equivalence ratio variations is investigated in this chapter. Common definitions of the mixing time scale are based on the actual mixing distance in reference space. Two different approaches for the mixing time scale in turbulent premixed combustion with stratification

are investigated in Sec. 7.5.

7.2 Investigated cases

Seven different cases for the assessment of the doubly conditioned MMC model as listed in Tab. 7.1 are investigated. The first case uses the

Table 7.1: Overview of conditioning approaches and different mixing time scale combinations for MMC coupled with the ATF-FGM approach.

Case	Conditioning	Model for τ	Averaging τ_L^p & τ_L^q	r_m in mm
1	singly (on $\tilde{c}$ only)	**original**, Eq.(3.19), $\xi = c$	max	5.9
2	doubly	**original**, Eq.(3.19)	harmonic	5.9
3	doubly	**original**, Eq.(3.19)	harmonic	6.9
4	doubly	**original**, Eq.(3.19)	harmonic	8.7
5	doubly	**original**, Eq.(3.19)	max	6.9
6	doubly	**a-iso**, Eq.(3.22)	harmonic	6.9
7	doubly	**a-iso**, Eq.(3.22)	max	6.9

singly conditioned MMC approach which is applied in the previous two chapters and is presented here for comparison. Cases 2, 3 and 4 are based on doubly conditioned MMC and present a variation in r_m with the mixing time scale given by the original model (cf. Sec. 3.3.3.3). The results of the different cases are investigated in Sec. 7.3. The

comparison of the results of the singly conditioned MMC approach (case 1) with the doubly conditioned MMC approach (case 3) is presented in Sec. 7.4. Cases 3 and 5 are based on the doubly conditioned MMC approach coupled with the same original model for the mixing times scale and $r_m = 6.9\,\text{mm}$, but each uses a different averaging procedure for $\tau_L^{p,q}$. Cases 6 and 7 use doubly conditioned MMC based on the anisotropic approach (cf. Sec. 3.3.3.3) for the mixing time scale and $r_m = 6.9\,\text{mm}$, but also differ in the averaging procedure of the two mixing time scales of the particle pair. The influence of the different mixing time scales on the simulation results is presented in Sec. 7.5.

7.3 r_m variation for doubly conditioned MMC

Figure 7.1 compares the predicted positions of the flame brush (indicated by T'_{max}) and the mixing layer (indicated by $\phi_m = 0.75$) with the corresponding positions from experiments. The simulation results are given by $r_m = 5.9\,\text{mm}$ (case 2), $r_m = 6.9\,\text{mm}$ (case 3) and $r_m = 8.7\,\text{mm}$ (case 4) as stated in Tab. 7.1. The values at "Pos-c" ($r_m = 5.9\,\text{mm}$) and "Pos-cf" ($r_m = 8.7\,\text{mm}$) represent feasible minimum and maximum values for r_m as computed in Sec. 4.3. The center of the flame brush and the mean location of the mixing layer is predicted quite accurately by the MMC results for all three r_m values. The predicted center of the flame brush is similar for the MMC results for all r_m values. The predictions of the mean location of the stratification layer do not show any considerable differences for the different r_m values. Overall, the results are quite insensitive to the choice of the r_m value and an intermediate value setting $r_m = 6.9\,\text{mm}$ (case 3) is used in the following investigations.

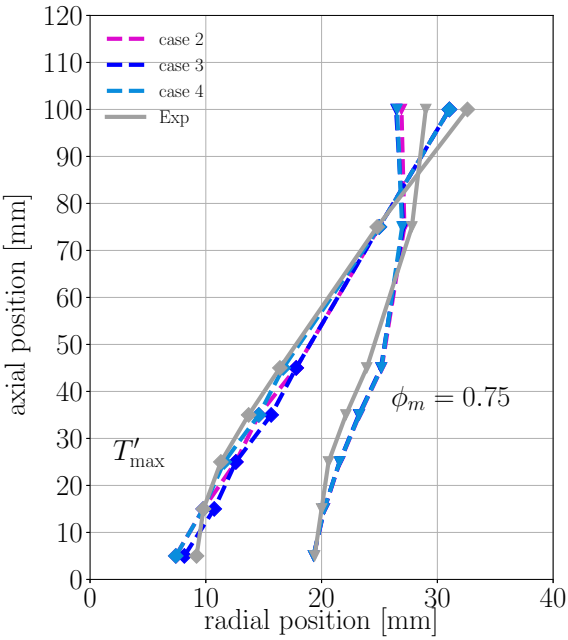

Figure 7.1: The mean radial positions of the center of the flame brush that is taken as the position of the maximum temperature RMS, $T'_{\max}$, is indicated by diamonds, the mean location of the stratification layer, $\phi_m = \frac{\phi_1+\phi_2}{2}$, is represented by triangles. The solid lines indicate the experimental data and the dashed lines represent the MMC data: purple lines (case 2), blue lines (case 3) and lightblue lines (case 4). The explanation of the case numbers is given in Tab. 7.1.

7.4 Comparison of doubly and singly conditioned MMC

For the singly conditioned approach r_m is determined from Eq. (3.17) (cf. Sec. 3.3.3.2) and consistent to the data available in the previous two chapters. Therefore, r_m is set to $r_m = 5.9\,\text{mm}$ which is the value

calculated at the characteristic location "Pos-c". The doubly conditioned MMC approach is represented here by case 3 with $r_m = 6.9\,\mathrm{mm}$ as discussed in the previous section.

7.4.1 Flame brush and mixing layer position

Figure 7.2 compares the predicted positions of the flame brush (indicated by T'_{max}) and the mixing layer (indicated by $\phi_m = 0.75$) with the corresponding positions from experiments. The dashed lines indicate MMC predictions while the solid lines show the experimental data. Note that the figure also includes results of the anisotropic mixing time scale model and these results are discussed below in Sec. 7.5. Figure 7.2 shows that the center of the flame brush is matched quite accurately for the singly conditioned MMC results and only small deviations between singly and doubly conditioned MMC results can be identified. Also, the prediction of the center of the mixing layer is identical for the two approaches up to the axial position $z = 45\,\mathrm{mm}$. However, further downstream (between $z = 75\,\mathrm{mm}$ and $z = 100\,\mathrm{mm}$) the singly conditioned MMC predicts the mixing layer at notably smaller radial positions.

7.4.2 Radial profiles of mixture fraction

The differences in mixture fraction of singly and doubly conditioned MMC-ATF in the previous section are explained with the aid of Fig. 7.3 that shows radial profiles of mean mixture fraction at two different axial positions for the singly and doubly conditioned approaches. At $z = 15\,\mathrm{mm}$ the profiles look quite similar and only very small differences can be observed for the highest mixture fraction values. Further downstream, however, the mixture fraction profile predicted by the singly conditioned approach is broadened, leading to lower mixture fraction

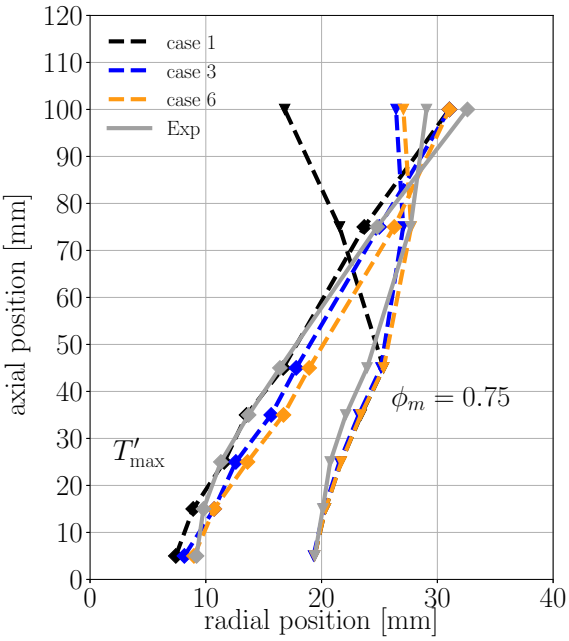

Figure 7.2: The mean radial positions of the center of the flame brush that is taken as the position of the maximum temperature RMS, $T'_{\max}$, is indicated by diamonds, the mean location of the stratification layer, $\phi_m = \frac{\phi_1+\phi_2}{2}$, is represented by triangles for the reference configuration TSF-A. The solid lines indicate the experimental data and the dashed lines represent the MMC data: black lines (case 1), blue lines (case 3) and orange lines (case 6). The explanation of the case numbers is given in Tab. 7.1.

values at $r < 55\,\text{mm}$. This overprediction of diffusion is a direct result of the lack of conditioning on mixture fraction space. Particles for mixing are selected independent of their reference mixture fraction values leading to enhanced mixing across the stratification layer which then causes the deviation from the measured profiles. This is even

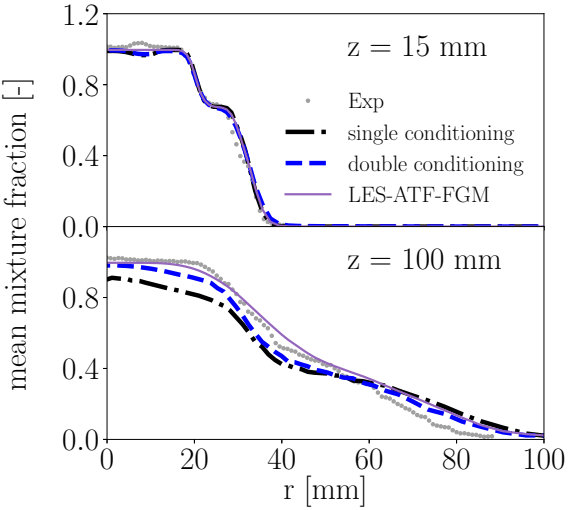

Figure 7.3: Radial profiles of Favre mean mixture fraction at different axial positions. Grey dots represent experimental data. Dotted dashed lines represent the singly conditioned MMC solution, dashed lines represent the doubly conditioned MMC solution and solid lines represent the LES-ATF-FGM solution.

more pronounced further downstream as the smaller mixing time scale within the flame front causes faster mixing. Upstream, the flame front is sufficiently far away from the stratification layer, mixing is slow and omission of conditioning in mixture fraction space has less effect. In contrast, the introduction of two reference fields preserves localness in the combined progress and mixture fraction space throughout the domain and improves results. This fact is strengthened by comparing the MMC data with the ATF-FGM solution, which is also given in Fig. 7.3. At the upstream position the profiles are quite similar. At the downstream position the doubly conditioned approach is much closer to the ATF-FGM solution and also closer to the experimental data when

compared to the results of the singly conditioned MMC.

While the results of the doubly conditioned MMC predict the radial profiles of the mixture fraction more realistically, the improvement hardly influences the flame position. The mixing of fluid of different equivalence ratio is described by the localization of the particles close in Eulerian mixture fraction space and by the definition of the mixing time scale based on mixture fraction. Especially, the mixing time scale based on the mixture fraction is dominated away from the flame front with the flame sensor $\Omega = 0$ (cf. Eq. (3.23)). Hence, the doubly conditioned MMC model is more reliable as the mixing in the stratification layer is treated directly.

7.5 Comparison of mixing time scale models

7.5.1 Mean quantities

As can be seen in Fig. 7.2 the predicted flame positions and the positions of the stratification layer are relatively insensitive to the exact implementation of the mixing time scale, and the results of cases 3 and 6 agree reasonably well with the experimental data. The results of cases 5 and 7 are also very similar and not shown in Fig. 7.2 for clarity of presentation. Comparing the different mixing time scale models, a slight shift to higher radial positions for the anisotropic mixing time scale is observed. This effect will be further investigated below (cf. also Fig. 7.5).

The mean flame brush and the mean mixing layer positions provide a rather qualitative measure. A more quantitative comparison for the assessment of mixing is provided by the radial profiles of mean

mixture fraction and its RMS as depicted in Fig. 7.4 for the four axial locations $z = 15\,\text{mm}$, $z = 45\,\text{mm}$, $z = 75\,\text{mm}$ and $z = 100\,\text{mm}$. The mean mixture fraction profiles are accurately predicted by all four

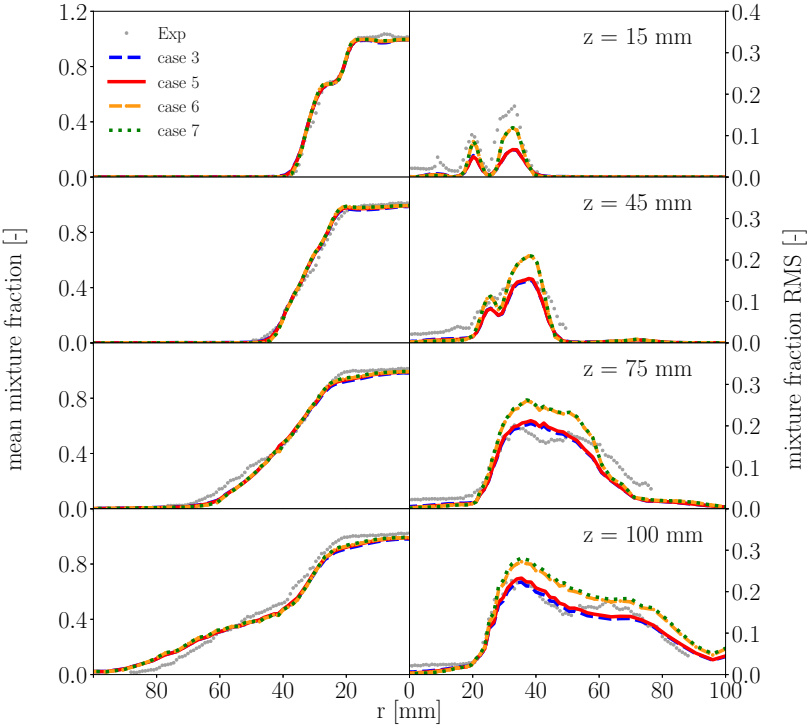

Figure 7.4: Radial profiles of Favre mean mixture fraction and RMS at different axial positions. Grey dots represent experimental data and the coloured lines represent the MMC data: blue lines (case 3), red lines (case 5), orange lines (case 6) and green lines (case 7). The explanation of the case numbers is given in Tab. 7.1.

cases and differences are very small. However, the original model tends to predict a lower mixture fraction RMS when compared with the

anisotropic model. This can be attributed to the different mixing time scale definitions and is - at least for the regions in the flame where non-premixed mixing dominates - expected as $\tau^f_{\text{a-iso}} > \tau^f_{\text{orig}}$ in non-premixed flames [81]. The smaller mixing frequency for the anisotropic model will reduce mixing and allow for larger fluctuations around the mean as observed in the figure. The differences in τ_L will also be discussed further below. Here, it is also observed that the choice for averaging the time scales of the two particles yields only small changes of the mixture fraction RMS and only at downstream locations. Reducing numerical diffusion, i.e. taking the maximum of the two time scales, results in a slightly increased mixture fraction RMS compared to the harmonic mean. However, the sensitivity of the results to the choice of the mixing time scale of a particle pair is generally very small, indicating overall relatively equal time scales for the two particles when they mix.

7.5.2 Correlation of reference variables and corresponding stochastic properties

The similarity of results between the two mixing time scale models can be better understood when analyzing the correlation between the stochastic reaction progress θ^p and mixture fraction z^p with the corresponding reference fields $\tilde{c}$ and $\tilde{f}$. Remember that the stochastic reaction progress and mixing evolve independently of the LES-filtered fields, however, a good correlation between the corresponding quantities is required. If the quantities were decorrelated, the LES-filtered field would not characterize the stochastic particles' species composition and conditioning of mixing on the reference field would become meaningless. Figure 7.5 presents scatter plots of θ^p versus $\tilde{c}(x^p)$ and z^p versus $\tilde{f}(x^p)$ at two axial locations. The correlations of cases 3 (original mixing model) and 6 (anisotropic mixing model) are compared here, both

employing the harmonic mean of the mixing time scales for a particle pair. First and most importantly, one can observe that the LES and

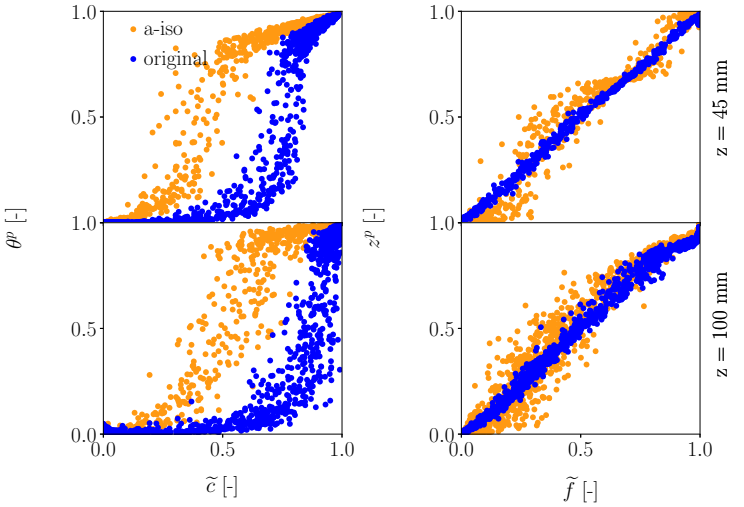

Figure 7.5: Scatter data θ^p versus $\tilde{c}(x^p)$ (first column) and z^p versus $\tilde{f}(x^p)$ (second column) of MMC results with the original mixing model (case 3) and the anisotropic mixing model (case 6) at different axial positions.

the stochastic solutions do not decorrelate and conditioning on the reference variables ensures localness in composition space even if particles are far away in physical space. As discussed in the previous two chapters, the relatively steep and narrow θ^p-profile indicates that firstly, the stochastic solution correctly predicts a much smaller (and close to realistic) flame thickness than the thickened LES field provides. This can easily be explained with the finite rate chemistry directly integrated on the particles: once a stochastic particle ignites it reaches the fully burnt state within the correct chemical time scale, while the chemical

source term for the LES field is artificially reduced by the thickening factor F, leading to a wider flame brush. Secondly, the flame on the particles propagates with the consistent turbulent flame speed of the flame predicted by the LES. If the stochastic solution over-predicted the flame speed, the θ^p-profile would increase from zero to one at $\tilde{c} = 0$. If it was under-predicted, the steep increase of θ^p would be observed at $\tilde{c} = 1$. The correlations are somewhat different for each mixing time scale model. However, the exact position of the steep increase of θ^p in $\tilde{c}$-space is not crucial as long as a clear correlation between θ^p and $\tilde{c}$ is preserved and conditioning on $\tilde{c}$ (localness in reference space) is correlated with localness in particle composition space.

Figure 7.5 (right) shows the correlation of the stochastic mixture fraction, z^p, versus the LES-filtered mixture fraction, $\tilde{f}$. In contrast to the correlation of the reaction progress, the scatter plots show an overall linear shape. This is expected as mixture fraction is a conserved scalar and no differences in source terms exist between stochastic and LES solution that could lead to the steepening effects. When comparing the results of the different mixing models it is apparent that the anisotropic approach predicts more scatter which is consistent with the results described in Fig. 7.4. The increased scatter is expected as Vo *et al.* [81] observed higher (and more accurate) conditional fluctuations for the anisotropic model when compared with the original model.

Figure 7.6 depicts the mixing time scales versus the two reference variables at different axial positions and corroborates above findings. The mixing time scale given by the original model exhibits more scatter when compared with the anisotropic mixing model. This can be attributed to the square of the particle distance in reference space ($d_{\tilde{c}}$ or $d_{\tilde{f}}$) that appears in the numerator of the model and which is subject to some level of scatter itself. In contrast, $\delta^{Y_{CO_2}}$ is a constant and this reduces fluctuations in $\tau_{\text{a-iso}}$. It is also seen that $\tau_{\text{a-iso}}$ tends to

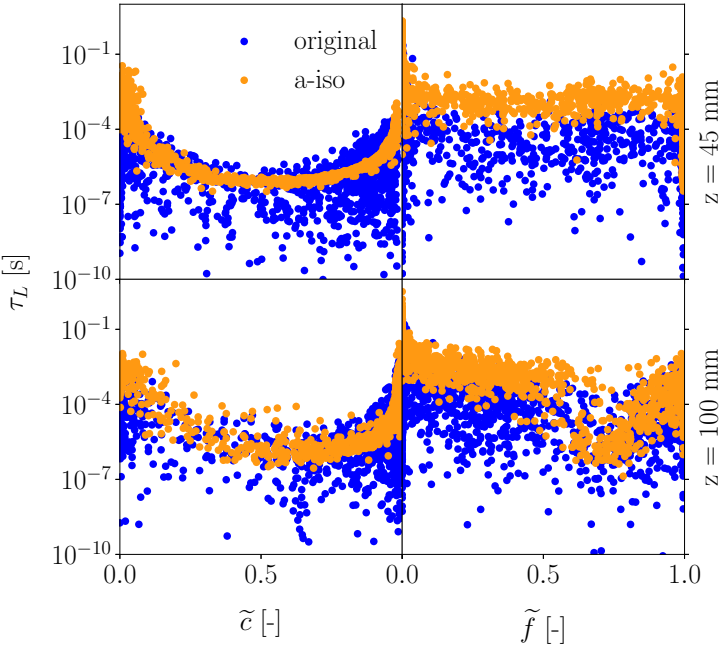

Figure 7.6: Mixing time scale τ_L versus $\tilde{c}(x^p)$ (first column) and versus $\tilde{f}(x^p)$ (second column) of MMC results with the original mixing model (case 3) and the anisotropic mixing model (case 6) at different axial positions.

be larger than τ_{orig}, which is in line with the DNS studies by Vo *et al.* [81]. Larger time scales lead to the increased fluctuations which is also consistent with the above discussion surrounding Figs. 7.4 and 7.5.

7.5.3 Flame structure

While ATF-FGM can predict a flamelet-like flame structure only, the PDF method is able to predict the deviations thereof. As demonstrated

in the previous two chapters, singly conditioned MMC can approximate deviations from a flamelet solution quite accurately. In Fig. 7.7, the effect of the different mixing time scale models for doubly conditioned MMC on conditional scalar fluctuations is shown. The flame character-

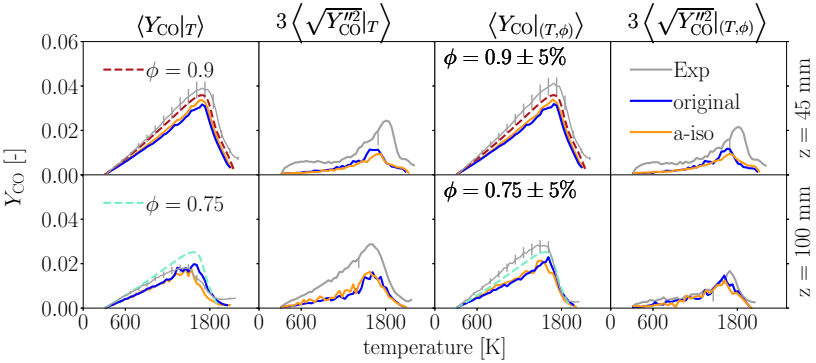

Figure 7.7: Mass fraction of CO versus temperature for experimental data (grey lines) and MMC results of case 3 (blue lines) and case 6 (orange lines) approach. Left column: conditional mean; center left column: conditional RMS; center right column: conditional mean for specific equivalence ratios and right column: conditional RMS for specific equivalence ratios. The coloured dashed lines within the first and third column are given by the FGM table for different equivalence ratios, namely $\phi = 0.9$ and $\phi = 0.75$.

istics are extracted from the particle solution in MMC. In the first and second column the conditional mean mass fraction of CO and its RMS versus temperature are shown. The dashed lines depict the flamelet solution extracted from the FGM table for a specific equivalence ratio. Close to the nozzle (and for $\phi = 0.9$) the MMC results and the experimental data approximate the flamelet solution quite well as is evidenced by the similar conditional mean profiles. Reasons for the higher values observed in the measurements were discussed in the pre-

vious chapter. Further downstream the deviations from the conditional mean increase and the deviations are slightly underpredicted by the MMC results. As already seen in the previous chapters, the increased deviations around the conditional mean may have two causes: turbulence and stratification, i.e. variation in equivalence ratio. Analogously to the previous chapters the turbulence-chemistry effects are isolated from stratification effects. This is obtained by plotting only data conditioned on a certain equivalence ratio (or mixture fraction) in the third and fourth column of Fig. 7.7. The RMS of the doubly conditioned CO mass fraction predicts the deviations from the flamelet solution for a fixed equivalence ratio. The trends for the doubly conditioned mean of the experimental data are correctly captured by MMC. The doubly conditioned RMS are quite similar for the different mixing time scale models, comparable to the experimental data and certainly different from zero as ATF-FGM would predict. The mixing frequency of the original model leads to slightly larger peak of the doubly conditioned RMS but differences are small overall. Note that the doubly conditioned RMS presented here are similar to predictions using the singly conditioned MMC approach in Sec. 6.4. This is not surprising as the effect of consistent treatment due to double conditioning is expected to be largest in the outer shear layer where stratification is significant.

7.6 Summary

The doubly conditioned MMC model is applied to the reference configuration TSF-A. In the doubly conditioned MMC model the reference variable space is extended to two dimensions. The LES-filtered mixture fraction is introduced as a second conditioning variable for the MMC mixing term. This additional reference variable leads to the distinction of fluid elements with different equivalence ratios that originate from

the stratification of the flame. At the same time the additional reference variable requires a modification of standard mixing time scale models and a blending function that combines the models for premixed and non-premixed combustion is introduced. The doubly conditioned MMC results show an improvement of the mixing fraction predictions compared to the singly conditioned MMC approach as it prevents unphysical mixing across the shear layer that cannot be captured by the singly conditioned approach. The key advantage of double conditioning is the more consistent treatment away from the flame front where quantities defined for premixed combustion become ill-defined and some ad hoc corrections needed to be introduced for simple single conditioning approaches. Furthermore, two different approaches of the mixing time scales are analyzed and their applicability to turbulent premixed combustion with stratification is investigated. While mean properties are quite insensitive to the different mixing time scale models and flame position hardly changes, the anisotropic model predicts - on average - larger mixing time scales leading to larger fluctuations of stochastic mixture fraction (z^p) around its corresponding LES-filtered mixture fraction value ($\tilde{f}$). This does, however, not increase the deviations from the flamelet structure significantly as evidenced by the small changes in doubly conditioned CO mass fractions. The findings of this study for stratified flames are in contrast to the findings for non-premixed flames [29, 81]. There, differences in mixing time scale models had significant effects on scalar variances with clearly improved predictions when using an anisotropic time scale model. For stratified flames these differences are much smaller and both models can provide adequate mixing frequencies. The doubly conditioned MMC model with the "standard" set of MMC parameters predicted accurate results compared to experimental data for the reference configuration TSF-A. Hence, the doubly conditioned MMC-ATF model presents a

more robust model as the treatment of pure mixing without combustion is directly modelled compared to the singly conditioned MMC-ATF model.

Chapter 8

Conclusion and outlook

8.1 Conclusion

This work presents a novel computational method - MMC-ATF - for the modelling of turbulent premixed combustion with stratification based on the multiple mapping conditioning mixing model. In turbulent premixed combustion the level of turbulence influences the flame structure differently. This affects the choice of the computational approach. Conventional mixing models cannot necessarily predict thin premixed flames in the flamelet regime. In MMC-ATF the stochastic particles mix close in composition space to ensure a flamelet structure if necessary. The localization in composition space is realized in MMC by conditioning the mixing operator on a reference space. For non-premixed combustion the reference space is given by the LES-filtered mixture fraction and this was extensively validated [29, 52, 53]. This choice of the reference space is questionable in turbulent premixed combustion with stratification. In this work the reference space is taken to be the LES-filtered reaction progress variable, $\tilde{c}$, of the artificially thickened

flame. The reference variable is obtained from the LES-ATF-FGM solution and interpolated to the particle position. The MMC version presented in this work is a sparse Lagrangian particle method, meaning that there are fewer stochastic particles than computational cells. To demonstrate the flamelet consistency of MMC-ATF and possible deviations thereof the model is applied to different configurations of the TSF series, which are located within the thin reaction zone regime. The model is validated by comparing the simulation results with experimental data.

Firstly, sensitivities towards modelling constants appearing in the mixing time scale model and the particle selection are investigated. While the standard value of the localness parameter transferred from non-premixed combustion yielded good predictions, the mixing time scale modelling needs to be adapted. For this parameter set consistency between the ATF-FGM and the MMC flame position is given. The results are hardly sensitive to the exact choice of the localness parameter in reaction progress variable space. The MMC approach predicts a flamelet structure at locations where the flame is thin and deviations thereof which are comparable to the deviations predicted by the experimental data. This demonstrates that MMC-ATF is a valuable model for the prediction of turbulent premixed combustion with stratification, which is flamelet consistent and predicts possible deviations from the flamelet structure.

Secondly, the singly conditioned MMC approach is applied to different configurations of the TSF series with and without shear and stratification. MMC-ATF predicts all flames with good accuracy compared with the experimental data. The flamelet structure of the real flame is accurately predicted by the MMC approach. The deviations from the flamelet structure are of good accuracy when compared to the experimental data. The trends for the different flames of the series

are predicted correctly by the MMC model. These results confirm the feasibility of the new MMC model for a range of different flames with one set of parameters.

In a final step, the reference variable space is extended to two dimensions by the additional LES-filtered mixture fraction. Via the second reference variable fluid elements of different equivalence ratios are distinguished. This results in improved and more reliable MMC predictions of the mean mixing layer position compared to singly conditioned MMC results. With the introduction of a second reference variable the computation of the localness parameter in physical space, r_m, based on two reference variables is updated and a variation of r_m hardly shows any influence on the results. Additionally, the mixing time scale model is revised and two different models are investigated. The mean properties are quite insensitive to the different mixing time scale models, but the anisotropic mixing time scale model predicts larger fluctuations for mixture fraction aligned with findings for non-premixed combustion [81]. Within the flame front these differences are not observed. Both models are adequate for modelling turbulent stratified combustion. In sum, the described observations state that the doubly conditioned MMC is a valuable model extension, which treats stratification directly.

The achievement of the described objectives results in the overall goal of this thesis which is the demonstration of the general feasibility of a novel Lagrangian MMC mixing model to predict turbulent premixed combustion with stratification.

8.2 Outlook

Even though the MMC-ATF results show good agreement with the experimental data, the mixing time scale, τ_L, can influence the flame

propagation speed in MMC. This can result in inconsistent flame propagation speeds predicted by the ATF-FGM and MMC models. This inconsistency cannot guarantee an MMC specific correlation which is clearly not desired. A more generic approach should directly couple the flame position predicted by MMC with the one obtained via the ATF approach. Furthermore, a proper investigation of the Lagrangian mixing time scale should isolate the model influence of LES from potential deficiencies in modelling of τ_L. Because DNS is able to resolve sub-grid scales the comparison of DNS with MMC-ATF can help to further develop and validate the mixing time scale model. Despite the modelling of flames within or close to the flamelet regime within this work, further analysis of applications with obvious deviations from the flamelet structure are desired. To predict deviations from the flame structure prescribed by the FGM approach beyond the flamelet regime which can influence the density and viscosity field a backward coupling from the stochastic particles to the Eulerian framework is needed. Care would need to be taken because of the sparse particle distribution and as the LES-filtered reaction progress variable is artificially thickened while the particle solution represents a thin flame. In the sparse Lagrangian MMC approach for non-premixed combustion the density is mapped from the particle solution onto the LES grid based on the equivalent enthalpy approach [12]. This density feedback can be realized via flamelet tables or kernel estimation in non-premixed combustion [25], but is not that trivial in premixed combustion. For the mapping a coupling variable is necessary. A transport equation for this coupling variable needs to be solved, which in premixed combustion will state a filtered chemical source term. A possible backward closure in premixed combustion could adapt the non-premixed approach or in an alternate approach scale the tabulated chemistry as proposed in [41]. Once an adequate mapping is achieved for turbulent premixed combus-

tion, the dependency on the mixture fraction needs to be considered in the density feedback (double conditioning). ATF-MMC will become an even more promising model for turbulent stratified combustion for all regimes of the premixed regime diagram.

Bibliography

[1] P. Auzillon, O. Gicquel, N. Darabiha, D. Veynante, and B. Fiorina. A Filtered Tabulated Chemistry model for LES of stratified flames. Combust. Flame, 159(8):2704–2717, 2012.

[2] R. S. Barlow, S. Meares, G. Magnotti, H. Cutcher, and A. R. Masri. Local extinction and near-field structure in piloted turbulent CH4/air jet flames with inhomogeneous inlets. Combust. Flame, 162(10):3516 – 3540, 2015.

[3] R. W. Bilger, S. H. Starner, and R. J. Kee. On reduced mechanisms for methane-air combustion in nonpremixed flames. Combust. Flame, 80(2):135–149, 1990.

[4] M. Boger, D. Veynante, H. Boughanem, and A. Trouvé. Direct numerical simulation analysis of flame surface density concept for large eddy simulation of turbulent premixed combustion. Proc. Combust. Inst., 27(1):917–925, 1998.

[5] T. Butler and P. O'Rourke. A numerical method for two-dimensional unsteady reacting flows. Proc. Combust. Inst., 16(1):1503–1515, 1977.

[6] R. R. Cao and S. B. Pope. The influence of chemical mechanisms on PDF calculations of nonpremixed piloted jet flame. Combust. Flame, 143(4):450–470, 2005.

[7] R. R. Cao, H. Wang, and S. B. Pope. The effect of mixing models in PDF calculations of piloted jet flames. Proc. Combust. Inst., 31(1):1543–1550, 2007.

[8] N. Chakraborty, J. W. Rogerson, and N. Swaminathan. A priori assessment of closures for scalar dissipation rate transport in turbulent premixed flames using direct numerical simulation. Phys. Fluids, 20(4):045106, 2008.

[9] U. N. C. Change. The Paris Agreement. https://unfccc.int/process-and-meetings/the-paris-agreement/the-paris-agreement, 2021.

[10] F. Charlette, C. Meneveau, and D. Veynante. A power-law flame wrinkling model for LES of premixed turbulent combustion Part I: non-dynamic formulation and initial tests. Combust. Flame, 131(1-2):159–180, 2002.

[11] F. Charlette, C. Meneveau, and D. Veynante. A power-law flame wrinkling model for LES of premixed turbulent combustion Part II: non-dynamic formulation and initial tests. Combust. Flame, 131(1-2):181–197, 2002.

[12] M. J. Cleary and A. Y. Klimenko. A detailed quantitative analysis of sparse-Lagrangian filtered density function simulations in constant and variable density reacting jet flows. Phys. Fluids, 23(11):115102, 2011.

[13] O. Colin, F. Ducros, D. Veynante, and T. Poinsot. A thickened flame model for large eddy simulations of turbulent premixed combustion. Phys. Fluids, 12(7):1843–1863, 2000.

[14] P. J. Colucci, F. A. Jaberi, P. Givi, and S. B. Pope. Filtered density function for large eddy simulation of turbulent reacting flows. Phys. Fluids, 10(2):499–515, 1998.

[15] J. A. M. de Swart, G. R. A. Groot, J. A. van Oijen, J. H. M. ten Thije Boonkkamp, and L. P. H. de Goey. Detailed analysis of the mass burning rate of stretched flames including preferential diffusion effects. Combust. Flame, 145(1):245–258, 2006.

[16] J. E. Dec. Advanced compression-ignition engines—understanding the in-cylinder processes. Proc. Combust. Inst., 32(2):2727–2742, 2009.

[17] C. Dopazo and E. E. O'Brien. An approach to the autoignition of a turbulent mixture. Acta Astronautica, 1(9-10):1239–1266, 1974.

[18] D. Dovizio and C. B. Devaud. Doubly Conditional Source-term Estimation (DCSE) for the modelling of turbulent stratified V-shaped flame. Combust. Flame, 172:79–93, 2016.

[19] T. D. Dunstan, Y. Minamoto, N. Chakraborty, and N. Swaminathan. Scalar dissipation rate modelling for large eddy simulation of turbulent premixed flames. Proc. Combust. Inst., 34(1):1193–1201, 2013.

[20] L. Durand and W. Polifke. Implementation of the Thickened Flame Model for Large Eddy Simulation of Turbulent Premixed Combustion in a Commercial Solver. ASME Turbo Expo Conference Proceedings, pages 869–878, 2007.

[21] D. Farrace, K. Chung, M. Bolla, Y. M. Wright, K. Boulouchos, and E. Mastorakos. A LES-CMC formulation for premixed flames including differential diffusion. Combust. Theor. Modelling, 22(3):411–431, 2018.

[22] B. Fiorina, R. Mercier, G. Kuenne, A. Ketelheun, A. Avdić, J. Janicka, D. Geyer, A. Dreizler, E. Alenius, C. Duwig, P. Trisjono, K. Kleinheinz, S. Kang, H. Pitsch, F. Proch, F. Cavallo Marincola, and A. Kempf. Challenging modeling strategies for LES of non-adiabatic turbulent stratified combustion. Combust. Flame, 162(11):4264–4282, 2015.

[23] J. H. Friedman, J. L. Bentley, and R. A. Finkel. An algorithm for finding best matches in logarithmic expected time. ACM Transactions on Mathematical Software, 3(3):209–226, 1977.

[24] S. Galindo-Lopez. Modelling of Mixed-mode Combustion using Multiple Mapping Conditioning. PhD thesis, The University of Sydney, 2018.

[25] S. Galindo-Lopez, F. Salehi, M. J. Cleary, A. R. Masri, G. Neuber, O. T. Stein, A. Kronenburg, A. Varna, E. R. Hawkes, B. Sundaram, A. Y. Klimenko, and Y. Ge. A stochastic multiple mapping conditioning computational model in OpenFOAM for turbulent combustion. Comput. Fluids, 172(1):410–425, 2018.

[26] Y. Gao, N. Chakraborty, and N. Swaminathan. Algebraic Closure of Scalar Dissipation Rate for Large Eddy Simulations of Turbulent Premixed Combustion. Combust. Sci. Techn., 186(10-11):1309–1337, 2014.

[27] Y. Ge, M. J. Cleary, and A. Y. Klimenko. A comparative study of Sandia flame series (D–F) using sparse-Lagrangian MMC modelling. Proc. Combust. Inst., 34(1):1325–1332, 2013.

[28] D. C. Haworth. A probability density function/flamelet method for partially premixed turbulent combustion. In Technical report, CTR Report, 2000.

[29] Z. Huo, F. Salehi, S. Galindo-Lopez, M. J. Cleary, and A. R. Masri. Sparse MMC-LES of a Sydney swirl flame. Proc. Combust. Inst., 27(2):2191–2198, 2019.

[30] International Workshop on Measurement and Computation of Turbulent Nonpremixed Flames (TNF). Sandia. available at http://www.tnfworkshop.org, 2020.

[31] F. A. Jaberi, P. J. Colucci, S. James, P. Givi, and S. B. Pope. Filtered mass density function for large-eddy simulation of turbulent reacting flows. J. Fluid Mech., 401:85–121, 1999.

[32] J. Janicka, W. Kolbe, and W. Kollmann. Closure of the transport equation for the probability density funcfion of turbulent scalar fields. Journal of Non-Equilibrium Thermodynamics, 4:47–66, 1979.

[33] W. P. Jones and S. Navarro-Martinez. Large eddy simulation of autoignition with a subgrid probability density function method. Combust. Flame, 150(3):170–187, 2007.

[34] M. M. Kamal, R. S. Barlow, and S. Hochgreb. Conditional analysis of turbulent premixed and stratified flames on local equivalence ratio and progress of reaction. Combust. Flame, 162(10):3896–3913, 2015.

[35] A. Kempf, M. Klein, and J. Janicka. Efficient Generation of Initial- and Inflow-Conditions for Transient Turbulent Flows in Arbitrary Geometries. Flow Turbul. Combust., 74(1):67–84, 2005.

[36] A. Klimenko. Matching conditional moments in PDF modelling of nonpremixed combustion. Combust. Flame, 143(4):369–385, 2005.

[37] A. Y. Klimenko and S. B. Pope. The modeling of turbulent reactive flows based on multiple mapping conditioning. Phys. Fluids, 15(7):1907–1925, 2003.

[38] A. N. Kolmogorov. The local structure of turbulence in incompressible viscous fluid for very large Reynolds numbers. Royal Society, 434:9–13, 1991.

[39] A. Kronenburg. Double conditioning of reactive scalar transport equations in turbulent non-premixed flames. Phys. Fluids, 16(7):2640–2648, 2004.

[40] A. Kronenburg and M. J. Cleary. Multiple mapping conditioning for flames with partial premixing. Combust. Flame, 155(1-2):215–231, 2008.

[41] A. Kronenburg and M. Kostka. Modeling extinction and reignition in turbulent flames. Combust. Flame, 143(4):342–356, 2005.

[42] G. Kuenne, A. Ketelheun, and J. Janicka. LES modeling of premixed combustion using a thickened flame approach coupled with FGM tabulated chemistry. Combust. Flame, 158(9):1750–1767, 2011.

[43] G. Kuenne, F. Seffrin, F. Fuest, T. Stahler, A. Ketelheun, D. Geyer, J. Janicka, and A. Dreizler. Experimental and numerical analysis of a lean premixed stratified burner using 1D Ra-

man/Rayleigh scattering and large eddy simulation. Combust. Flame, 159(8):2669–2689, 2012.

[44] G. Künne. Large eddy simulation of premixed combustion using artificial flame thickening coupled with tabulated chemistry. PhD thesis, TU Darmstadt, Göttingen, 2012. Zugl.: Darmstadt, Techn. Univ., Diss., 2012.

[45] M. Kuron, Z. Ren, E. Hawkes, H. Zhou, H. Kolla, J. Chen, and T. Lu. A mixing timescale model for TPDF simulations of turbulent premixed flames. Combust. Flame, 177:171–183, 2017.

[46] J. P. Legier, T. Poinsot, and D. Veynante. Dynamically thickened flame LES model for premixed and non-premixed turbulent combustion. In Proc. Summer Program 2000, CTR, pages 157–168, 2000.

[47] R. P. Lindstedt, S. A. Louloudi, and E. M. Váos. Joint scalar probability density function modeling of pollutant formation in piloted turbulent jet diffusion flames with comprehensive chemistry. Proc. Combust. Inst., 28(1):149–156, 2000.

[48] R. P. Lindstedt and E. M. Vaos. Transported PDF modeling of high-Reynolds-number premixed turbulent flames. Combust. Flame, 145(3):495–511, 2006.

[49] A. N. Lipatnikov. Stratified turbulent flames: Recent advances in understanding the influence of mixture inhomogeneities on premixed combustion and modeling challenges. Prog. Energ. Combust. Sci., 62:87–132, 2017.

[50] F. Marincola, T. Ma, and A. Kempf. Large eddy simulations of the Darmstadt turbulent stratified flame series. Proc. Combust. Inst., 34(1):1307–1315, 12 2013.

[51] A. Masri. Partial premixing and stratification in turbulent flames. Proc. Combust. Inst., 35(2):1115 – 1136, 2015.

[52] G. Neuber, F. Fuest, J. Kirchmann, A. Kronenburg, O. T. Stein, S. Galindo-Lopez, M. J. Cleary, R. S. Barlow, B. Coriton, J. H. Frank, and J. A. Sutton. Sparse-Lagrangian MMC modelling of the Sandia DME flame series. Combust. Flame, 208:110 – 121, 2019.

[53] G. Neuber, A. Kronenburg, O. T. Stein, and M. J. Cleary. MMC-LES modelling of droplet nucleation and growth in turbulent jets. Chem. Eng. Sci., 167:204–218, 2017.

[54] N. Peters. Turbulent Combustion. Cambridge University Press, 2000.

[55] T. Poinsot and D. Veynante. Theoretical and Numerical Combustion. R. T. Edwards, 2001.

[56] S. B. Pope. PDF methods for turbulent reactive flows. Prog. Energy Combust. Sci., 11(2):119–192, 1985.

[57] S. B. Pope. Turbulent Flows. Cambridge University Press, 2000.

[58] S. B. Pope. A model for turbulent mixing based on shadow-position conditioning. Phys. Fluids, 25(11):110803, 2013.

[59] H. Ritchie and M. Roser. Energy. Our World in Data, 2020. https://ourworldindata.org/energy.

[60] D. H. Rowinski and S. B. Pope. An investigation of mixing in a three-stream turbulent jet. Phys. Fluids, 25(10):105105, 2013.

[61] F. Salehi, M. J. Cleary, A. R. Masri, Y. Ge, and A. Y. Klimenko. Sparse-Lagrangian MMC simulations of an n-dodecane jet

at engine-relevant conditions. Proc. Combust. Inst., 36:3577–3585, 2017.

[62] F. Seffrin, F. Fuest, D. Geyer, and A. Dreizler. Flow field studies of a new series of turbulent premixed stratified flames. Combust. Flame, 157(2):384–396, 2010.

[63] L. Selle, G. Lartigue, T. Poinsot, R. Koch, K.-U. Schildmacher, W. Krebs, B. Prade, P. Kaufmann, and D. Veynante. Compressible large eddy simulation of turbulent combustion in complex geometry on unstructured meshes. Combust. Flame, 137(4):489 – 505, 2004.

[64] J. Smagorinsky. General circulation experiments with the primitive equations. Monthly Weather Review, 91:99–164, 1963.

[65] G. P. Smith, D. M. Golden, M. Frenklach, N. W. Moriarty, B. Eiteneer, M. Goldenberg, C. T. Bowman, R. K. Hanson, S. Song, W. C. Gardiner, V. V. Lissianski, and Z. Qin. available at http://combustion.berkeley.edu/gri-mech/, 2021.

[66] K. R. Sreenivasan. Fractals and multifractals in fluid turbulence. Ann. Rev. Fluid Mech., 23(1):539–604, 1991.

[67] T. Stahler, D. Geyer, G. Magnotti, P. Trunk, M. J. Dunn, R. S. Barlow, and A. Dreizler. Multiple conditioned analysis of the turbulent stratified flame A. Proc. Combust. Inst., 36(2):1947–1955, 2017.

[68] M. Stöllinger and S. Heinz. Evaluation of scalar mixing and time scale models in PDF simulations of a turbulent premixed flame. Combust. Flame, 157(9):1671–1685, 2010.

[69] C. Straub, S. De, A. Kronenburg, and K. Vogiatzaki. The effect of timescale variation in multiple mapping conditioning mixing of PDF calculations for Sandia Flame series (D-F). Combust. Theor. Model., 20(5):894–912, 2016.

[70] C. Straub, A. Kronenburg, O. T. Stein, R. S. Barlow, and D. Geyer. Modeling stratified flames with and without shear using multiple mapping conditioning. Proc. Combust. Inst., 37(2):2317–2324, 2019.

[71] C. Straub, A. Kronenburg, O. T. Stein, S. Galindo-Lopez, and M. J. Cleary. Mixing time scale models for multiple mapping conditioning with two reference variables. Flow Turbul. Combust., 106:1143 – 1166, 2021.

[72] C. Straub, A. Kronenburg, O. T. Stein, G. Kuenne, J. Janicka, R. S. Barlow, and D. Geyer. Multiple mapping conditioning coupled with an artificially thickened flame model for turbulent premixed combustion. Combust. Flame, 196:325–336, 2018.

[73] S. Subramaniam and S. B. Pope. A mixing model for turbulent reactive flows based on Euclidean minimum spanning trees. Combust. Flame, 115:487–514, 1998.

[74] B. Sundaram and A. Y. Klimenko. A PDF approach to thin premixed flamelets using multiple mapping conditioning. Proc. Combust. Inst., 36(2):1937–1945, 2017.

[75] B. Sundaram and A. Y. Klimenko. A pdf approach to thin premixed flamelets using multiple mapping conditioning. Proc. Combust. Inst., 36(2):1937–1945, 2017.

[76] R. R. Tirunagari and S. B. Pope. LES/PDF for premixed combustion in the DNS limit. Combust. Theor. Model., 20(5):834–865, 2016.

[77] P. Trisjono, K. Kleinheinz, H. Pitsch, and S. Kang. Large Eddy Simulation of Stratified and Sheared Flames of a Premixed Turbulent Stratified Flame Burner Using a Flamelet Model with Heat Loss. Flow Turbul. Combust., 92:201–235, 2014.

[78] J. A. van Oijen and L. P. H. de Goey. Modelling of premixed laminar flames using flamelet-generated manifolds. Combust. Sci. Techn., 161(1):113–137, 2000.

[79] H. K. Versteeg and W. Malalasekera. An Introduction to Computational Fluid Dynamics: The Finite Volume Method. Pearson/Prentice Hall, second edition, 2007.

[80] S. Vo, A. Kronenburg, O. T. Stein, and M. J. Cleary. Multiple mapping conditioning for silica nanoparticle nucleation in turbulent flows. Proc. Combust. Inst., 36:1089–1097, 2017.

[81] S. Vo, O. T. Stein, A. Kronenburg, and M. J. Cleary. Assessment of mixing time scales for a sparse particle method. Combust. Flame, 179:280–299, 2017.

[82] K. Vogiatzaki, A. Kronenburg, M. J. Cleary, and J. Kent. Multiple mapping conditioning of turbulent jet diffusion flames. Proc. Combust. Inst., 32(2):1679–1685, 2009.

[83] K. Vogiatzaki, A. Kronenburg, S. Navarro-Martinez, and W. P. Jones. Stochastic multiple mapping conditioning for a piloted, turbulent jet diffusion flame. Proc. Combust. Inst., 33(1):1523–1531, 2011.

[84] A. P. Wandel and A. Y. Klimenko. Testing multiple mapping conditioning mixing for Monte Carlo probability density function simulations. Phys. Fluids, 17(12):128105, 2005.

[85] H. Wang, T. Pant, and P. Zhang. LES/PDF Modeling of Turbulent Premixed Flames with Locally Enhanced Mixing by Reaction. Flow Turbul. Combust., 100(1):147–175, 2018.

[86] F. Williams. Combustion Theory. Addison-Wesley, Redwood City, second edition, 1985.

[87] J. Xu and S. B. Pope. PDF calculations of turbulent nonpremixed flames with local extinction. Combust. Flame, 123(3):281–307, 2000.

[88] Y. Yang, J. E. Dec, N. Dronniou, and M. Sjöberg. Tailoring HCCI heat-release rates with partial fuel stratification: Comparison of two-stage and single-stage-ignition fuels. Proc. Combust. Inst., 33(2):3047–3055, 2011.

[89] B. T. Zoller, M. L. Hack, and P. Jenny. A PDF combustion model for turbulent premixed flames. Proc. Combust. Inst., 34(1):1421–1428, 2013.

Appendix A

Data storage

Table B1: Cases and code used to produce results of [72]. The corresponding code repository is "/itv-publications/2018_Straub_CNF.git". This table explains the particular cases for the sampled solution. The converged cases are given analogously in the folder *converge*.

"Multiple mapping conditioning coupled with an artificially thickened flame model for turbulent premixed combustion" (2018_Straub_CNF)		
Data on storage	Case	Code
samplingfm0point02CE1-GRIDT2e06NPC	$c_m = 0.02$, $C_c = 1.0$	"master" on GIT. SHA: af479be8794275091074cfbb28547c105f773f31
samplingfm0point03CE0point1-GRIDT2e06NPC	$c_m = 0.03$, $C_c = 0.1$	"master" on GIT. SHA: af479be8794275091074cfbb28547c105f773f31
samplingfm0point03CE0point5-GRIDT2e06NPC	$c_m = 0.03$, $C_c = 0.5$	"master" on GIT. SHA: af479be8794275091074cfbb28547c105f773f31
samplingfm0point03CE1-GRIDT2e06NPC	$c_m = 0.03$, $C_c = 1.0$	"master" on GIT. SHA: af479be8794275091074cfbb28547c105f773f31
samplingfm0point06CE1-GRIDT2e06NPC	$c_m = 0.06$, $C_c = 1.0$	"master" on GIT. SHA: af479be8794275091074cfbb28547c105f773f31

Table B2: Cases and code used to produce results of [70]. The corresponding code repository is "/itv-publications/2019_Straub_PCI.git". This table explains the particular cases for the sampled solution. The converged cases are given analogously in the folder *converge*.

"Modelling stratified flames with and without shear using multiple mapping conditioning" (2018_Straub_PCI)		
Data on storage	Case	Code
TSF-A/sampling-cm0point03CE0point5	TSF-A, $c_m = 0.03$, $C_c = 0.5$	"master" on GIT. SHA: 119661d55cce151fa074790879ff517efae7300a
TSF-C/samplingDecAngle-cm0point03CE0point5	TSF-C, $c_m = 0.03$, $C_c = 0.5$	"master" on GIT. SHA: 119661d55cce151fa074790879ff517efae7300a
TSF-G/samplingDecAngle-cm0poinit03CE0point5Radicals	TSF-G, $c_m = 0.03$, $C_c = 0.5$	"master" on GIT. SHA: 119661d55cce151fa074790879ff517efae7300a

Table B3: Cases and code used to produce results of [71]. The corresponding code repository is "/itv-publications/2020_Straub_FTC.git". This table explains the particular cases.

"Mixing time scale models for multiple mapping conditioning with two reference variables" (2020_Straub_FTC)		
Data on storage	Case	Code
original/singlyCond/ cm0point03ri3point4mmMax	Case 1 (cf. Tab. 7.1) here and in [71]	"master" on GIT. SHA: a35ea8d24a1769a81838c88843c01f2001f22682
original/fm0point03- cm0point03ri3p4mmHarmonic	Case 2 (cf. Tab. 7.1) here	"master" on GIT. SHA: a35ea8d24a1769a81838c88843c01f2001f22682
original/fm0point03- cm0point03ri4mmHarmonic	Case 3 (cf. Tab. 7.1) here and in [71]	"master" on GIT. SHA: a35ea8d24a1769a81838c88843c01f2001f22682
original/fm0point03- cm0point03ri5mmHarmonic	Case 4 (cf. Tab. 7.1) here	"master" on GIT. SHA: a35ea8d24a1769a81838c88843c01f2001f22682
original/fm0point03- cm0point03ri4mmMax	Case 5 (cf. Tab. 7.1) here and case 2 in [71]	"master" on GIT. SHA: a35ea8d24a1769a81838c88843c01f2001f22682
aISO/fm0point03- cm0point03ri4mmHarmonic	Case 6 (cf. Tab. 7.1) here and case 5 in [71]	"master" on GIT. SHA: a35ea8d24a1769a81838c88843c01f2001f22682
aISO/fm0point03- cm0point03ri4mmMax	Case 7 (cf. Tab. 7.1) here and case 4 in [71]	"master" on GIT. SHA: a35ea8d24a1769a81838c88843c01f2001f22682

Table B4: Scripts to create the figures which do not appear in the publications.

Scripts to create additional figures	
Code on storage	Figures
02_lamPlusFigBFER.ipynb	This script creates Figs. 2.1, 2.2 and 2.3.
CNF18/03_scatterData_woHistogram.ipynb	This script creates Figs. 5.11, 5.5 and 5.13.
CNF18/02a_unconditional.ipynb	This script creates Figs. 5.3 and 5.12.
PCI19/TSF_02a_unconditional.ipynb	This script creates Fig. 6.1.
PCI19/TSF_02a_unconditional.ipynb	This script creates Figs. 6.2-6.4.
03_uncondStratified_rmStudy.ipynb	This script creates Figs. 7.1.